Design, Prototyping and Characterization of a CMUT-on-ASIC Probe for High-Volume-Rate 3-D Abdominal Ultrasound Imaging

Rozsa, N.N.M.

DOI
10.4233/uuid:f4d4cf0c-b34a-40cf-9df1-499aa91a1a3f

Publication date
2025

Document Version
Final published version

Citation (APA)
Rozsa, N. N. M. (2025). *Design, Prototyping and Characterization of a CMUT-on-ASIC Probe for High-Volume-Rate 3-D Abdominal Ultrasound Imaging*. [Dissertation (TU Delft), Delft University of Technology]. https://doi.org/10.4233/uuid:f4d4cf0c-b34a-40cf-9df1-499aa91a1a3f

Design, Prototyping and Characterization of a CMUT-on-ASIC Probe for High-Volume-Rate 3-D Abdominal Ultrasound Imaging

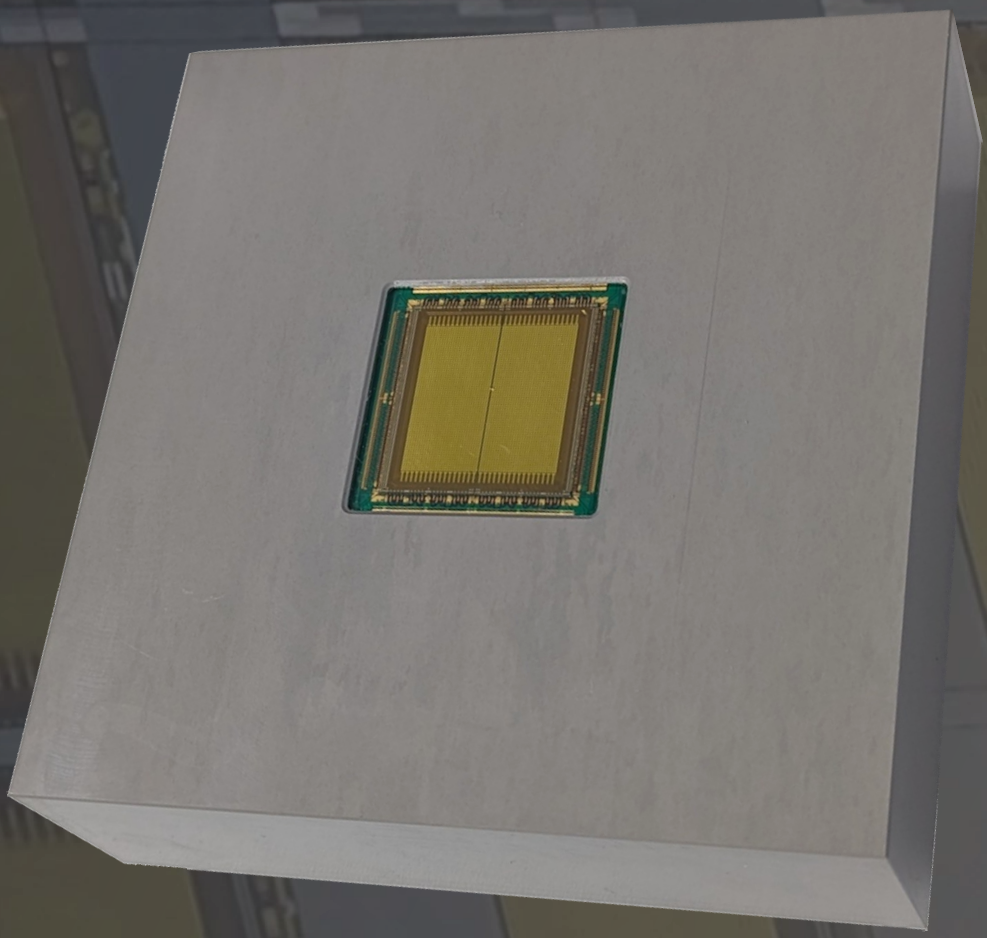

Nuriel Rozsa

Design, Prototyping and Characterization of a CMUT-on-ASIC Probe for High-Volume-Rate 3-D Abdominal Ultrasound Imaging

Design, Prototyping and Characterization of a CMUT-on-ASIC Probe for High-Volume-Rate 3-D Abdominal Ultrasound Imaging

Dissertation

for the purpose of obtaining the degree of doctor
at Delft University of Technology
by the authority of the Rector Magnificus, Prof.dr.ir. T.H.J.J. van der Hagen,
chair of the Board for Doctorates
to be defended publicly on
Tuesday 9 December 2025 at 12:30 o'clock

by

Nuriel Nathan Machiel Rozsa

Master of Science in Electrical Engineering, Delft University of Technology,
Netherlands
born in Seattle, United States.

This dissertation has been approved by the promotors.

Composition of the doctoral committee:

Rector Magnificus,	chairperson
Dr. ir. M.A.P. Pertijs,	Delft University of Technology, promotor
Dr. ir. M.D. Verweij,	Delft University of Technology, Erasmus MC University Medical Center, promotor

Independent Members:

Prof. dr. ir. R. Dekker,	Delft University of Technology
Prof. dr. ir. R. Lopata,	Eindhoven University of Technology
Prof. dr. A.S. Savoia,	Università degli Studi Roma Tre, Italy
Prof. dr. ir. W.A. Serdijn,	Delft University of Technology
Prof. dr. K.A.A. Makinwa,	Delft University of Technology, reserve member

Non-independent Members:

Dr. ir. H.J. Vos,	Delft University of Technology, Erasmus MC University Medical Center

This research is a part of the Ultra-X-treme programme (P17-32), financed by the Netherlands Organization for Scientific Research.

Keywords: Ultrasound, AAA, ASIC, 3D, High-Volume-Rate, Large Volume, CMUT, Bulk PZT Transducer, Transducer Array, Matrix Probe
Printed by: Proefschrift Specialist | www.proefschriftspecialist.nl
Cover by: Nuriel Rozsa

ISBN 978-94-93483-46-0
An electronic version of this dissertation is available at
http://repository.tudelft.nl/.

To my friends and family

Contents

1

Introduction

1.1. Motivation

1.1.1. Cardiovascular Conditions

According to the World Health Organization (WHO), "cardiovascular diseases (CVDs) are the leading cause of death globally, taking an estimated 17.9 million lives each year." [1]. Of these, roughly 150,000-200,000 deaths are caused by abdominal aortic aneurysm (AAA) ruptures [2]. AAA is a condition where a person's abdominal aortic diameter is widened to 3.0 cm or more, with general risk of rupture increasing with width. Figure 1.1 shows an illustration of the condition. Surgical intervention is considered when a patient's abdominal aorta (AA) has a diameter exceeding 5.5 cm for men or 5.0 cm for women, and/or a yearly increase in diameter of more than 1.0 cm [3], [4].

Depending on the circumstances of the patient, two kinds of surgical interventions are possible, both with associated risks of complications and/or death. One is endovascular aortic aneurysm repair (EVAR), which is a minimally-invasive surgery in which a foldable graft is guided from the femoral artery (Figure 1.1) to the AA, and then anchored above and below the aneurysm. Once the graft is placed, it acts as a strengthening inline for the vessel, reducing risk of rupture [2], [5], [6], [7]. The other intervention is open aortic aneurysm repair (OR). This is an invasive operation in which the chest and aorta are opened, and a graft is

1

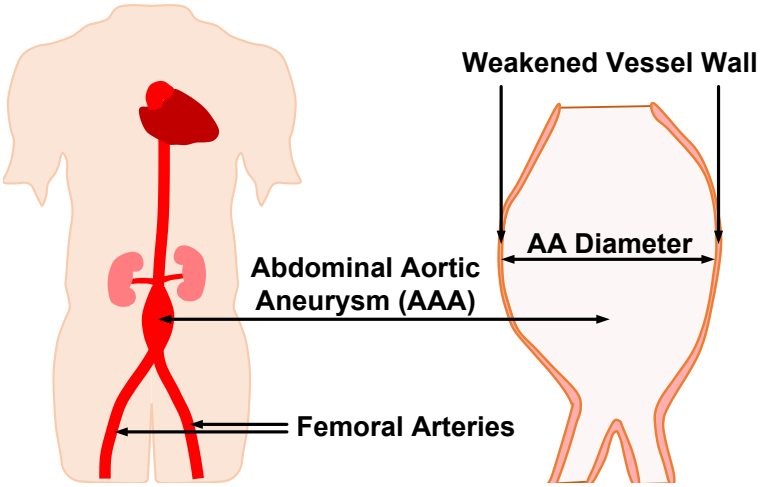

Figure 1.1: Illustration of AAA.

sewn inside the vessel [2], [8], [9]. To avoid negative patient outcomes, the risks of complications during and after these operations, versus the risk of AAA rupture are carefully weighted by specialists [2], [4].

However, in practice, specialists mostly rely on statistical data on the geometries of the vessel to assess these risks [2], [4]. While this results in a positive patient outcome in most cases, a non-insignificant amount of patients are still given an operation unnecessarily [10], [11] or die of AAA rupture due to an underestimation of the risk [12]. In addition, AAA repairs are expensive, costing tens of thousands of euros per operation including aftercare [13], [14]. Therefore, improving the accuracy of risk assessment both leads to improved patient outcomes and reduced cost of care. To do so, it is important to understand the current method of AAA diagnosis and what its shortcomings are.

1.1.2. Ultrasound Imaging for AAA Diagnosis

As aforementioned, as the AA increases in diameter, the more the patient is at risk of rupture. Given that patients with AAA do not experience symptoms, early diagnosis of patients often result in improved outcomes [2], [4], [15]. As such, the barrier for screening needs to be as low as possible. Currently, ultrasound imaging is used for diagnosing AAA [4], as it offers the following benefits towards this end:

- **Fast:** The operator can image the AA in real time [16], [17].
- **Safe:** Ultrasound imaging is regarded very safe, as it is non-invasive and does not expose the patient to harmful radiation [2], [4], [17], unlike imaging such as X-ray scans, computed tomography (CT) scans or Fluoroscopy, which expose patients to ionizing radiation [18].
- **Low cost:** Ultrasound imaging systems and their operation are less expensive than alternatives, such as (real-time) magnetic resonance imaging ((RT-)MRI) or radiation-based scans [16], [19].
- **Portable:** Ultrasound imaging does not require a dedicated space in a clinic or hospital [16], making it flexibly applicable, unlike with (RT-)MRI or radiation-based scans.
- **Sufficient resolution:** Ultrasound offers a sufficiently high resolution for (cardio)vascular imaging [4], [17].

However, clinical ultrasound systems can typically only make 2-dimensional (2D) images (at a high frame-rate), and those that can make 3-dimensional (3D) images do so at a reduced frame-rate, which in some cases is too low when imaging the AA. To understand why this limitation exists and why it matters for treating AAAs, the operation and utilized imaging techniques of ultrasound systems are covered next.

1.2. Background

1.2.1. Operation of Ultrasound Imaging Systems

The working principle behind ultrasound imaging involves transmitting ultrasound beams and receiving their reflections. Images are then reconstructed from the time-of-flight and magnitude of the receive (RX) signals, the former mapping object locations and the latter determining contrast. Figure 1.2(a) shows a block diagram of a typical ultrasound imaging system. An array of ultrasound transducer elements connects to a transmit (TX) circuit or a RX circuit via transmit/receive (T/R) switch. Historically, the transducer elements in a probe were individually connected via micro-coaxial cables to the rest of the ultrasound system, an example of which is shown in Figure 1.2(b). However, parts of the system are increasingly

1

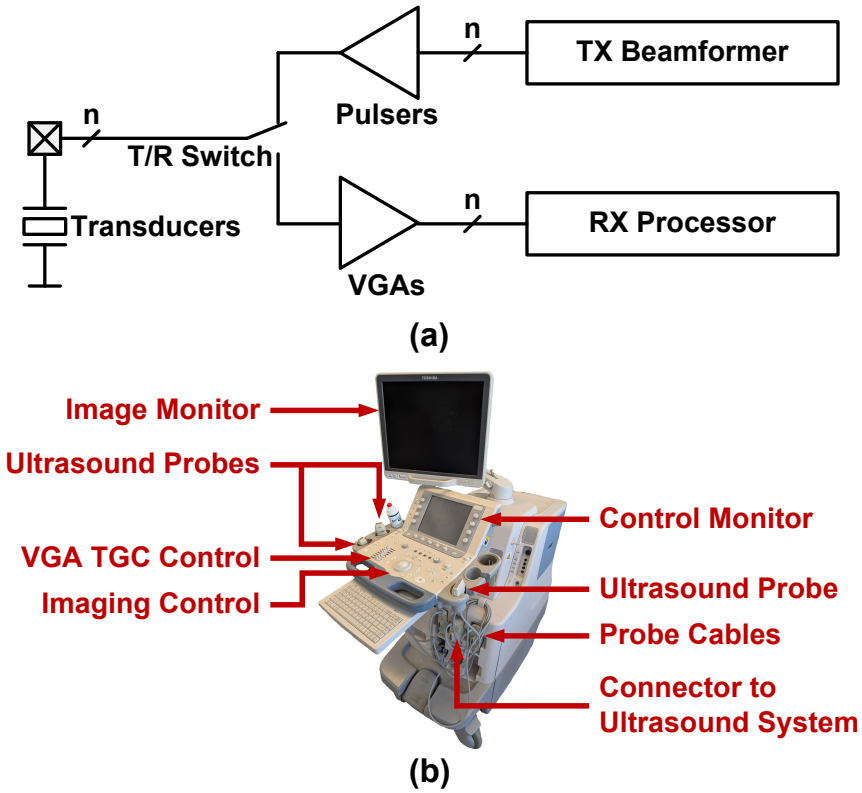

Figure 1.2: (a) Diagram of a typical ultrasound system with an n-channel transducer array. (b) Image of clinical ultrasound system.

integrated in the probe [20], [21], [22], [23], [24], [25], which is also covered in Section 1.3.

The TX circuit consists of programmable transducer drivers, and a TX beamformer (TX BF) that delays the actuation of the drivers by a programmable amount while also controlling the signal waveforms and amplitudes that the drivers produce. The RX circuit consists of low-noise variable-gain amplifiers (VGAs) and an RX signal processor. The signal processor, in turn, typically consists of analog-to-digital converters (ADCs), an RX beamformer (RX BF) that combines the amplified RX data into focused outputs, and an envelope detector to reconstruct the signal intensities in the ultrasound image [26].

While the RX channels only require a signal-to-noise ratio (SNR) around 30-50 dB, the RX dynamic range (DR) is typically much higher, as the human body exponentially attenuates ultrasound waves proportional to $s \times f_u$, where s is the propagation distance and f_u the frequency of the ultrasound waveform. Therefore, the VGAs typically have a time-gain compensation (TGC) feature [26], which involves the exponential increase in the VGA gain over each pulse-echo acquisition. This reduces the DR requirements for the following RX processor, improving power efficiency of the system.

Historically, imaging probes consisted of a 1-dimensional (1D) transducer array, allowing for 2D images to be made. However, probes with a 2D transducer array are increasingly common, enabling 3D imaging [26], [27], [28]. The size and operating frequency of a transducer array is a trade-off between form factor, the imaging depth requirement, and the required resolution of the reconstructed images, where the achievable resolution R_p is determined by the focus that the TX and RX beamformers can achieve. This, in turn, scales with the aperture of the probe A_p and f_u [29].

Figure 1.3(a) shows the typical operation of a TX BF. By making use of interference between the waveforms produced by each transducer element, the TX BF controls the steering angle and shape of the TX beams. Depending on the application, the amplitudes of the waveforms transmitted by each element are weighted to more accurately shape the direction in which energy is transmitted. The typical TX waveform is a Gaussian pulse, which is generated by driving the transducer array with an n-period pulse, where n depends on the frequency response of the transducer elements in the probe. This waveform is common, as it has a compact envelope in the time domain, which results in a high axial resolution, and is relatively easy to generate [26]. However, depending on the imaging application, more complex waveforms such as chirps or coded sequences are also used to improve performance [30], [31], [32], [33], [34], [35].

Figure 1.3(b) shows the typical operation of a RX BF. Similar to a TX BF, it uses interference to focus the probe to programmable points in space. A delay-and-sum algorithm is commonly used as a computationally-efficient method of combining the RX signals to a focused output, representing intensities of reflections at a focal point in the medium of interest. Weighting is also typically applied to the RX channels before summing to improve the directivity of the array to the focal point, and/or to improve the signal-to-noise ratio (SNR) of the focused waveform [26], [36].

1

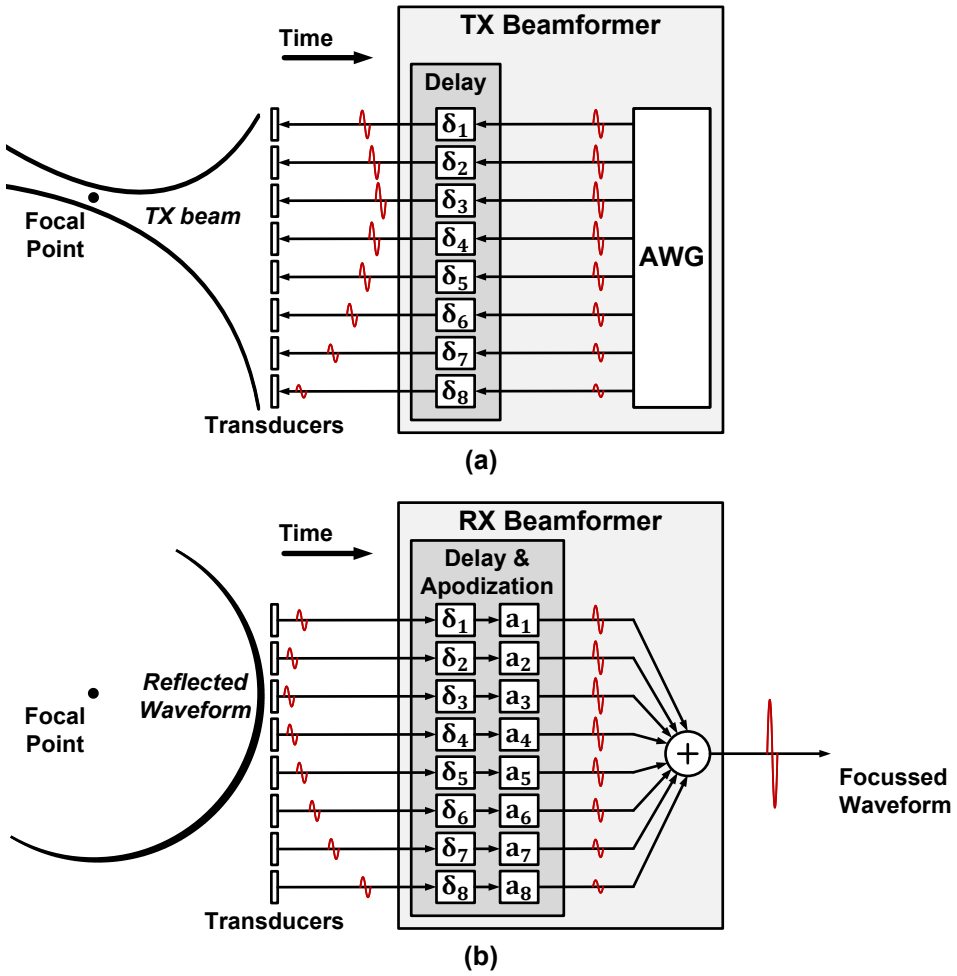

Figure 1.3: (a) Illustration of a typical TX BF for an 8-element transducer array. (b) Illustration of a typical RX BF for an 8-element transducer array implementing a delay-and-sum algorithm.

Conventionally, the transducer array consists of bulk-fabricated piezo-electric transducers [20], [21], [26]. However, micro-fabricated ultrasound transducers, such as capacitive micromachined ultrasound transducers (CMUTs) and piezo-electric micromachined ultrasound transducers (PMUTs) are increasingly used for their improved scalability, ease of integration with application-specific integrated circuits (ASICs) (further covered in Section 1.3) and bandwidth, compared to bulk-fabricated transducers [20], [21], [37].

1.2.2. Conventional Ultrasound Imaging Techniques

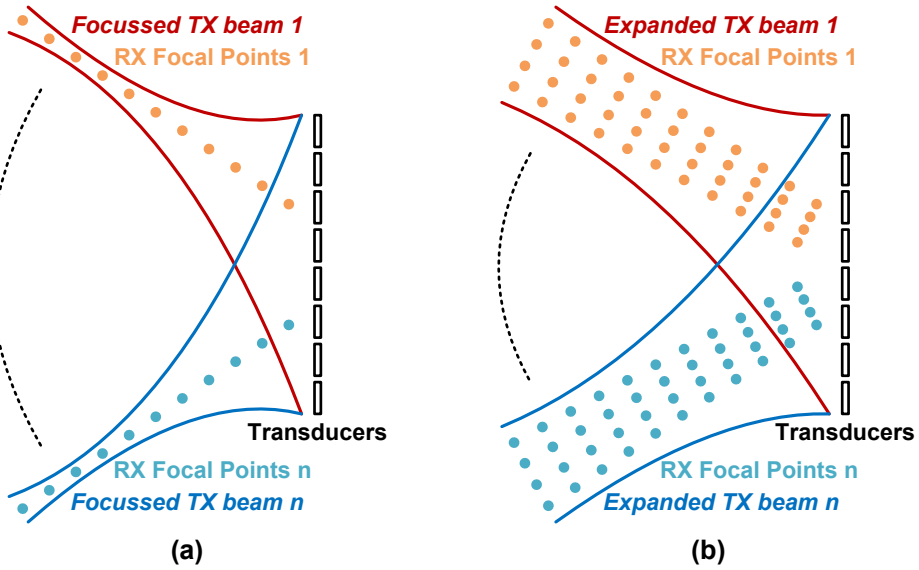

Figure 1.4: (a) Imaging with an 8-element transducer array, using n line scans for image reconstruction. (b) Imaging with an 8-element transducer array, using n subsector scans for image reconstruction.

Brightness mode (B-mode) imaging is a standard method for visualizing structures within a medium, such as the AA. It displays a 2D image where the brightness at each point represents the amount of reflected ultrasound energy [17]. These images are conventionally reconstructed from multiple pulse-echo acquisitions, where in each acquisition, the probe produces a focused beam along a scan line. After this, the RX BF focuses along that line to reconstruct reflection intensities. This process is repeated to reconstruct all points in the image, as shown in Figure 1.4(a). This method directly trades-off image resolution and/or size with frame-rate, as more scan lines require more pulse-echo acquisitions, each introducing a time delay stemming from the propagation speed of sound through the medium and back. As a frame rate between 30 Hz and 60 Hz is usually acceptable for real-time feedback, this trade-off does not present issues for structure visualization.

As aforementioned, when assessing the risk of AAA rupture, the diameter of the AA is currently the most strongly weighted biomarker. However, other imaging modes are also used to evaluate the health of the vessel, such as Doppler ultrasound, which is used to track blood flow through the vessel [16]. As the name

implies, the Doppler shift of returning ultrasound waveforms from the motion of blood are used to estimate flow speeds. Historically continuous waveforms were used (continuous wave (CW) Doppler), where the imaging array is sub-divided into transmitting and receiving sub-arrays. The received continuous waveform would be down-modulated by the TX frequency, such that the resulting signal represents the Doppler shift. By focusing the TX array and RX array at the same region, movement information is derived from there. However, this focal region can be quite broad, resulting in a poor spatial resolution [26], [38].

Pulsed-wave Doppler (PW Doppler) addresses this by transmitting wide-band waveforms instead. This imaging mode is similar to the aforementioned B-mode imaging, however, now the changes between pulse-echo acquisitions are used to determine the phase shift between successive pulse-echo acquisitions at each focal point, as this is easier to detect than the relatively narrow Doppler frequency shift that occurs. With the associated improvement in spatial resolution, turbulence and local gradients in flow speeds can now be evaluated [16]. However, since this method samples the phase shift at the pulse-echo rate, the maximum measurable flow speed is constrained by the Nyquist criterion [26]. This requires the probe to image at high frame rates to correctly reconstruct the high flow rates in the AA [39].

Figure 1.4(b) shows such a method. Instead of imaging with line scans, data is acquired with (sub)sector scans. This entails expanding the scanning region of the TX beams, where the RX beamformer focuses the digitized RX data along multiple lines within each TX beam. This enables larger subsectors of the medium to be imaged per pulse-echo acquisition, requiring fewer acquisitions to reconstruct an image. The benefit is an increased frame rate, but this comes at the cost of image quality: image resolution degrades due to an increased reliance on the achievable focus in RX only, the contrast will degrade by a reduced round-trip SNR per pulse-echo acquisition and increased clutter, and aberration effects by an inadequate estimation of the ultrasound propagation speed may be exacerbated. This trade-off remains as the size of each subsector scan is increased in return for increased frame-rate. While the scanning regions can be partially overlapped to focus in RX at the same points from multiple angles to improve the image resolution and contrast, this comes at the cost of a reduced frame-rate. Nevertheless, this approach can still achieve a higher frame rate for the same resolution than serial line scans [40], [41].

Another biomarker of interest is the wall strength of the vessel, which relates to its ability to withstand stresses before rupturing. This, in turn, may be related to the elastic properties of the vessel [42], [43]. Historically, for applications such as imaging certain types of cancers, such data could be acquired via ultrasound by strain elastography. This involves first acquiring B-mode image data with a probe lightly placed on the body, and subsequently reacquiring the data after an added compression is applied. Due to the compression, the reflected waveforms have a time-displacement, yet remain highly correlated to the reference data. As the time-displacement is correlated to the compression of the medium, the relative elasticity can be estimated. However, while this method can give a good indication of local variations in elasticity, the results strongly rely on the compression applied. As this is very inconsistent in practice, the results also have high tolerances. [26], [44]

For cardiovascular monitoring, physiologically generated displacements, such as those resulting from the beating of the heart, can also be used to measure elastic properties of vessels. For AAAs, this can involve measuring the change in volume and area of the vessel for a given change in blood pressure [42]. An alternative method of evaluating elasticity is by shear-wave elastography. This method tracks the propagation of shear-waves in the medium, which are induced by TX waveforms generated by the probe. As these shear-waves have low propagation speeds, they can be tracked in real time at frame rates in the kHz range.[26], [44], [45] As such, the trade-offs with this imaging mode are similar to those associated with Doppler ultrasound.

1.2.3. Emerging Imaging Techniques

As aforementioned, (shear-wave) elastography and Doppler ultrasound offer more biomarkers to assess the disease state of a AAA, improving accuracy of risk assessment. However, both methods historically have been used for evaluating a 2D plane. As blood flow and elasticity have 3D properties, more modern techniques such as 3D-flow and 3D-elastography are increasingly of interest [46], [47], [48], [49], [50]. As aforementioned, this is enabled by ultrasound systems with 2D transducer arrays. However, conventional 3D probes have not adequately been able to image the volume of interest at the required volume-rate due to hardware restrictions.

As will be covered more extensively in Chapter 2 and Chapter 4, due to the

high rates of movement and the large volume involved when imaging AAAs, very few volumetric subsector scans can be done to reconstruct each frame. Therefore, to maintain an acceptable resolution, a large aperture A_p is required. Moreover, a large A_p typically also comes at the cost of a large transducer element count to avoid grating-lobe artifacts in the field-of-view (FoV). The grating lobes of a beam generated by a 1D matrix array appear at the following angles [29]

$$\Theta_{g,m} = \pm arcsin\left(\frac{m\lambda}{p}\right) \tag{1.1}$$

where $\Theta_{g,m}$ are the angles of the grating lobes for $m \neq 0$, p is the pitch of the transducer elements in the matrix array and λ is the wavelength of the transmitted ultrasound waveform, with the same principle applying for 2D arrays [26], [29]. By requiring a large element count to image at a large FoV, multiple engineering challenges are introduced that affect the imaging strategies that the system can employ. The most significant of these is managing channel-count while retaining a high volume rate and flexibility in how the probe is used.

Commercial probes that use direct-element connections to an ultrasound system are constrained to arrays of roughly 1000 elements [51], [52] due to interconnect limitations [53], resulting in sharp performance compromises. For example, sparse arrays are carefully designed such that a minimal amount of elements occupy A_p while minimizing grating-lobe artifacts [54]. However, this increases clutter levels and reduces the transmitted and received signal amplitudes of the probe, resulting in a degraded image contrast and penetration depth. Alternatively, smaller dense arrays can be used [51], [52] at the cost of resolution [53] and/or penetration depth. Probes with imaging arrays exceeding 1000 elements that use row-column addressing have a limited FoV [55], making them unsuitable for AAA imaging.

1.3. Proposed Solution

Probes with array sizes exceeding 1000 elements that retain a sufficiently large FoV require channel-count reduction techniques, for which in-probe ASICs are well suited. In addition, these ASICs can provide added signal conditioning, such as pre-amplification, to improve the achievable imaging depth of the system. Moreover, by directly interfacing the transducer array with one or multiple ASICs, channel parasitics and in-probe interconnect can be minimized [22], [23], [24], [56]. However, the ASICs may not excessively limit the volume rate of the probe for its

intended application.

The targeted specifications for the probe are shown in Table 1.1. As the probe is intended for research on improved imaging of AAA, it needs be as flexibly applicable as possible. Therefore, a high flexibility in TX waveform definition and beamforming are also desirable properties. Moreover, the probe has to be compatible with existing research imaging systems to ease adoption.

Table 1.1: System specifications

Aperture	Imaging Depth	Field of View	Volume Rate	Acoustic Bandwidth	Element Pitch
23×23 mm^2	≥10 cm	60°×60°	2000 vol/s	2 - 4 MHz	365 µm

To accommodate these requirements, a novel 3D probe has been designed, which achieves the highest volume-rate for designs with in-probe channel-count reduction reported to date. The full probe consists of 2 tiled ASICs, each accommodating a 32×64-element transducer array. Each ASIC provides 8× channel-count reduction by means of 2×2 delay-and-sum micro-beamformers (µBFs) and 2× time-division multiplexing (TDM), thus exploiting the benefits of both techniques without reducing the frame rate below the acceptable limit (2000 volumes/s) or straining the requirements for the back-end receive system – Thus, the probe can interface with 2 commonly-used Verasonics Vantage-256 (VSX) imaging systems [52], [53], [57]. The probe also contains a novel TX BF that provides a high degree of flexibility in TX waveform definition by steering arbitrary pulse-density modulated (PDM) waveforms to pulsers, driving each element.

In addition, the probe was designed to be compatible with multiple different transducer technologies for added flexibility in its fabrication and to enable future fabrication of more application optimized variants. One of these are CMUTs [58], [59] that are monolithically fabricated on the ASICs. As these devices are fabricated at a wafer-level, they can result in reduced probe costs and improved yield. Moreover, CMUTs have a relatively high bandwidth compared to more traditionally integrated PZT transducers [60].

1.4. Outline

This thesis is organized as follows.

Chapter 2 covers the design and evaluation of the aforementioned probe with a 4096-element CMUT array that is monolithically integrated onto two custom ASICs developed in-house. Each ASIC in the probe interfaces with a custom motherboard that can be mounted to a Vantage-256 imaging system for ease of integration in existing medical R&D setups. The design scales the combination of micro-beamforming and TDM to an array of thousands of elements for the first time, while also implementing a novel TX BF, enabling the targeted state-of-the-art volume-rate to be demonstrated.

Chapter 3 covers the element-level acoustic evaluation of both the aforementioned CMUT transducers and a custom bulk-fabricated PZT transducer array, using the developed ultrasound probe as a test platform. Circuit, layout and packaging design trade-offs for having the system be compatible with these different transducers are also covered. With this, a more universal and consistent test platform for comparison of ultrasound transducers is demonstrated, while also presenting further evaluation of the imaging probe for its intended application.

Chapter 4 covers the design and evaluation of imaging schemes for the fabricated probes. They use 30°×30° diverging TX beams per pulse-echo acquisition, where they differ in the amount of beams transmitted per reconstructed image, and in whether TDM or synthetic aperture imaging is used. While all schemes are suited for evaluating the volume of interest, they mainly trade-off image resolution for volume-rate. Therefore, the achievable resolution and performance when imaging fast moving targets are also compared.

Chapter 5 summarizes the main findings and contributions of this work, and discusses potential points of improvement for the system. This is covered for both the near- and long-term. Additionally, future methodological performance evaluation improvements are discussed.

1

References

[1] World Health Organization. "Cardiovascular Diseases," Accessed: Apr. 2, 2025. [Online]. Available at: https://www.who.int/health-topics/cardiovascular-diseases#tab=tab_1.

[2] V. Kessler, J. Klopf, W. Eilenberg, C. Neumayer, and C. Brostjan, "AAA revisited: A comprehensive review of risk factors, management, and hallmarks of pathogenesis," *Biomedicines*, vol. 10, no. 1, 2022, ISSN: 2227-9059. [Online]. Available at: https://www.mdpi.com/2227-9059/10/1/94.

[3] J. Golledge, S. Thanigaimani, J. T. Powell, and P. S. Tsao, "Pathogenesis and management of abdominal aortic aneurysm," *European Heart Journal*, vol. 44, no. 29, pp. 2682–2697, Jun. 2023, ISSN: 0195-668X. DOI: 10.1093/eurheartj/ehad386. eprint: https://academic.oup.com/eurheartj/article-pdf/44/29/2682/51017100/ehad386.pdf. [Online]. Available at: https://doi.org/10.1093/eurheartj/ehad386.

[4] A. Wanhainen et al., "Editor's choice – european society for vascular surgery (ESVS) 2024 clinical practice guidelines on the management of abdominal aorto-iliac artery aneurysms☒," *European Journal of Vascular and Endovascular Surgery*, vol. 67, no. 2, pp. 192–331, 2024, ISSN: 1078-5884. DOI: https://doi.org/10.1016/j.ejvs.2023.11.002. [Online]. Available at: https://www.sciencedirect.com/science/article/pii/S1078588423008894.

[5] A. England and R. Mc Williams, "Endovascular aortic aneurysm repair (evar)," *The Ulster medical journal*, vol. 82, no. 1, p. 3, 2013.

[6] UMC Utrecht. "Endovasculaire aneurysma behandeling van de grote lichaamsslagader (evar procedure)," Accessed: Mar. 4, 2025. [Online]. Available at: https://www.umcutrecht.nl/nl/behandeling/endovasculaire-aneurysma-behandeling-van-de-grote-lichaamsslagader-evar-procedure/folder.

[7] Erasmus MC Medical Center. "Patiëntenfolder endovasculaire behandeling van een aneurysma (verwijding) in de grote lichaamsslagader (aorta)," Accessed: Mar. 24, 2025. [Online]. Available at: https://www.erasmusmc.nl/nl-nl/patientenfolders/endovasculaire-behandeling-van-een-aneurysma-verwijding-in-de-grote-lichaamsslagader-aorta-fldr-vwjj1603177962twl4#2d86d074-3ad9-4e74-8057-564ce4e1414d.

[8] Stanford Medicine. "Abdominal Aortic Aneurysm (AAA) Open Repair," Accessed: Mar. 5, 2025. [Online]. Available at: https://stanfordhealthcare.org/medical-conditions/blood-heart-circulation/abdominal-aortic-aneurysm/treatments/abdominal-aortic-aneurysm-open-repair.html.

[9] Erasmus MC. "Aorta aneurysma operatie van de grote lichaamsslagader (aorta)," Accessed: Mar. 5, 2025. [Online]. Available at: https://www.erasmusmc.nl/nl-nl/patientenzorg/operaties/aorta-aneurysma#4b0681f9-8901-41de-97ec-9dcb4b06db7b.

[10] M. Johansson, P. H. Zahl, V. Siersma, K. J. Jørgensen, B. Marklund, and J. Brodersen, "Benefits and harms of screening men for abdominal aortic aneurysm in sweden: A registry-based cohort study," *The Lancet*, vol. 391, no. 10138, pp. 2441–2447, 2018, ISSN: 0140-6736. DOI: https://doi.org/10.1016/S0140-6736(18)31031-6. [Online]. Available at: https://www.sciencedirect.com/science/article/pii/S0140673618310316.

[11] Health Council of the Netherlands, "Population-based screening for abdominal aortic aneurysm (AAA)," *The Hague: Health Council of the Netherlands*, no. 2019/10, 2019.

[12] J. Powell, S. Gotensparre, M. Sweeting, L. Brown, F. Fowkes, and S. Thompson, "Rupture rates of small abdominal aortic aneurysms: A systematic review of the literature," *European Journal of Vascular and Endovascular Surgery*, vol. 41, no. 1, pp. 2–10, 2011, ISSN: 1078-5884. DOI: https://doi.org/10.1016/j.ejvs.2010.09.005. [Online]. Available at: https://www.sciencedirect.com/science/article/pii/S1078588410005289.

[13] I. De Groot, G. Ligtenberg, and S. Vijgen, "Endovasculaire behandeling van complexe aneurysmata van de aorta," *College voor zorgverzekeringen*, 2012.

[14] A. Mehta et al., "Long-term costs to medicare associated with endovascular and open repairs of infrarenal and complex abdominal aortic aneurysms," *Journal of Vascular Surgery*, vol. 80, no. 1, pp. 98–106, 2024, ISSN: 0741-5214. DOI: https://doi.org/10.1016/j.jvs.2024.03.017. [Online]. Available at: https://www.sciencedirect.com/science/article/pii/S0741521424004543.

[15] E. S. Lee et al., "Costs of abdominal aortic aneurysm care at a regional veterans affairs medical center with the implementation of an abdominal

aortic aneurysm screening program," *Journal of Vascular Surgery*, vol. 75, no. 4, pp. 1253–1259, 2022.

[16] B. M. Fadel et al., "Ultrasound imaging of the abdominal aorta: A comprehensive review," *Journal of the American Society of Echocardiography*, vol. 34, no. 11, pp. 1119–1136, 2021.

[17] I. Aly et al., "Cardiac ultrasound: An anatomical and clinical review," *Translational Research in Anatomy*, vol. 22, p. 100 083, 2021.

[18] A. J. Einstein, K. W. Moser, R. C. Thompson, M. D. Cerqueira, and M. J. Henzlova, "Radiation dose to patients from cardiac diagnostic imaging," *Circulation*, vol. 116, no. 11, pp. 1290–1305, 2007.

[19] Erasmus MC Medical Center. "Passantenprijslijst 2025," Accessed: Mar. 28, 2025. [Online]. Available at: https://www.erasmusmc.nl/-/media/erasmusmc/pdf/2-themaoverstijgend/passantenprijslijsten/2025/20241230-dot-passanten-2025-versie-voor-communicatie_definitief.pdf.

[20] C. Chen and M. A. P. Pertijs, "Integrated transceivers for emerging medical ultrasound imaging devices: A review," *IEEE Open Journal of the Solid-State Circuits Society*, vol. 1, pp. 104–114, 2021. DOI: 10.1109/OJSSCS.2021.3115398.

[21] Y. Zhang and A. Demosthenous, "Integrated circuits for medical ultrasound applications: Imaging and beyond," *IEEE Transactions on Biomedical Circuits and Systems*, vol. 15, no. 5, pp. 838–858, 2021. DOI: 10.1109/TBCAS.2021.3120886.

[22] Y. M. Hopf et al., "A pitch-matched high-frame-rate ultrasound imaging ASIC for catheter-based 3-D probes," *IEEE Journal of Solid-State Circuits*, vol. 59, no. 2, pp. 476–491, 2024. DOI: 10.1109/JSSC.2023.3299749.

[23] P. Guo et al., "A 125 μ m-pitch-matched transceiver ASIC with micro-beamforming ADC and multi-level signaling for 3-D transfontanelle ultrasonography," *IEEE Journal of Solid-State Circuits*, pp. 1–14, 2024. DOI: 10.1109/JSSC.2024.3355854.

[24] J. M. Rothberg et al., "Ultrasound-on-chip platform for medical imaging, analysis, and collective intelligence," *Proceedings of the National Academy of Sciences*, vol. 118, no. 27, e2019339118, 2021.

[25] R. Wodnicki, J. Zhang, Q. Zhou, J. Foiret, C. Notard, and K. W. Ferrara, "Electronically scanned large apertures for interventional and diagnostic liver," in *2023 IEEE International Ultrasonics Symposium (IUS)*, 2023, pp. 1–4. DOI: 10.1109/IUS51837.2023.10306431.

[26] T. L. Szabo and P. Kaczkowski, *Essentials of Ultrasound Imaging*. Elsevier, 2023.

[27] A. G. Fraser, M. J. Monaghan, A. F. van der Steen, and G. R. Sutherland, "A concise history of echocardiography: Timeline, pioneers, and landmark publications," *European Heart Journal-Cardiovascular Imaging*, vol. 23, no. 9, pp. 1130–1143, 2022.

[28] V. C.-C. Wu and M. Takeuchi, "Three-dimensional echocardiography: Current status and real-life applications," *Acta Cardiologica Sinica*, vol. 33, no. 2, p. 107, 2017.

[29] L. W. Schmerr, *Fundamentals of Ultrasonic Phased Arrays*. Springer, 2015, pp. 20–24.

[30] T. Misaridis and J. Jensen, "Use of modulated excitation signals in medical ultrasound. part i: Basic concepts and expected benefits," *IEEE Transactions on Ultrasonics, Ferroelectrics, and Frequency Control*, vol. 52, no. 2, pp. 177–191, 2005. DOI: 10.1109/TUFFC.2005.1406545.

[31] T. Misaridis and J. Jensen, "Use of modulated excitation signals in medical ultrasound. part ii: Design and performance for medical imaging applications," *IEEE Transactions on Ultrasonics, Ferroelectrics, and Frequency Control*, vol. 52, no. 2, pp. 192–207, 2005. DOI: 10.1109/TUFFC.2005.1406546.

[32] T. Misaridis and J. Jensen, "Use of modulated excitation signals in medical ultrasound. part iii: High frame rate imaging," *IEEE Transactions on Ultrasonics, Ferroelectrics, and Frequency Control*, vol. 52, no. 2, pp. 208–219, 2005. DOI: 10.1109/TUFFC.2005.1406547.

[33] A. Ramalli, A. Dallai, E. Boni, F. Guidi, S. Ricci, and P. Tortoli, "Real-time pulse compression in multigate spectral doppler imaging," in *2015 IEEE International Ultrasonics Symposium (IUS)*, 2015, pp. 1–4. DOI: 10.1109/ULTSYM.2015.0418.

[34] P. Song, M. W. Urban, A. Manduca, J. F. Greenleaf, and S. Chen, "Coded excitation plane wave imaging for shear wave motion detection," *IEEE Transactions on Ultrasonics, Ferroelectrics, and Frequency Control*, vol. 62, no. 7, pp. 1356–1372, 2015. DOI: 10.1109/TUFFC.2015.007062.

[35] R. P. Zangabad et al., "Real-time coded excitation imaging using a cmut-based side looking array for intravascular ultrasound," *IEEE Transactions on Ultrasonics, Ferroelectrics, and Frequency Control*, vol. 68, no. 6, pp. 2048–2058, 2021. DOI: 10.1109/TUFFC.2021.3054971.

[36] V. Perrot, M. Polichetti, F. Varray, and D. Garcia, "So you think you can das? a viewpoint on delay-and-sum beamforming," *Ultrasonics*, vol. 111, p. 106 309, 2021.

[37] E. Moisello, L. Novaresi, E. Sarkar, P. Malcovati, T. L. Costa, and E. Bonizzoni, "Pmut and cmut devices for biomedical applications: A review," *IEEE Access*, vol. 12, pp. 18 640–18 657, 2024. DOI: 10.1109/ACCESS.2024.3359906.

[38] R. S. Reneman and A. Hoeks, "Continuous wave and pulsed doppler flowmeters—a general introduction," *Echocardiology: with Doppler applications and Real time imaging*, pp. 189–205, 1977.

[39] J. Luo, K. Fujikura, L. S. Tyrie, M. D. Tilson, and E. E. Konofagou, "Pulse wave imaging of normal and aneurysmal abdominal aortas in vivo," *IEEE Transactions on Medical Imaging*, vol. 28, no. 4, pp. 477–486, 2009. DOI: 10.1109/TMI.2008.928179.

[40] G. Montaldo, M. Tanter, J. Bercoff, N. Benech, and M. Fink, "Coherent plane-wave compounding for very high frame rate ultrasonography and transient elastography," *IEEE Transactions on Ultrasonics, Ferroelectrics, and Frequency Control*, vol. 56, no. 3, pp. 489–506, 2009. DOI: 10.1109/TUFFC.2009.1067.

[41] J. Bercoff, "Ultrafast ultrasound imaging," *Ultrasound imaging-Medical applications*, pp. 3–24, 2011.

[42] L. C. Jansen, H.-M. Schwab, F. N. van de Vosse, M. R. H. M. van Sambeek, and R. G. P. Lopata, "Local and global distensibility assessment of abdominal aortic aneurysms in vivo from probe tracked 2D ultrasound images," *Frontiers in Medical Technology*, vol. 4, 2023, ISSN: 2673-3129. DOI: 10.3389/fmedt.2022.1052213. [Online]. Available at: https://www.frontiersin.org/articles/10.3389/fmedt.2022.1052213.

[43] M. van 't Veer et al., "Biomechanical properties of abdominal aortic aneurysms assessed by simultaneously measured pressure and volume changes in humans," *Journal of Vascular Surgery*, vol. 48, no. 6, pp. 1401–1407, 2008, ISSN: 0741-5214. DOI: https://doi.org/10.1016/j.jvs.2008.06.060. [Online]. Available at: https://www.sciencedirect.com/science/article/pii/S0741521408010999.

[44] B. S. Garra, "Elastography: History, principles, and technique comparison," *Abdominal imaging*, vol. 40, pp. 680–697, 2015.

[45] L. Marais et al., "Arterial stiffness assessment by shear wave elastography and ultrafast pulse wave imaging: Comparison with reference techniques in normotensives and hypertensives," *Ultrasound in medicine & biology*, vol. 45, no. 3, pp. 758–772, 2019.

[46] K. Riemer, M. Toulemonde, E. Rowland, C. Leow, M. Tang, and P. Weinberg, "4d blood flow and wall shear stress measured using volumetric ultrasound image velocimetry," in *2020 IEEE International Ultrasonics Symposium (IUS)*, IEEE, 2020, pp. 1–4.

[47] P. Santos, G. U. Haugen, L. Løvstakken, E. Samset, and J. D'hooge, "Diverging wave volumetric imaging using subaperture beamforming," *IEEE Transactions on Ultrasonics, Ferroelectrics, and Frequency Control*, vol. 63, no. 12, pp. 2114–2124, 2016. DOI: 10.1109/TUFFC.2016.2616172.

[48] J. H. Fonken, E. J. Maas, A. H. Nievergeld, M. R. Van Sambeek, F. N. Van de Vosse, and R. G. Lopata, "Ultrasound-based fluid-structure interaction modeling of abdominal aortic aneurysms incorporating pre-stress," *Frontiers in Physiology*, vol. 12, p. 717 593, 2021.

[49] X. Sun et al., "Four-dimensional (4d) ultrasound shear wave elastography using sequential excitation," *IEEE Transactions on Biomedical Engineering*, vol. 72, no. 2, pp. 786–793, 2025. DOI: 10.1109/TBME.2024.3472689.

[50] R. Lopata, E. Maas, M. Thirugnanasambandam, E. van Disseldorp, and M. van Sambeek, "Ultrasound imaging for aortic biomechanics," in *Biomechanics of the Aorta*, Elsevier, 2024, pp. 139–162.

[51] J. Provost et al., "3D ultrafast ultrasound imaging in vivo," *Physics in Medicine & Biology*, vol. 59, no. 19, p. L1, Sep. 2014. DOI: 10.1088/0031-9155/59/19/L1. [Online]. Available at: https://dx.doi.org/10.1088/0031-9155/59/19/L1.

[52] K. Riemer, M. Toulemonde, E. M. Rowland, C. H. Leow, M.-X. Tang, and P. D. Weinberg, "4D blood flow and wall shear stress measured using volumetric ultrasound image velocimetry," in *2020 IEEE International Ultrasonics Symposium (IUS)*, 2020, pp. 1–4. DOI: 10.1109/IUS46767.2020.9251636.

[53] L. C. Jansen, S. Fekkes, H.-M. Schwab, and R. G. Lopata, "Increasing abdominal aortic aneurysm curvature visibility using 3D dual probe bistatic ultrasound imaging combined with probe translation," *Ultrasonics*, vol. 139, p. 107 284, 2024, ISSN: 0041-624X. DOI: https://doi.org/10.1016/j.ultras.2024.107284. [Online]. Available at: https://www.sciencedirect.com/science/article/pii/S0041624X24000465.

[54] A. Ramalli, E. Boni, A. S. Savoia, and P. Tortoli, "Density-tapered spiral arrays for ultrasound 3-D imaging," *IEEE Transactions on Ultrasonics, Ferroelectrics, and Frequency Control*, vol. 62, no. 8, pp. 1580–1588, 2015. DOI: 10.1109/TUFFC.2015.007035.

[55] J. A. Jensen et al., "Anatomic and functional imaging using row–column arrays," *IEEE Transactions on Ultrasonics, Ferroelectrics, and Frequency Control*, vol. 69, no. 10, pp. 2722–2738, 2022. DOI: 10.1109/TUFFC.2022.3191391.

[56] Y. Igarashi et al., "Single-chip 3072-element-channel transceiver/128-subarray-channel 2-D array IC with analog RX and all-digital tx beamformer for echocardiography," *IEEE Journal of Solid-State Circuits*, vol. 54, no. 9, pp. 2555–2567, 2019. DOI: 10.1109/JSSC.2019.2921697.

[57] Verasonics, *Vantage specifications for biomedical & general applications*, English, Verasonics, 2024, 4 pp., February, 2024.

[58] R. Van Schaijk and M. Devices, "CMUT: a versatile and low cost ultrasonic platform," in *Micromachined Ultrasonic Transducers 2019*, Philips Innovation Serv., 2019. Accessed: Mar. 2, 2025. [Online]. Available at: https://www.salland.com/wp-content/uploads/2019/06/11-Rob-van-Schaijk-Philips-InS-MEMS-Seminar-2019.pdf.

[59] R. van Schaijk, M. in 't Zandt, P. Robaeys, M. Slotboom, J. Klootwijk, and P. Bekkers, "Reliability of collapse mode cmut," in *2023 IEEE International Ultrasonics Symposium (IUS)*, 2023, pp. 1–4. DOI: 10.1109/IUS51837.2023.10307882.

[60] C. D. Herickhoff and R. van Schaijk, "Cmut technology developments," *Zeitschrift für Medizinische Physik*, vol. 33, no. 3, pp. 256–266, 2023.

2

A CMUT-on-ASIC Probe Design for 3D High-Volume-Rate Large-Volume Abdominal Aorta Imaging

This chapter is based on the publication "A 2000-Volumes/s 3D Ultrasound Probe with Monolithically-Integrated 23×23-mm^2 4096-Element CMUT Array" in IEEE Journal for Solid State Circuits, vol. 60, no. 4, pp. 1397-1410, April 2025, doi: 10.1109/JSSC.2025.3534087

2.1. Introduction

As covered in Chapter 1, the goal is to design a probe with a 4096-element capacitive micromachined ultrasound transducer (CMUT) array, monolithically integrated on application-specific integrated circuits (ASICs) that apply channel-count reduction to reduce the amount of channels coming out of the probe to a manageable amount. Broadly, channel-count reduction techniques can be di-

vided into two categories: techniques that reduce channel count at the cost of a reduction in volume rate, and techniques that exploit RX signal characteristics to reduce channel count without reducing volume rate. The first category includes techniques such as micro-beamforming [1], [2], [3], [4], [5], [6], element summation [7] and/or synthetic aperture imaging [6], [7], [8], [9]. As each of these techniques requires multiple transmit/receive (T/R) acquisitions to reconstruct a volume, they can only be applied for high-volume-rate (HVR) imaging to a limited extent. With micro-beamforming [1], [2], [3], [4], [5], [6], the transducer array is divided into multiple sub-arrays, in which the RX signals per element are combined into a single channel by a delay-and-sum operation. This operation yields a preprogrammed directivity of the sub-array, i.e., only a smaller sub-volume is scanned with one single T/R acquisition. Therefore, scanning the full FoV requires multiple T/R acquisitions, which are combined to reconstruct the full volume. Element summation, i.e. summing without delaying [7], can be seen as a simplification of micro-beamforming, where the sub-arrays can only be 'forward' looking. As a result, the volume that can be imaged compared to micro-beamforming is reduced. Synthetic aperture imaging [6], [7], [8], [9] is a multiplexing (MUX) technique, in which only a subset of elements is selected during transmit (TX) and/or receive (RX) per acquisition, and all signals are combined in the later volume reconstruction step. However, multiple acquisitions are required to obtain a full volumetric data set, reducing volume rate. Moreover, since the recorded sub-volumes are captured sequentially, any motion in between the capturing leads to reconstruction artifacts [10], [11].

Techniques in the second category, which reduce channel count without sacrificing volume rate, include analog time-division multiplexing (TDM) [4], [12], [13], [14], frequency-division multiplexing (FDM) [15] or digital TDM (D-TDM) [3], [7]. These techniques exploit the limited bandwidth of element-level RX signals by modulating multiple signals onto a higher-bandwidth output channel. However, this introduces crosstalk (for TDM and FDM) or bit-errors (for D-TDM), leading to imaging artifacts. Moreover, these techniques are limited by the bandwidth of the cable that connects the probe to an imaging system, or by that of the system RX channel [16], [17]. As a result, practical ultrasound systems can only make limited use of these techniques.

Currently reported probes with ASICs also have constrained TX waveform programmability, resulting from limitations in their counter-based TX beamformer (TX BF) architecture [3], [6], [18], [19], on-chip pulsers [7], [20] and/or signal

distribution network [20]. The extent of this limitation varies per design. For instance, some designs can transmit an arbitrary pulse train, with a semi-fixed duty cycle [3], [18]. The design in [20] provides more pulse shape programmability, but the waveform length and BF delays are restricted. These restrictions have been reduced with a BF that propagates a more freely programmable TX waveform across its array [7]. Nevertheless, no design has made both the pulse shape and length arbitrary to the same extent as probes with direct-element connections, trading off flexibility in TX waveform generation with system complexity, often precluding applications requiring more complex waveforms than simple pulses or pulse trains [21], [22].

This chapter covers a probe design that can image a 60°×60°×10 cm volume at 2000 volumes/s, which is sufficient to image the flow and wall motion of the abdominal aorta (AA), and is the highest volume-rate for designs with in-probe channel-count reduction reported to date. The full probe consists of 2 tiled ASICs, each monolithically integrated with a 32×64-element array of capacitive micromachined ultrasound transducers (CMUTs) with a 2.6 MHz center frequency. Each ASIC provides 8× channel-count reduction by means of 2×2 delay-and-sum microbeamformers (µBFs) and 2× TDM, thus exploiting the benefits of both techniques without reducing the frame rate below the acceptable limit (2000 volumes/s) or straining the requirements for the back-end receive system – Thus, the probe can interface with 2 commonly-used Verasonics Vantage-256 (VSX) imaging systems [16], [23], [24]. The µBF architecture in the ASIC is based on the design in [19], but provides an 80% larger delay range to image the specified FoV. TDM-induced crosstalk from channel-bandwidth limitations is mitigated with equalizers (EQs), consisting of finite-impulse-response (FIR) filters that the system trains with a pseudo-random bit sequence (PRBS) generated on chip. By calibrating the frequency response of each channel, the on-chip cable driver bandwidth can be reduced, in turn making the system more power efficient.

The probe also contains a novel TX BF that provides a high degree of flexibility in TX waveform definition, while having a relatively low system complexity. It steers arbitrary pulse-density modulated (PDM) waveforms to 2-level 65 V unipolar pulsers, driving each element. Similar to the TX BF presented in [7], waves are propagated across the array by means of programmable delay cells, integrated per element. However, the presented probe does so in a row-column fashion, rather than with a delay mesh. This simplifies the per-element TX BF logic, while maintaining the ability to define arbitrary BF delays.

This chapter is structured as follows. Section 2.2 covers the design requirements for the intended application and the associated system architecture. Section 2.3 covers the circuit design of the ASICs and Section 2.4 covers their integration with CMUTs and packaging. Section 2.5 presents the characterization and imaging results of fabricated prototypes. The paper ends with Section 2.6, which contains a comparison to prior designs and a conclusion.

2.2. System Design

2.2.1. Application & System Overview

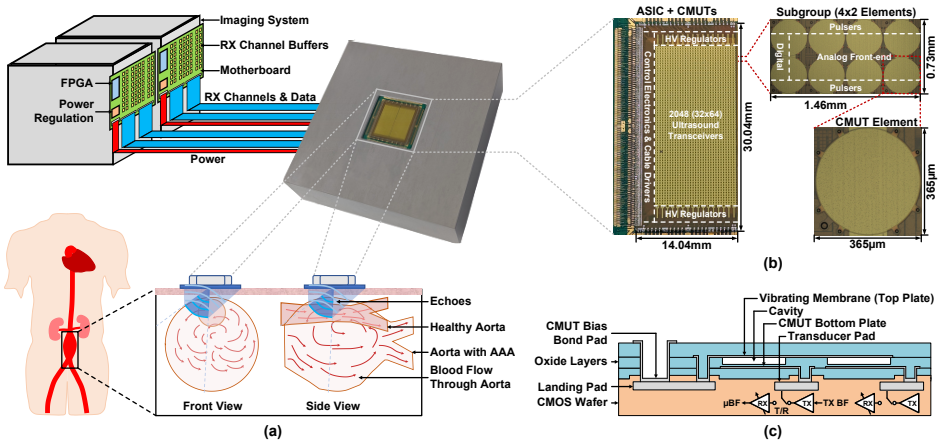

Figure 2.1: (a) Overview of the developed system and its application. (b) Overview of an ASIC + CMUTs and a breakdown of the replicated modules. (c) Simplified cross-section of the CMUT design.

Figure 2.1(a) shows an overview of the developed system and its application. It consists of the imaging probe with ASICs plus CMUTs, the aperture of which is divisible in two halves (tiles) that can independently interface with a system back-end. This consists of two duplicate motherboards and imaging systems. Each motherboard buffers the RX channels from one tile, regulates its various supplies and contains an FPGA to configure the probe. The imaging systems digitize the RX signals and do image reconstruction.

Although the main targeted application is imaging of the AA, the features of the probe are equally applicable in other parts of the cardiovascular system, such as

the heart [25]. The probe's packaging was designed to be compatible with various research setups by having a flat waterproof front-side and various mounting points at the back of the casing. This packaging is covered in more detail in Section 2.4.

Figure 2.1(b) shows an overview of one tile. It consists of two independent 32×32-element halves that are subdivided into 4×2-element subgroups reducing the echo signals received by the 8 subgroup elements to one output RX channel. These are routed to the periphery of the chip, where they are buffered and connected to the off-chip system back-end.

Figure 2.1(c) shows the simplified monolithically-integrated CMUT layer stack. The CMUTs are Philips 365-µm-pitch CM5 devices [26], [27] and have been fabricated on an ASIC that is made with a TSMC 0.18 µm bipolar-CMOS-DMOS (BCD) process. This process provides both high-voltage (HV) double-diffused metal-oxide-semiconductor (DMOS) and low-voltage (LV) complementary metal-oxide semiconductor (CMOS) devices, the former being required for the on-chip TX circuits and the latter for the RX circuits and logic. Each CMUT connects to a TX and RX front end, which are separated with a T/R switch. Although the probe presented in this work contains CMUTs, both the RX and TX front-ends have been designed to also be compatible with bulk-piezo transducers (PZT), similar to those used in [6], [19], but at a lower frequency.

2.2.2. Architecture

Figure 2.2 shows the system architecture implemented in the presented design. Because each tile is subdivided in independent ASIC halves, the full probe consists of independently operable quarters. Each ASIC half contains periphery circuitry and a core that consists of an array of subgroups. The system clock ($\mathrm{CLK_{SYST}}$) operates at a frequency (f_{SYST}) of 31.25 MHz, which defines a time resolution ($\mathrm{T_{SYST}}$) for both the TX BF and µBF of 32 ns.

The probe targets a 10 cm imaging depth. Given the speed of sound in human tissue, the resulting maximum pulse-repetition frequency (PRF) is 7.7 kHz. To achieve the targeted volume-rate of ∼2000 volumes/s, the full volume of 60°×60°×10 cm needs to be reconstructed from at most 4 T/R acquisitions. As a result, to accommodate the µBF restrictions (covered later in this section) and to maximize the probe's round-trip dynamic range (DR), the 4 targeted TX beams diverge 30° in both azimuth and elevation directions. However, in order to freely configure the probe for other imaging modes, narrower angles in both

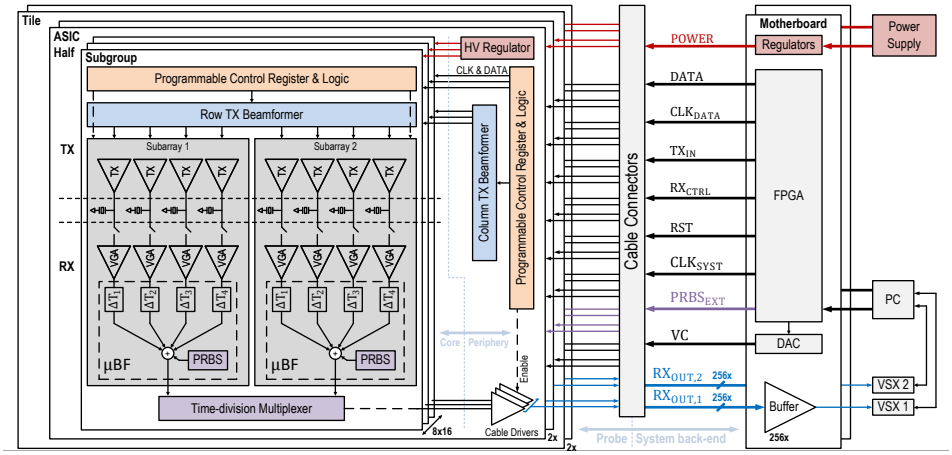

Figure 2.2: Overview of the developed system architecture.

azimuth and/or elevation may be desired. Therefore the probe is capable of freely configuring its delay profile for each T/R cycle.

Figure 2.3(a) shows the TX BF architecture. It contains a column and row section, each consisting of an array of delay cells. The column section is located at the ASIC periphery. By means of an input-selection multiplexer, each cell can either take the external PDM-modulated input TX_{IN} (indicated with 'E' on the multiplexer), or take its input from a neighboring cell (indicated with vertical arrows on the multiplexer). This allows the signal to propagate vertically and be passed to the row sections. Similarly, the cells in each row take either the output of the corresponding column cell or of a neighbor, as indicated with the 'R' and the horizontal arrows, respectively, in the row-cell input-selection mux, propagating the signal horizontally. Both row and column cells implement a delay range of 0-7 clock periods (delays are indicated with the δ-blocks). This provides a cumulative delay range of $7 \times (64 + 64) \times T_{SYST} \approx 28.7$ µs across the array, as needed to implement the maximum delay difference between elements in the array. Because the TX BF only delays TX_{IN}, the waveform can have an arbitrary shape and length.

The TX BF is programmed with a shift-register (SR) that is controlled by an external data and clock signal. As shown in Figure 2.3(b), the TX BF can be programmed in a row-column fashion for optimal speed, or in a daisy-chain fashion for optimal flexibility. Figure 2.3(c) provides a few example delay profiles and their corresponding programmed settings with this TX BF. As indicated, the arbitrary

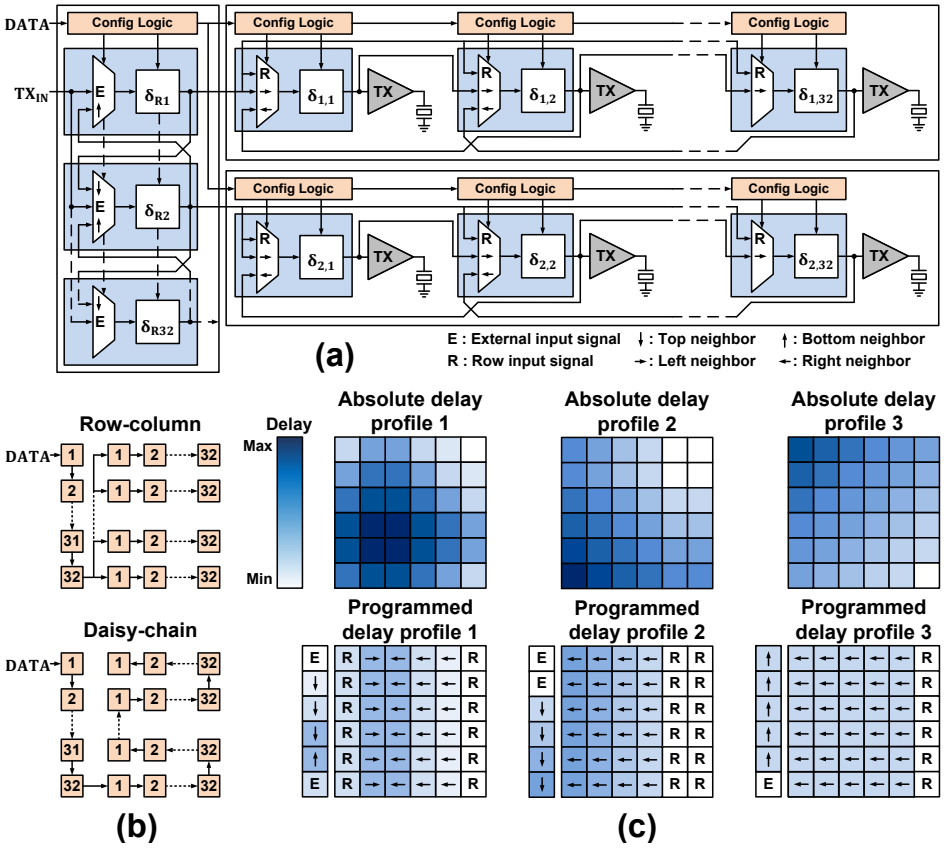

Figure 2.3: (a) TX BF architecture. (b) Overview of programming configuration modes. (c) Example delay profiles and programmed settings for a simplified 6×6 array. Profile 1 is an angled focused beam, profile 2 is an angled diverging beam and profile 3 is an angled plane wave.

sum of delays in both column and rows provide a wide range of waveforms that can be generated. Implementation details of the TX BF are discussed in Section 2.3.1.

In TX, CMUTs are driven element-level with a 2-level unipolar pulser. Although the pulser is capable of producing pulses with amplitudes between 5 V and 65 V, the transmit voltage is limited to 40 V. This ensures that the CMUTs remain in collapse mode and operate reliably when biased at +120 V at their AC ground [27]. The HV regulator at the ASIC periphery provides an additional supply for the pulser, which will be covered in Section 2.3.2.

For RX, each CMUT connects to a low-noise variable-gain amplifier (VGA).

As ultrasound waves exponentially attenuate with distance in human tissue, the round-trip DR per T/R cycle can be in the order of 100 dB [3], [18]. However, signal-to-noise ratio (SNR) requirements are typically only 40 dB. Therefore, the RX front-end implements time-gain-compensation (TGC) to decouple the system's SNR from its DR, resulting in an improved average power dissipation. The VGA has a continuous-gain range of 36 dB, which is controlled by an external analog signal (VC).

Each 4×2-element subgroup is divided into two 2×2-element subarrays, the echo signals of which are combined using a µBF with a programmable delay between 0 and 8 clock periods. As a result of the summing operation involved with µBF, the FoV of each CMUT subarray reduces to 30°, thus requiring 2 viewing angles to cover a 60° FoV and 4 for a 60°×60° FoV. As mentioned, the required 60°×60°×10 cm imaging volume is reconstructed from 4 T/R acquisitions using TX waveforms that cover a 30°×30° FoV, one for each quadrant. Therefore, the directivity of the µBFs can be configured such that the FoV in RX matches TX. Both the VGA and µBF are based on the design in [19], but the µBF in this design has an 80% larger delay range to enable proper matching of the TX and RX FoV.

TDM is realized by having one of two µBFs periodically provide its output to a cable driver at the ASIC periphery. To minimize the load of the cable drivers, each RX channel is buffered at the system back-end before entering a VSX system. The VSX systems digitize and equalize all RX channels to compensate bandwidth limitations of the cable drivers. This reduces their bandwidth requirements, allowing for more power-efficient scaling. The EQs are trained with an on-chip generated PRBS, covered in more detail in Section 2.5. Similar to the TX BF, the RX circuits can also be programmed in a row-column or daisy-chain fashion with a separate external data and clock signal.

2.3. Circuit Design

2.3.1. TX Beamformer

As indicated in Figure 2.3, the TX BF consists of element-level delay cells that provide a delay difference between elements before transmitting TX_{IN}. Figure 2.4 shows their implementation. As TX_{IN} is a PDM waveform that is sampled by CLK_{SYST}, it can be represented by a clocked binary sequence. Therefore, its delays can be implemented by a cascade of D-flip-flops (DFFs). To configure the

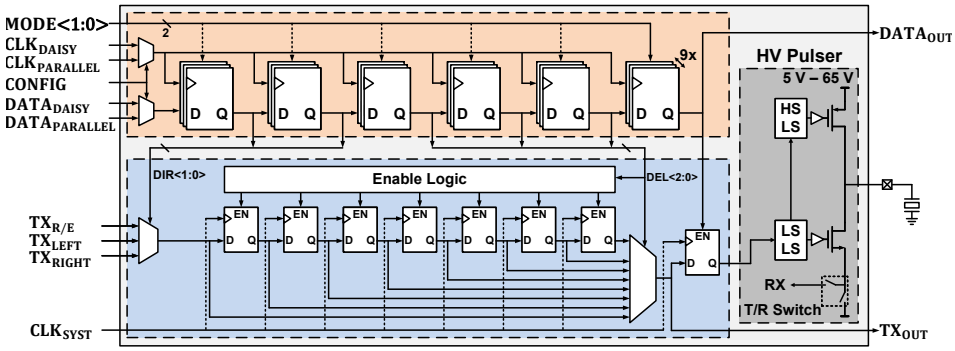

Figure 2.4: Implementation of the element-level TX BF and pulser. DEL<2:0> configures the signal delay, DIR<1:0> configures the signal propagation direction and 1 bit enables the element HV pulser.

per-element delays, the output of one of the cascaded DFFs is selected to be passed-on to the low-side level-shifters (LS LS) of the HV pulser, and neighboring delay cells (TX_{OUT}). The DFFs that are not used per delay cell are disabled to reduce switching losses.

The following 6 bits are used to configure each delay cell: a 3-bit delay code (DEL) for selecting the output of the delay DFF, a 2-bit select code (DIR) for selecting the input propagation direction and a 1-bit enable for the element HV pulser. To allow for fast switching between delay profiles, each cell contains 9×6 configuration DFFs, providing space for 9 pre-loaded profiles. Their upload settings are configured with 3 external control signals. The CONFIG signal controls the data upload fashion (see Figure 2.3(b)). The MODE<1:0> signal controls whether 1 or 9 profiles should be uploaded and whether the register should receive external data or loop previously uploaded local TX BF profile data per rising-edge of its input clock.

Each ASIC half contains one external data and clock signal for the TX BF registers (Figure 2.2), but they are split into two signals at the periphery. This allows them to be routed together for both upload modes, guaranteeing them to be in-phase for each delay cell, preventing possible bit errors.

2.3.2. TX Pulser

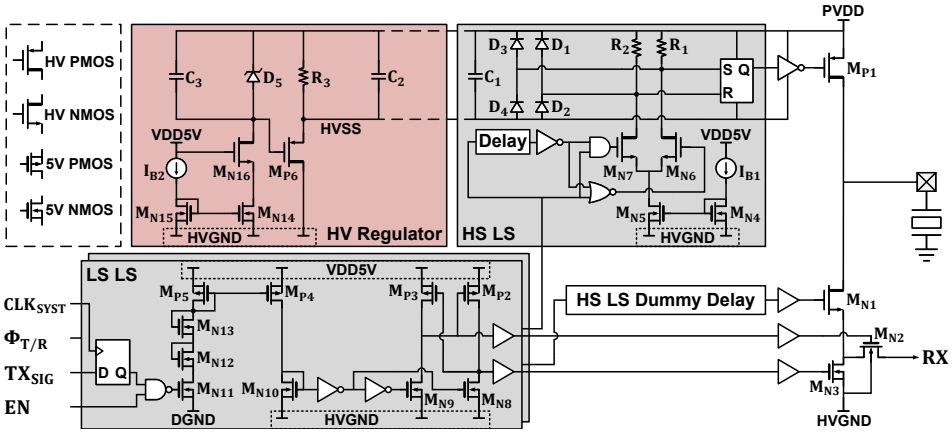

Figure 2.5: Implementation of the element-level pulser and HV regulator at the ASIC periphery.

Figure 2.5 shows the element-level pulser design. The unipolar pulser driver stage, consisting of M_{P1}, M_{N1}, M_{N2} and M_{N3}, is the same as the design in [18], [28], but with an improved guard-ring design for prevention of latch-up. The DMOS transistors M_{P1} and M_{N1} switch the output voltage level, whereas M_{N2} and M_{N3} implement the T/R switch, connecting the CMUT to the VGA through M_{N1} and M_{N2} during RX, while isolating it from HV pulsing during TX. M_{P1} was scaled for driving strength, M_{N1} was scaled for driving strength and noise, M_{N2} was scaled for noise, and M_{N3} was scaled to minimize voltage ripple at the source of M_{N1}.

Two LS LS [29] stages convert the digital supply domain (DVDD-DGND) input signals to the 5 V domain (VDD5V-HVGND) and drive the T/R switch, high-side level-shifter (HS LS) and M_{N1}. Due to the large trace inductances from the long supply routing across the array, the high-side (PVDD-HVSS), power (PVDD-HVGND) and 5 V domains can experience significant ripple when in TX mode. Therefore, the diode-connected M_{N12} and M_{N13} are added to limit the voltage swing over M_{N11} and M_{P5}. The LS LS output is a latch that implements a break-before-make function to ensure that M_{P1}/M_{N1} and M_{N2}/M_{N3} are not on at the same time. The HS LS propagation delay is compensated with a dummy delay before the driver of M_{N1}.

The HS LS is based on the design in [30]. Its output is defined by a HS latch that operates in hold mode when both set and reset are '1' or '0', providing a high robustness against supply ripple. The latch is set or reset by means of pulsed

inputs, generated through the IR drop across resistors R_1 and R_2 and the current drawn by a LS current-mirror, which is steered through DMOS transistors M_{N6} and M_{N7}. The pulse width is derived from a delay cell with a delay larger than the propagation delay of the TX signal through the HS LS and the HV pulser to ensure that the state of the HS latch does not change while the supply is most active.

The HS LS is powered by the pulser supplies PVDD and HVGND. PVDD can be varied between 5 V and 65 V. The HVSS voltage, generated by a HV regulator at the ASIC periphery, is PVDD - 5 V. The regulator is the same as in [18], [28], while clamping diodes D_{1-4} are added per HS LS. These diodes ensure that the HS latch set and reset node voltages are kept between PVDD and HVSS ± diode voltage V_D. They also ensure that HVSS does not increase by more than V_D while the set or reset nodes are pulled down. This ensures reliable operation of the HS LS while transmitting longer pulse sequences, as the local supply capacitor C_1 can be recharged without transient currents from the regulator at the periphery, thus avoiding excessive voltage ripple at HVSS.

2.3.3. Variable-Gain Amplifier

The VGA is based on the design in [19], [31]. As shown in Figure 2.6, it consists of a cascaded low-noise capacitive-feedback trans-impedance amplifier (TIA), capacitively-coupled to a current amplifier (CA). The TIA provides a low-impedance input for interfacing with a CMUT transducer, while the CA has a high-impedance output for driving the boxcar-integration-based µBF. Both stages implement half the total variable continuous gain range of 36 dB, which is controlled by a VC that is supplied per ASIC half. The VGA is scaled for an input-referred noise-density of 0.6 pA/$\sqrt{\text{Hz}}$ within a 1.4-to-3.8-MHz bandwidth at its maximum gain (VC = 1.2 V).

2.3.4. RX Channel-Count Reduction and Transmission

Figure 2.6 shows the µBF and TDM circuit diagram. Like in [19], the boxcar-integration-based µBF consists of 4 time-interleaved integrator stages, followed by 2 ping-ponged sample-and-hold (S/H) stages. The current outputs of the 4 preceding CAs are steered to one of the 4 integrators in a cyclic fashion by means

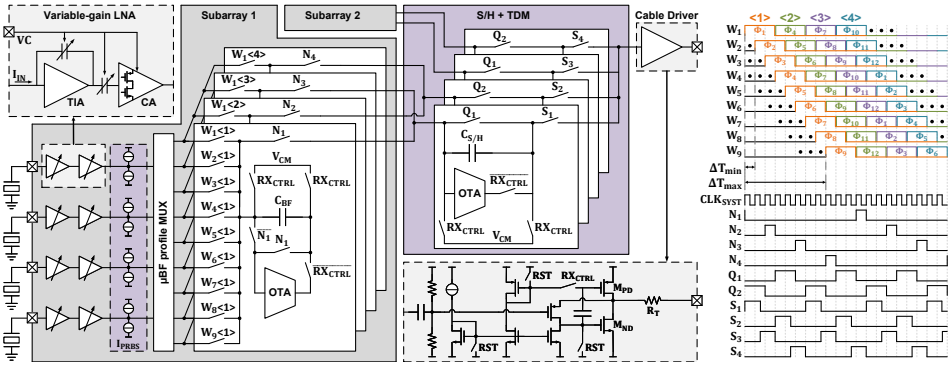

Figure 2.6: Implementation of the RX front-end and the timing diagram of its delay-and-sum µBF and S/H + TDM stages.

of input switches W_{1-9}<1:4>. The phases for the clocks driving W_{1-9}<1:4> are programmable, while the integrator output charge is transferred to the S/H stages at a fixed cyclic timing via clock signals N_{1-4} and Q_{1-2}. The S/H stage that is not in charge-transfer mode is connected to the output, following clock signals S_{1-4}. As the timing for the integrators and charge-transfer is fixed, but the timing of the input currents can be shifted, the relative delay between input integration and output S/H is programmable for each input channel. Thus, a sum-and-delay operation is realized.

Since switched S/H stages define the RX channel output, TDM is easily realized having 4 S/H stages drive the input of the following cable driver instead of 2. Conceptually, more than 2× TDM could be realized by interleaving more stages, but the channel-bandwidth of the targeted VSX back-end limits this design freedom. The cable driver is a super source follower with a class-AB driver [32]. Like the LNA and µBF OTAs, the class-AB driver has a sampled-and-held bias that is reset every T/R cycle by the RX_{CTRL} signal. M_{PD}, M_{ND} and R_T are scaled to achieve a 50 Ω output impedance.

2.3.5. Channel Equalization and Calibration

To reduce TDM channel crosstalk, after digitizing the RX channels in the VSX, equalization is applied to flatten the frequency response. This technique is based on what was demonstrated in [14]. The EQs are implemented as adaptive linear equalizers (ALEs) from the Matlab communications library [33]. This is a finite-

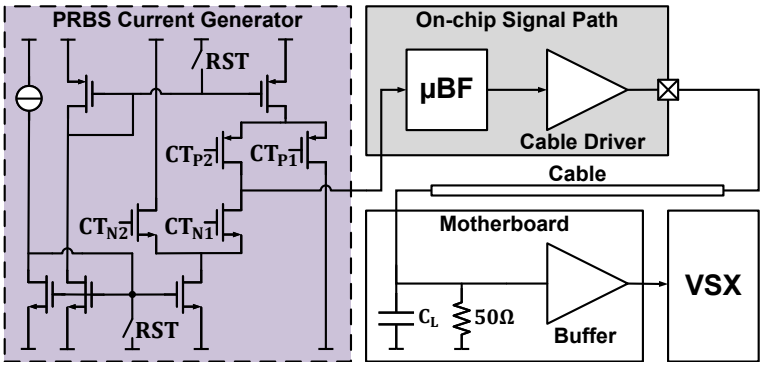

Figure 2.7: Circuit diagram of the I_{PRBS} current source generating training data for the EQ in the system back-end and the signal path that is equalized.

impulse-response FIR filter that uses the least-mean-square algorithm to scale its coefficients.

The training data for each RX channel EQ is generated on-chip with a programmable 2-level current source I_{PRBS} at each µBF input. The implementation of the current sources is shown in Figure 2.7. They output an off-chip supplied pseudo-random-bit-sequence (PRBS), which propagates through the on-chip µBF and cable driver, and the off-chip cable and buffer before being digitized by the VSX in the system back-end.

In addition to calibrating bandwidth-limitations, the system also calibrates static ripple signals at each RX channel output, resulting from switching artefacts introduced by the µBF. This is done by first collecting averaged RX channel data without an input signal, which only contains the ripple. This ripple is then subtracted from both the RX signals collected during imaging and the training data for the EQ.

2.4. System Integration

2.4.1. CMUT Integration

As mentioned in Section 2.2, the CMUTs are biased at a voltage V_{bias} of +120 V to reliably operate in collapse mode. The CMUT top electrodes (Figure 2.1(c)) are routed to the ASIC periphery to be bonded to the printed circuit board (PCB) that provides V_{bias}. Figure 2.8(a) shows the applied biasing scheme. The CMUTs

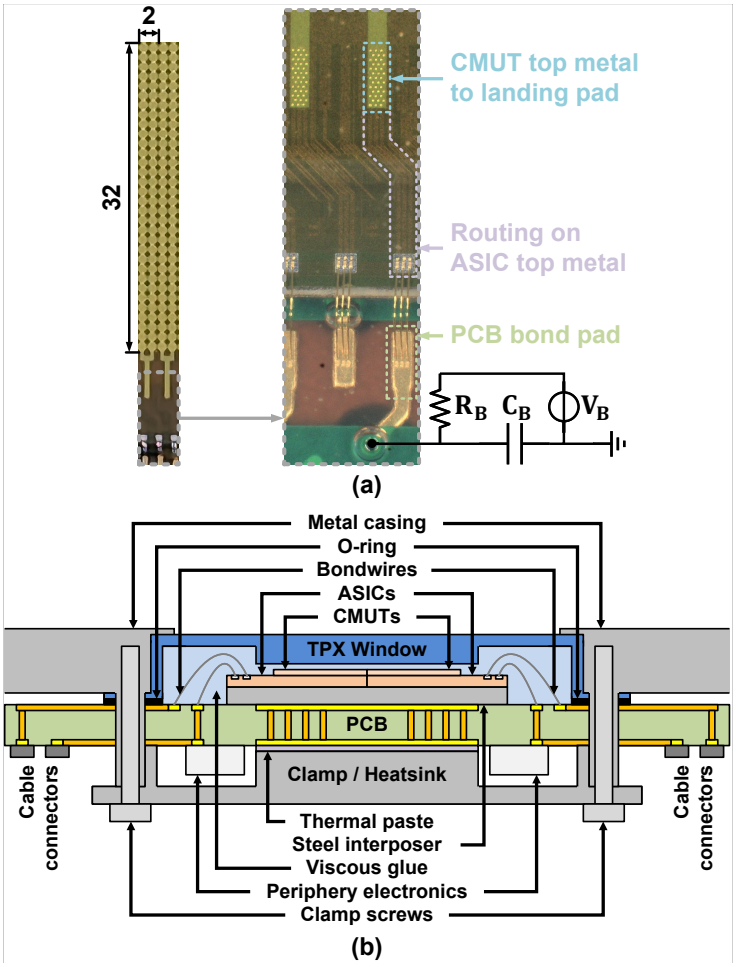

Figure 2.8: (a) Overview of the CMUT biasing per two columns of the imaging array. (b) Overview of the system packaging.

in every 2 columns of an ASIC half share one biasing pad. This allows only a section of the array to be disconnected if one or multiple CMUTs are faulty. Bias capacitor C_B provides an AC ground for the CMUTs, whereas the HV supply V_B only operates as a direct-current (DC) bias source by means of resistor R_B. As both the sensitivity and center frequency of the CMUTs depend on V_{bias} [27], independent biasing of CMUT columns along the x-axis of the array enables apodization. However, this is not done in the presented system, where $V_{bias} = +120$ V for simplicity.

To accommodate the CMUT devices on the standard TSMC BCD process wafers, a few layout restrictions were introduced. The microfabrication of the CMUTs requires a wafer surface topography that is as flat as possible. While the CMUT fabrication contains a planarization step, the top-metal thickness of the ASICs was also restricted as a precaution to improve the initial surface flatness, which added additional constraints to its power distribution design. Additionally, sufficient spacing is required all-around any in-ASIC CMUT bias trace to prevent dielectric breakdown, as the TSMC 180nm BCD process is not designed for trace-to-trace potential differences beyond 70 V.

2.4.2. Acoustic Packaging

To avoid excessive energy loss in both TX and RX, acoustic impedance matching of the array to the medium of interest is necessary. This requires a package with a similar impedance to water, while providing a water-tight seal for the underlying electronics. Additionally, the surface of the imaging aperture must be flat to ensure a good contact with the medium of interest. Figure 2.8(b) shows the designed package to meet these requirements.

The tiles are glued on an interposer plate that both ensures a flat imaging aperture and provides good thermal coupling to a PCB. After bonding the tiles to the PCB, a viscous glue is applied to the imaging array. This glue has a similar acoustic impedance to water while being electrically isolating. A Polymethylpentene (TPX) window is then mounted on the array, pushing the glue outwards, coupling the array to the window while sealing the bonding wires. To ensure water-tightness around the window, the PCB is mounted in an anodized-aluminum casing, where an O-ring provides the water-tight seal. Pressure is applied to the O-ring via a backside clamp that also functions as a heatsink for the ASICs.

2.5. Experimental Results & Discussion

2.5.1. General Measurement Setup

As shown in Figure 2.8(b) and Figure 2.9(a), each tile in the probe is bonded to a daughterboard PCB. In the measurements presented, the digital inputs and RX output channels of 1 tile are connected via 1.65 m Samtec micro-coax cables with

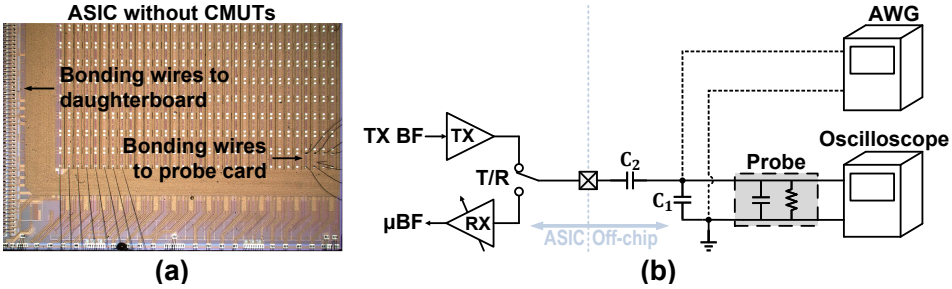

Figure 2.9: (a) Picture of one of the ASICs without CMUTs connected to a probe card. (b) Diagram of the measurement setup for 1 input channel.

HQCD connectors [34] to the system back-end. The FPGA module that programs the tile is a DE10-Nano evaluation board [35] and the RX channel buffers on the motherboard in the system back-end are high-speed op-amps [36] configured as voltage followers with 50 Ω input termination. In addition to voltage regulation on the motherboard by means of linear-drop-out regulators (LDOs), the analog supply is also regulated on the daughterboard to avoid TGC-related IR drop in the cables affecting the ASIC performance.

2.5.2. Electrical Characterization

ASICs without the monolithically-integrated CMUTs were used to validate both the electrical performance of the TX pulser and the RX front-ends. Selected transducer pads were bonded to a custom probe card. An overview of this measurement setup is shown in Figure 2.9(b). C_1, C_2 and the input capacitance of the 200 MHz passive probe approximate the load of a CMUT, while also attenuating the voltage from the HV TX pulsers on the ASIC by 13.4×. This attenuation was calibrated and corrected for in TX measurements. The oscilloscope is connected for both TX and RX measurements, but the AWG is only connected for RX.

Figure 2.10(a) shows the probed pulser output when transmitting various PDM waveforms at the maximum TX voltage of 65 V. The 2-period pulse is used for most standard imaging applications, but chirps or pseudo-random sequences can be used instead to increase the contrast from low-reflective objects, as these waveforms contain more energy. Figure 2.10(b) shows the corresponding acoustic outputs, which are covered in more detail in subsection 2.5.3. Figure 2.11 shows the pulser output when transmitting the same chirp as shown in Figure 2.10(a) after being

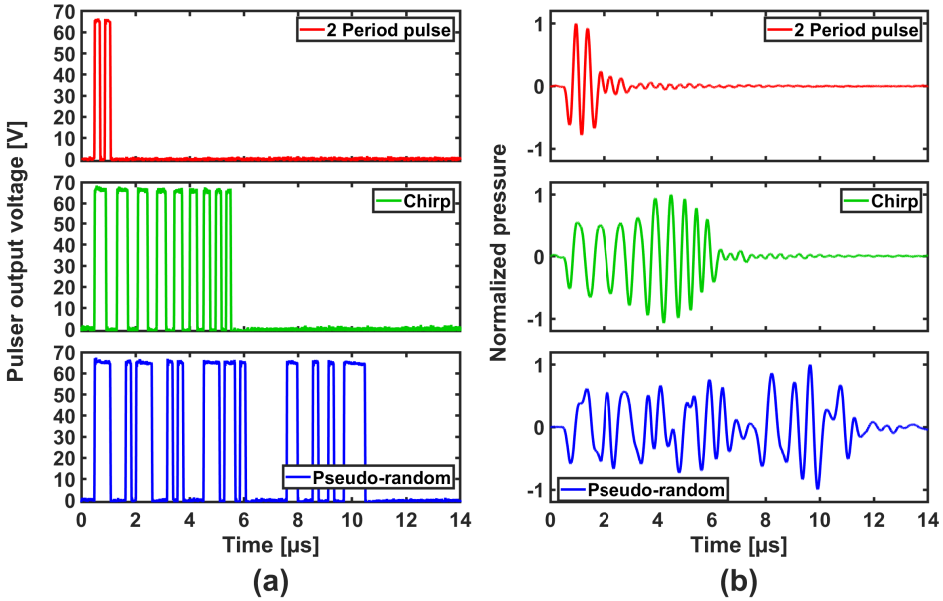

Figure 2.10: (a) Transducer pad output for various PDM signals at the maximum ASIC transmit amplitude. (b) Normalized transmitted acoustic signal corresponding to the transducer pad signals at a 40 V transmit amplitude.

delayed between 0 and $8T_{SYST}$ by the TX BF. Combining the results from Figure 2.10 and 2.11 demonstrates the ability to BF arbitrary PDM waveforms.

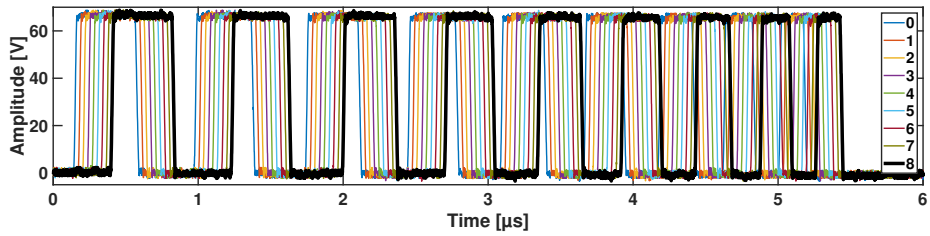

Figure 2.11: Pulser outputting a chirp sequence, shifted between 0 and $8T_{SYST}$ by the TX BF.

Figure 2.12(a) shows the subarray gain versus frequency for multiple TGC VC settings. Figure 2.12(b) shows the gain at the 2.6 MHz center frequency and -3-dB BW versus VC. The gain range is 36 dB and the BW varies from 3.0 MHz to 3.8 MHz across VC. Given a 1.4-MHz-to-3.8-MHz BW of interest and 2.6 MHz center frequency defined by the CMUTs, the fractional bandwidth of the amplifier

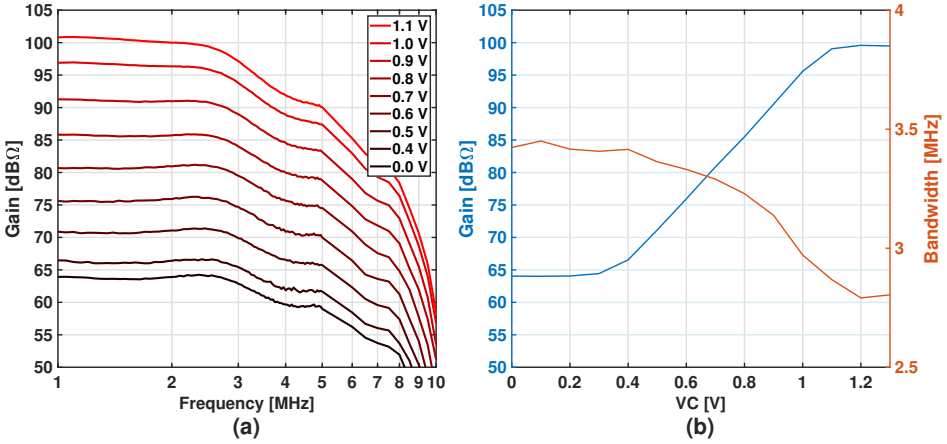

Figure 2.12: (A) Measured RX channel gain versus frequency for various VC settings. (B) Gain at 2.6 MHz and -3-dB BW versus the VC control voltage.

varies from ∼60% to ∼90%, which is more than the required 50% across the gain range. These results also approximate the same attenuation that will occur for the CMUT-to-LNA input current, as the impedance of C_2 is similar to that of the CMUT.

To validate the subgroup crosstalk, test signals are applied to an RX channel (Figure 2.9(a)). The EQs applied for the crosstalk measurements and imaging results (subsection 2.5.4) have 18 taps. They equalize the VSX 14-bit ADC output data, which is sampled at 3× the TDM frequency at 62.5 MHz. As such, the EQs are configured fractionally spaced, using 3 samples per symbol. They are trained with a 2500-times-repeated 16382-bit PRBS.

Figure 2.13(a) and Figure 2.13(b) show the crosstalk from subarray 1 to subarray 2 and vice-versa with and without back-end equalization in the time domain. The test signals are 2.6-MHz-center-frequency 2-period pulses. With equalization applied, the peak-peak crosstalk from subarray 1 to subarray 2 improves from -11.4 dB to -20.9 dB and from subarray 2 to subarray 1 from -10.9 dB to -21.4 dB.

Figure 2.13(c) and Figure 2.13(d) show the power spectral density (PSD) of the RX channel output when a 2.5 MHz tone is applied to the subarray inputs. The reduction in a µBF-induced ripple tone at 2.6 MHz is also shown after calibration. Figure 2.13(e) and Figure 2.13(f) show the crosstalk improvement when the frequency of the input tone is swept across the 1.4-MHz-to-3.8-MHz bandwidth of interest. The effectiveness of the equalization varies over frequency, but the aver-

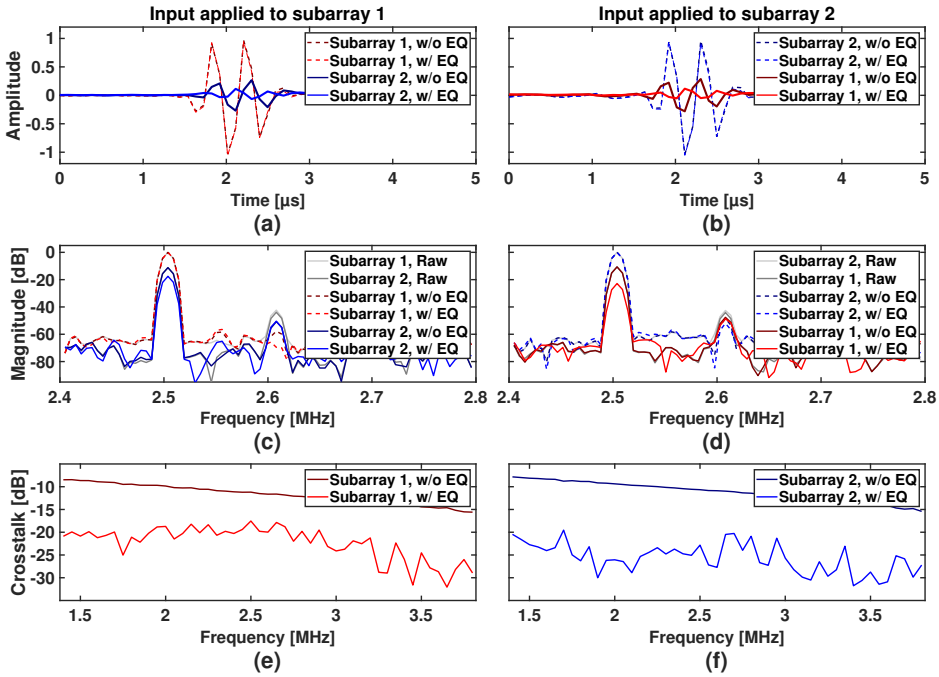

Figure 2.13: (a) Crosstalk from a pulse into subarray 1 to subarray 2. (b) Crosstalk from a pulse into subarray 2 to subarray 1. (c) Crosstalk from a 2.5 MHz tone into subarray 1 to subarray 2. (d) Crosstalk from a 2.5 MHz tone into subarray 2 to subarray 1. (e) Crosstalk from tones within the bandwidth of interest into subarray 1 to subarray 2. (f) Crosstalk from tones within the bandwidth of interest into subarray 2 to subarray 1.

age crosstalk from subarray 1 to subarray 2 improves to -22.4 dB and the average crosstalk from subarray 2 to subarray 1 to -25.7 dB.

As the power dissipation of the pulser is directly related to the pulse transmission density, Figure 2.14(a) shows the dissipation versus the number of transmitted pulse periods when an ASIC half is transmitting with no TX BF delays. This is shown for a prototype with and without CMUTs. As most imaging modes using this probe transmit a 2-period pulse per T/R cycle, the typical number of pulse periods/second is 16000 when imaging at 2000 volumes/s with 4 diverging waves per volume. The associated power/element drawn from the HV supply is 186 µW, which is much lower than the RX power dissipation.

A breakdown of the power dissipation of the probe is shown in Figure 2.14(b). All power dissipation was measured during active operation using a prototype

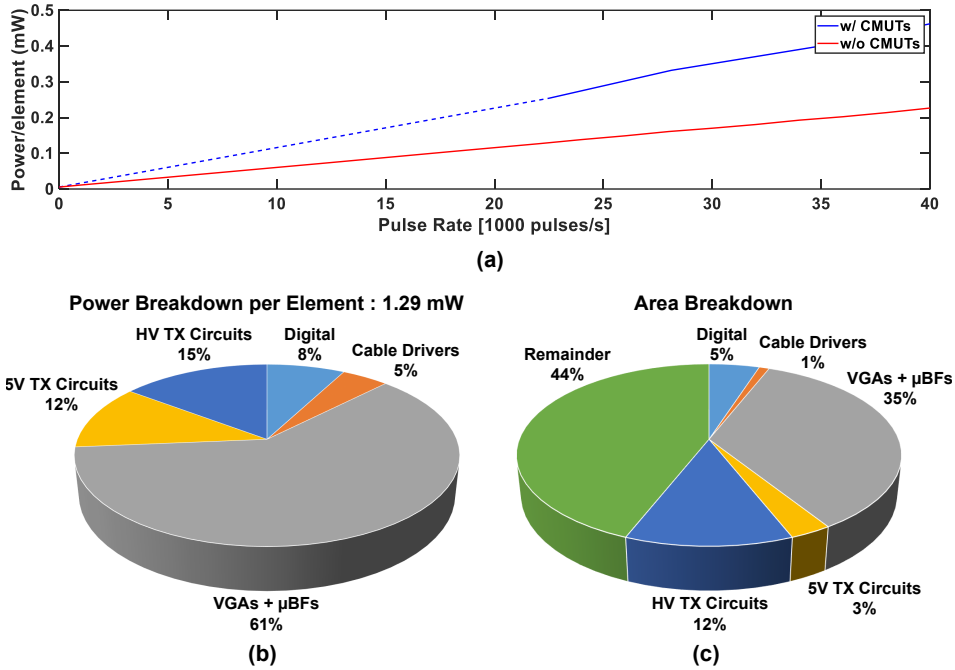

Figure 2.14: (a) Relation between the HV supply power/element and the amount of pulse periods transmitted, using a repeated chirp sequence as a test signal (Figure 2.10). The solid sections of the line are measured data points, while the dotted sections are from interpolation. (b) Element-referred power breakdown for 16 kperiods/s TX and VC ramping per T/R cycle. (c) Area breakdown of the tiles. The 'Remainder' category contains decoupling capacitors, bond pads, interconnect, ESD protection circuits and unused area.

with CMUTs. The pulse-repetition frequency (PRF) is 8 kHz, as needed for 2000 volumes/s imaging. However, to measure different parts of the RX circuitry independently, parts of the ASIC were disabled. The RX front-end dissipates 0.79 mW/El. when applying a ramp function to VC during each T/R cycle.

A breakdown of the ASIC area is shown in Figure 2.14(c). Although active circuits use most area, because of the pad-limited nature of the design, a substantial 44% of the total area consists of bond pads, pad protection circuitry, decoupling capacitors and interconnect. Of the active design, the RX front-end dominates with 36% of the total area, while the combined TX circuit only uses 15% of the total area.

2.5.3. Acoustic Characterization

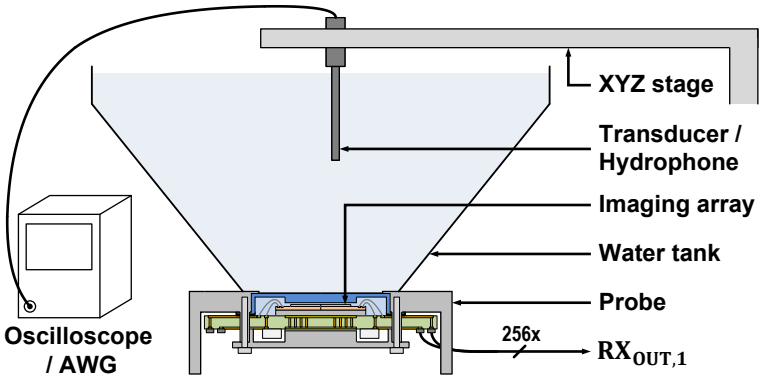

Figure 2.15: Acoustic measurement setup.

Figure 2.15 shows the measurement setup for the acoustic measurements. A 3D-printed water tank is placed on top of the ultrasound probe. The interface between the two consists of acoustic gel and a plastic bag with a thickness much lower than the 600 µm nominal wavelength of the ultrasound waves, thus not significantly attenuating signals. From the top of the water tank, an xyz stage with a holder positions imaging objects or instrumentation, depending on the measurement.

Figure 2.10(b) shows the measured normalized pressure of the transmitted waveforms using the driving signals shown in Figure 2.10(a). All elements on 1 tile were transmitting with no time delays. The waveforms were transmitted at the nominal maximum of the probe, where TX is limited to 40 V. As is shown, the probe is capable of producing a wide range of acoustic waveforms by means of the arbitrary PDM driving signal for the CMUTs.

Figure 2.16 demonstrates the TX BF functionality by comparing four scanned C-planes of TX beams with their ideal Field II [37] simulation result. These diverging beams are the same as used in the TX scheme for 60°×60°×10 cm 2000 vol/s imaging. As the results are presented for 1 tile, the imaging scheme only uses the central 32×32 elements, as a symmetrical transmit aperture is needed to create the desired symmetrical diverging waves.

The ASIC was configured to cycle through 9 pre-uploaded TX profiles, as it also does for HVR imaging. The C-plane has a 3.5 cm distance from the array. The peak-peak pressures were measured using a 200 µm diameter hydrophone and an

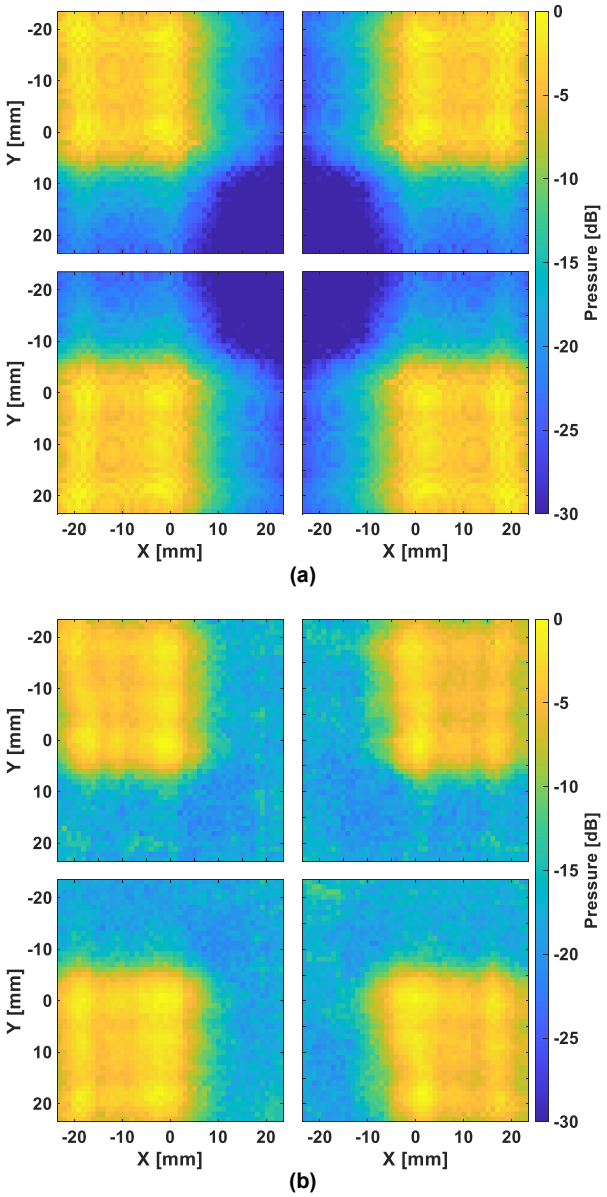

Figure 2.16: (a) Simulated C-planes at 3.5 cm from the probe for the diverging waves used in the TX scheme for imaging of 60°×60°×10 cm at 2000 vol/s. (b) Measured C-planes of the same TX waves at 3.5 cm from the probe.

xyz stage, scanning a grid of 4.6×4.6 cm with 1 mm steps. The PRF of the ASIC during this measurement is 18 kHz. As shown, the measured diverging waves are in good agreement with the simulations. The elevated clutter is from reflections in the water tank, originating from prior scan point transmissions.

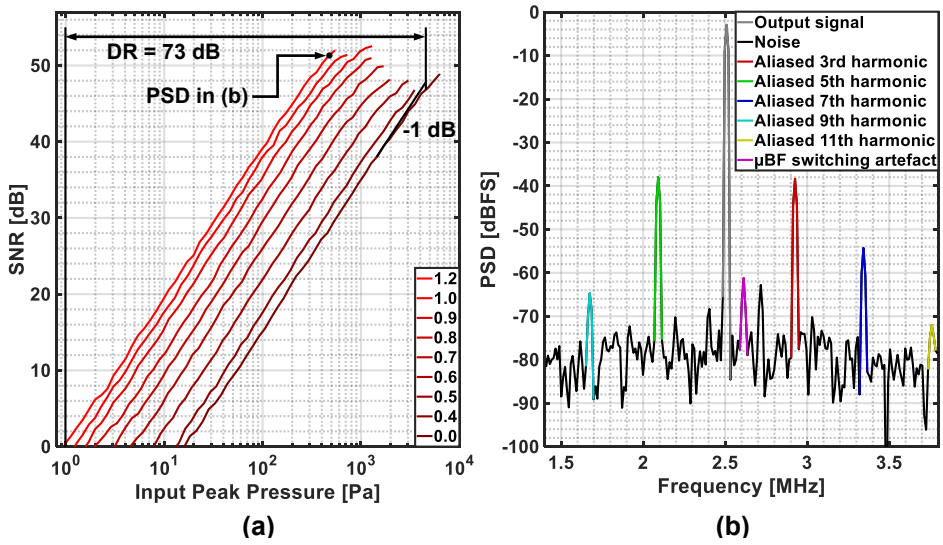

Figure 2.17: (a) Subarray SNR vs input peak pressure for varying VC control voltages. (b) Example PSD of output signal at high signal levels.

Figure 2.17(a) shows the output signal-to-noise ratio (SNR) versus the peak input pressure of a subarray for varying VC control voltages. The lowest signal level is at an SNR of 0 dB in the highest gain setting. The highest signal level is at the point where the SNR diverges 1 dB from the dB-linear SNR-to-pressure curve at the lowest gain setting. In total, the measurable peak pressure range is between 0.99 Pa and 4559 Pa, which gives a 73 dB dynamic range (DR). The peak SNR is 52 dB and was measured at the highest gain setting. Distortion of the RX signals does not significantly affect the image quality, as received pulse amplitudes, widths and times-of-arrival define the reconstructed image. Therefore, SNR is used as a metric for DR instead of the signal-to-noise+distortion ratio (SNDR).

Given that the SNR is 0 dB for a peak input pressure of 0.99 Pa, the input pressure noise is calculated to be 0.452 $\mathrm{mPa_{rms}}/\sqrt{\mathrm{Hz}}$ in the 1.4 MHz to 3.8 MHz bandwidth of interest. The simulated conversion efficiency of the CMUTs is between 2.5 nA/Pa and 4.0 nA/Pa. When combining this conversion efficiency with the estimated measurement uncertainties of the acoustic measurement setup, the

input referred current noise density is estimated at 1.4 $pA_{rms}/\sqrt{Hz}$ with an uncertainty of ± 0.7 $pA_{rms}/\sqrt{Hz}$, which is in line with expectations. Figure 2.17(b) shows the output PSD used for deriving one data point in Figure 2.17(a). The signal tone is at 2.5 MHz. At high amplitudes, odd-harmonics that alias back into the bandwidth of interest dominate distortion.

2.5.4. Imaging Results

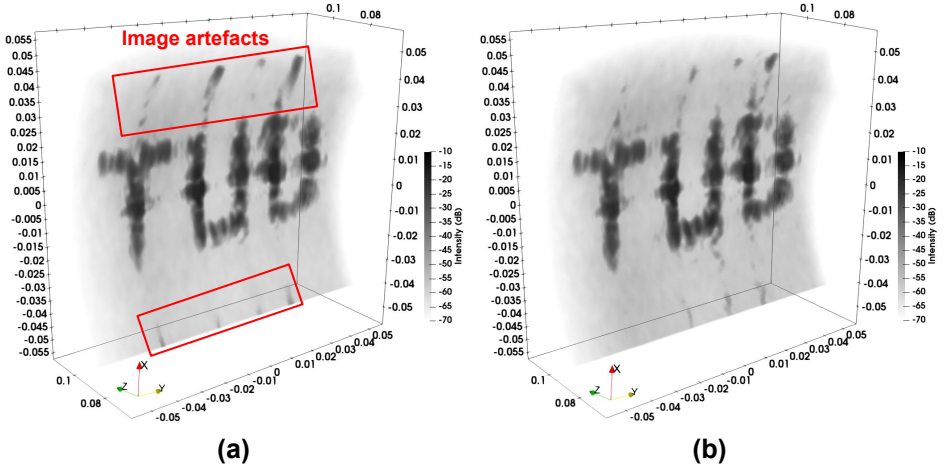

Figure 2.18: (a) 3D B-mode image of 3D-printed "TUD" logo without equalization. (b) 3D B-mode image of the same 3D-printed "TUD" logo with equalization.

To demonstrate imaging capabilities of the probe, images were made of a tissue mimicking phantom (CIRS 040GSE) [38] and multiple objects in a water tank. The 3D images shown in Figure 2.18 and 2.19 were made with 1 tile, using the same TX scheme as is shown in Figure 2.16 in the same water tank, using a 5 V TX amplitude. Figure 2.18 shows a 60°×60°×10 cm volume 3D B-mode image of 3D-printed "TUD" logo with and without channel equalization. As the images demonstrate, the artefacts in the image are reduced with decreased TDM-induced crosstalk.

Figure 2.19(a) shows a similarly obtained 3D B-mode image of a set of needle heads, connected to a shaker, which oscillated the needles along the Z-axis at 20 Hz. Given that the probe is imaging at 2000 volumes/s, it is oversampling the needle head positions by 50×, as is demonstrated in Figure 2.19(b) where the

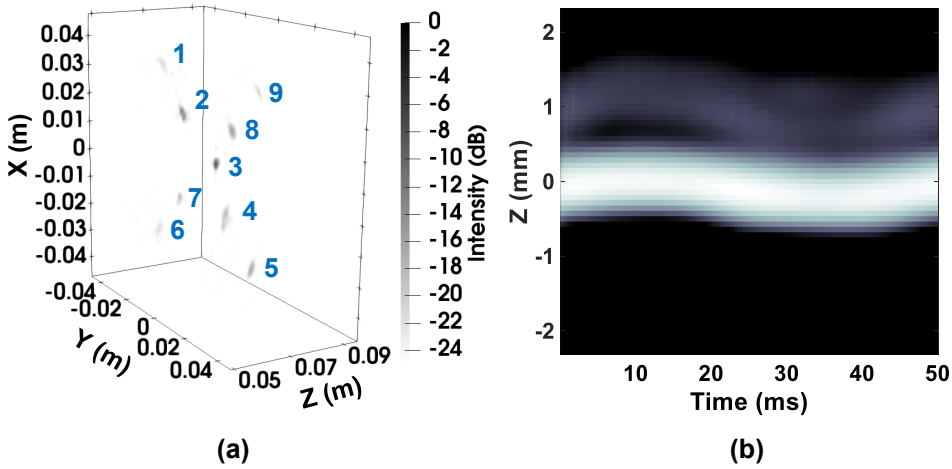

Figure 2.19: (a) 3D B-mode image of cross-shaped needle phantom. (b) M-Mode image of needle 3, which is moving along the Z-axis at a 20 Hz frequency.

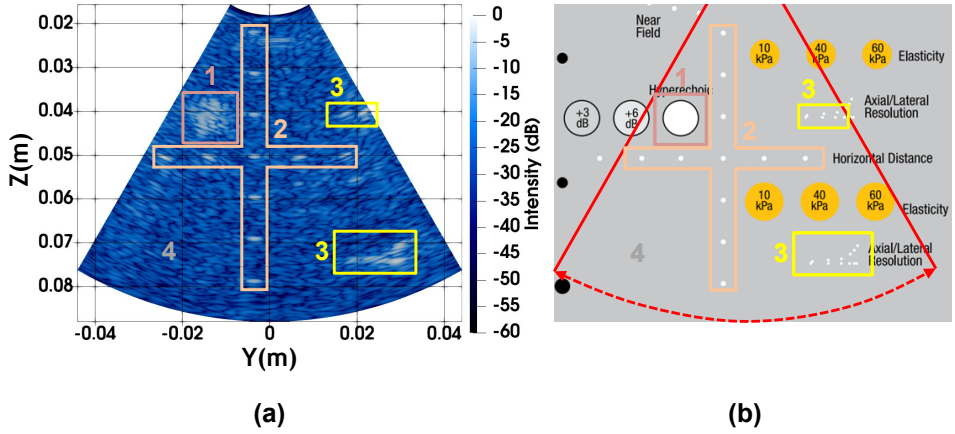

Figure 2.20: (a) B-mode image of tissue mimicking (CIRS 040GSE) phantom. Region 1 shows a hyperechoic cylinder, region 2 shows nylon strings, region 3 shows shows nylon strings with a smaller size and region 4 shows the background speckle of the phantom. (b) Reference image of the phantom [38].

position of center needle 3 is shown versus time.

Figure 2.20 shows a B-mode image of the tissue mimicking phantom, which attenuates ultrasound waves by 0.5 dB/cm/MHz. To reconstruct the image, 3 beams were used that are diverging along the Y-axis and plane waves along the out-of-plane X-axis, rather than the transmission scheme shown in Figure 2.16.

Just like that scheme, only the center square is used in TX for the same reason. The opening angle of the TX beams are also the same along the Y-axis. The image was recorded at 8000/3≈2.7 kHz at a 5 V TX. This lower TX voltage was chosen as a precaution to prevent damaging the limited number of imaging prototypes available. Despite this, the probe has enough round-trip DR to obtain a penetration depth of ≥8.8 cm with a sufficiently high contrast. This gives ample margin for features that have lower contrast when imaging with 40 V TX. Note, the imaging depth is limited by the depth that the VSX can process at an 8 kHz PRF, which is roughly 7 mm less than the theoretically achievable depth at a 1540 m/s speed of sound in human tissue.

Table 2.1: Performance summary and comparison with the prior art.

	This work	[7]	[20]	[3]	[4]	[6]
Technology	**180 nm BCD + MEMS**	180 nm BCD + MEMS	180 nm BCD	180 nm BCD	180 nm BCD	180 nm BCD
Transducer	**2D CMUT**	2D CMUT	2D PZT	2D PZT	CMUT	2D PZT
TX/RX Channels	**4096 / 4096**	8960 / 8960	128 / 3072	288 / 288	40 / 40	256 / 256
Center Frequency	**2.6 MHz**	5.5 MHz	2 MHz	6 MHz	5 MHz	9 MHz
Element Pitch	**365 µm**	208 µm	300 µm	160 µm	N/A	125 µm
Arbitrary-Wave TX	✓	✓	×	×	×	×
TX BF	✓	✓	✓	✓	✓	✓
Crosstalk Calibration	✓	×	×	×	×	×
Volume Rate [vol/s]	**2000**	N/A	N/A	1000	N/A	N/A
Channel Reduction	**8×**	64×	24×	18×	40×	128×
Channel Reduction Method(s)[*1]	**4× µBF** **2× TDM**	8× Summing / MUX 8× RX Pre-processing[*2]	24× µBF	3× µBF 6× D-TDM	5× µBF 8× TDM	8× MUX 4× µBF 4× D-TDM
RX Output Type	**Analog**	Digital	Analog	Digital	Analog	Digital
Max TX Voltage [V]	**65**[*3]	50	138	30	70	20
Active Area / El. [mm^2]	**0.12**[*4]	0.043	0.09	0.03	0.15	0.016
RX Power / El. [mW]	**0.85**[*5]	0.66[*6]	0.74	1.12	4.65	1.83
Peak SNR [dB]	**52**	54.5[*6]	N/A	52.2	N/A	54
Input DR [dB]	**73**	N/A	85	91	76	83

*1 : micro-beamformer (µBF), analog time-division multiplexing (TDM), multiplexing (MUX), digital time-division multiplexing (D-TDM)

*2 : A combination of signal-processing techniques to realize channel-count reduction.

*3 : Voltage can be generated by the ASICs, but the acoustic prototypes are limited to 40 V TX.

*4 : This excludes the 'Remainder' category from Figure 2.14.

*5 : Given a ramp function applied to VC over each T/R period. RX Power per Element consists of the power consumed by the VGAs, µBFs and cable drivers divided by the number of elements.

*6 : From the results presented in [39].

2.6. Conclusion

To address the emerging need for large-volume HVR imaging, this paper has presented a 4096-element 3D ultrasound probe. The probe is based on 365-µm-pitch CMUTs with a 2.6 MHz center-frequency, which are monolithically integrated on 2 tiled ASICs that were fabricated in a 180nm BCD process. For TX, these contain a novel arbitrary-PDM-wave TX BF, implemented as a programmable digital pipeline. It interfaces with element-level 2-level 65 V unipolar pulsers that drive the CMUT array. In RX, the ASICs pre-amplify signals with element-level low-noise VGAs with a 36-dB gain range and provide 8× channel-count reduction by applying 2×2 µBF and 2× TDM. Together, the proposed system architecture enables imaging a 60°×60°×10 cm volume at 2000 volumes/s, the highest volume rate for designs with in-probe channel-count reduction reported to date, while providing sufficient RX-channel reduction for the probe to interface with existing imaging systems. Moreover, PRBS-trained EQ reduces RX-channel crosstalk, which allows power efficient scaling of the in-probe cable drivers. A set of prototypes have been developed for both electrical and acoustic performance evaluation. With the acoustic prototypes, the targeted imaging performance was demonstrated with both water tank measurements and tissue-mimicking phantom images.

Table 2.1 shows a summary of the achieved results and a comparison with the prior art. While previous works have also reported combinations of micro-beamforming and signal modulation techniques to reduce channel count [3], [4], [6], this work demonstrates its scalability to imaging arrays with thousands of elements, while retaining a high volume rate. In addition, the system has a high flexibility in TX waveform definition at a reduced complexity compared to arbitrary-wave TX BFs in the prior art. Together with competitive power consumption and DR, it is a promising solution for use in medical R&D targeting improved diagnosis and treatment of abdominal aortic aneurysms, as well as other applications requiring HVR imaging of a large volume.

References

[1] P. Santos, G. U. Haugen, L. Løvstakken, E. Samset, and J. D'hooge, "Diverging wave volumetric imaging using subaperture beamforming," *IEEE Transactions on Ultrasonics, Ferroelectrics, and Frequency Control*, vol. 63, no. 12, pp. 2114–2124, 2016. DOI: 10.1109/TUFFC.2016.2616172.

[2] B. Savord and R. Solomon, "Fully sampled matrix transducer for real time 3D ultrasonic imaging," in *IEEE Symposium on Ultrasonics, 2003*, vol. 1, 2003, 945–953 Vol.1. DOI: 10.1109/ULTSYM.2003.1293556.

[3] Y. M. Hopf et al., "A pitch-matched high-frame-rate ultrasound imaging ASIC for catheter-based 3-D probes," *IEEE Journal of Solid-State Circuits*, vol. 59, no. 2, pp. 476–491, 2024. DOI: 10.1109/JSSC.2023.3299749.

[4] A. Rezvanitabar et al., "Integrated hybrid sub-aperture beamforming and time-division multiplexing for massive readout in ultrasound imaging," *IEEE Transactions on Biomedical Circuits and Systems*, vol. 16, no. 5, pp. 972–980, 2022. DOI: 10.1109/TBCAS.2022.3205024.

[5] C. Chen et al., "A pitch-matched front-end ASIC with integrated subarray beamforming ADC for miniature 3-D ultrasound probes," *IEEE Journal of Solid-State Circuits*, vol. 53, no. 11, pp. 3050–3064, 2018. DOI: 10.1109/JSSC.2018.2864295.

[6] P. Guo et al., "A 125 μ m-pitch-matched transceiver ASIC with micro-beamforming ADC and multi-level signaling for 3-D transfontanelle ultrasonography," *IEEE Journal of Solid-State Circuits*, pp. 1–14, 2024. DOI: 10.1109/JSSC.2024.3355854.

[7] J. M. Rothberg et al., "Ultrasound-on-chip platform for medical imaging, analysis, and collective intelligence," *Proceedings of the National Academy of Sciences*, vol. 118, no. 27, e2019339118, 2021.

[8] R. Wodnicki et al., "Row-multiplexed 1,024 element large aperture array for electronic scanning in elevation," in *2022 IEEE International Ultrasonics Symposium (IUS)*, 2022, pp. 1–4. DOI: 10.1109/IUS54386.2022.9958124.

[9] T. Kim et al., "Design of an ultrasound transceiver ASIC with a switching-artifact reduction technique for 3D carotid artery imaging," *Sensors*, vol. 21, no. 1, 2021, ISSN: 1424-8220. [Online]. Available at: https://www.mdpi.com/1424-8220/21/1/150.

[10] S. I. Nikolov, J. Kortbek, and J. A. Jensen, "Practical applications of synthetic aperture imaging," in *2010 IEEE International Ultrasonics Symposium*, 2010, pp. 350–358. DOI: 10.1109/ULTSYM.2010.5935627.

[11] J. A. Jensen, "Estimation of high velocities in synthetic-aperture imaging—part i: Theory," *IEEE Transactions on Ultrasonics, Ferroelectrics, and Frequency Control*, vol. 66, no. 6, pp. 1024–1031, 2019. DOI: 10.1109/TUFFC.2019.2906384.

[12] P. Wagner, C. Daft, S. Panda, and I. Ladabaum, "5G-1 two approaches to electronically scanned 3D imaging using cMUTs," in *2006 IEEE Ultrasonics Symposium*, 2006, pp. 685–688. DOI: 10.1109/ULTSYM.2006.185.

[13] T. M. Carpenter, M. W. Rashid, M. Ghovanloo, D. M. J. Cowell, S. Freear, and F. L. Degertekin, "Direct digital demultiplexing of analog TDM signals for cable reduction in ultrasound imaging catheters," *IEEE Transactions on Ultrasonics, Ferroelectrics, and Frequency Control*, vol. 63, no. 8, pp. 1078–1085, 2016. DOI: 10.1109/TUFFC.2016.2557622.

[14] Q. Liu, C. Chen, Z.-y. Chang, C. Prins, and M. A. P. Pertijs, "A mixed-signal multiplexing system for cable-count reduction in ultrasound probes," in *2015 IEEE International Ultrasonics Symposium (IUS)*, 2015, pp. 1–4. DOI: 10.1109/ULTSYM.2015.0141.

[15] M. W. Rashid, C. Tekes, M. Ghovanloo, and F. L. Degertekin, "Design of frequency-division multiplexing front-end receiver electronics for CMUT-on-CMOS based intracardiac echocardiography," in *2014 IEEE International Ultrasonics Symposium*, 2014, pp. 1540–1543. DOI: 10.1109/ULTSYM.2014.0381.

[16] Verasonics, *Vantage specifications for biomedical & general applications*, English, Verasonics, 2024, 4 pp., February, 2024.

[17] E. Boni et al., "ULA-OP 256: A 256-channel open scanner for development and real-time implementation of new ultrasound methods," *IEEE Transactions on Ultrasonics, Ferroelectrics, and Frequency Control*, vol. 63, no. 10, pp. 1488–1495, 2016. DOI: 10.1109/TUFFC.2016.2566920.

[18] Y. M. Hopf et al., "A pitch-matched transceiver ASIC with shared hybrid beamforming ADC for high-frame-rate 3-D intracardiac echocardiography," *IEEE Journal of Solid-State Circuits*, vol. 57, no. 11, pp. 3228–3242, 2022. DOI: 10.1109/JSSC.2022.3201758.

[19] P. Guo et al., "A 1.2-mW/channel pitch-matched transceiver ASIC employing a boxcar-integration-based rx micro-beamformer for high-resolution 3-D ultrasound imaging," *IEEE Journal of Solid-State Circuits*, vol. 58, no. 9, pp. 2607–2618, 2023. DOI: 10.1109/JSSC.2023.3271270.

[20] Y. Igarashi et al., "Single-chip 3072-element-channel transceiver/128-subarray-channel 2-D array IC with analog RX and all-digital tx beamformer for echocardiography," *IEEE Journal of Solid-State Circuits*, vol. 54, no. 9, pp. 2555–2567, 2019. DOI: 10.1109/JSSC.2019.2921697.

[21] A. Ramalli, A. Dallai, E. Boni, F. Guidi, S. Ricci, and P. Tortoli, "Real-time pulse compression in multigate spectral doppler imaging," in *2015 IEEE International Ultrasonics Symposium (IUS)*, 2015, pp. 1–4. DOI: 10.1109/ULTSYM.2015.0418.

[22] P. Song, M. W. Urban, A. Manduca, J. F. Greenleaf, and S. Chen, "Coded excitation plane wave imaging for shear wave motion detection," *IEEE Transactions on Ultrasonics, Ferroelectrics, and Frequency Control*, vol. 62, no. 7, pp. 1356–1372, 2015. DOI: 10.1109/TUFFC.2015.007062.

[23] L. C. Jansen, S. Fekkes, H.-M. Schwab, and R. G. Lopata, "Increasing abdominal aortic aneurysm curvature visibility using 3D dual probe bistatic ultrasound imaging combined with probe translation," *Ultrasonics*, vol. 139, p. 107 284, 2024, ISSN: 0041-624X. DOI: https://doi.org/10.1016/j.ultras.2024.107284. [Online]. Available at: https://www.sciencedirect.com/science/article/pii/S0041624X24000465.

[24] K. Riemer, M. Toulemonde, E. M. Rowland, C. H. Leow, M.-X. Tang, and P. D. Weinberg, "4D blood flow and wall shear stress measured using volumetric ultrasound image velocimetry," in *2020 IEEE International Ultrasonics Symposium (IUS)*, 2020, pp. 1–4. DOI: 10.1109/IUS46767.2020.9251636.

[25] J. Voorneveld et al., "4-D echo-particle image velocimetry in a left ventricular phantom," *Ultrasound in Medicine & Biology*, vol. 46, no. 3, pp. 805–817, 2020, ISSN: 0301-5629. DOI: https://doi.org/10.1016/j.ultrasmedbio.2019.11.020. [Online]. Available at: https://www.sciencedirect.com/science/article/pii/S0301562919316217.

[26] M. S. Kilinc, H. Lee, C. D. Arvanitis, and F. L. Degertekin, "Dual mode CMUT array operation for skull imaging and passive acoustic monitoring in

transcranial ultrasound," in *2021 IEEE International Ultrasonics Symposium (IUS)*, 2021, pp. 1–4. DOI: 10.1109/IUS52206.2021.9593365.

[27] R. Van Schaijk and M. Devices, "CMUT: a versatile and low cost ultrasonic platform," in *Micromachined Ultrasonic Transducers 2019*, Philips Innovation Serv., 2019. Accessed: Mar. 2, 2025. [Online]. Available at: https://www.salland.com/wp-content/uploads/2019/06/11-Rob-van-Schaijk-Philips-InS-MEMS-Seminar-2019.pdf.

[28] Y. M. Hopf et al., "A compact integrated high-voltage pulser insensitive to supply transients for 3-D miniature ultrasound probes," *IEEE Solid-State Circuits Letters*, vol. 5, pp. 166–169, 2022. DOI: 10.1109/LSSC.2022.3180071.

[29] M. Tan et al., "A 64-channel transmit beamformer with ±30-V bipolar high-voltage pulsers for catheter-based ultrasound probes," *IEEE Journal of Solid-State Circuits*, vol. 55, no. 7, pp. 1796–1806, 2020. DOI: 10.1109/JSSC.2020.2987719.

[30] H. Zhang et al., "A high-linearity and low-emi multilevel class-D amplifier," *IEEE Journal of Solid-State Circuits*, vol. 56, no. 4, pp. 1176–1185, 2021. DOI: 10.1109/JSSC.2020.3043815.

[31] P. Guo et al., "A pitch-matched low-noise analog front-end with accurate continuous time-gain compensation for high-density ultrasound transducer arrays," *IEEE Journal of Solid-State Circuits*, vol. 58, no. 6, pp. 1693–1705, 2023. DOI: 10.1109/JSSC.2022.3200160.

[32] E. Kang et al., "A reconfigurable ultrasound transceiver ASIC with 24 × 40 elements for 3-D carotid artery imaging," *IEEE Journal of Solid-State Circuits*, vol. 53, no. 7, pp. 2065–2075, 2018. DOI: 10.1109/JSSC.2018.2820156.

[33] MathWorks. "Adaptive equalizers," Accessed: Mar. 2, 2025. [Online]. Available at: https://nl.mathworks.com/help/comm/ug/adaptive-equalizers.html.

[34] Samtec. "HQCD," Accessed: Mar. 2, 2025. [Online]. Available at: https://www.samtec.com/products/hqcd.

[35] Terasic. "DE10-Nano kit," Accessed: Mar. 2, 2025. [Online]. Available at: https://www.terasic.com.tw/cgi-bin/page/archive.pl?Language=English&CategoryNo=167&No=1046&PartNo=2#heading.

[36] T. Instruments, "OPAx354-Q1 250-MHz, rail-to-rail I/O, CMOS operation amplifiers," 2018. Accessed: Mar. 2, 2025. [Online]. Available at: https://www.ti.com/lit/ds/symlink/opa4354-q1.pdf?HQS=TI-null-null-alldatasheets-df-pf-SEP-wwe&ts=1730713860935.

[37] J. A. Jensen. "Field-II simulation program," Accessed: Mar. 2, 2025. [Online]. Available at: https://field-ii.dk/.

[38] CIRS Inc. "Multi-purpose, multi-tissue ultrasound phantom model 040GSE," Accessed: Mar. 2, 2025. [Online]. Available at: https://www.cirsinc.com/wp-content/uploads/2021/09/040GSE-DS-093021.pdf.

[39] N. Sanchez et al., "34.1 an 8960-element ultrasound-on-chip for point-of-care ultrasound," in *2021 IEEE International Solid-State Circuits Conference (ISSCC)*, vol. 64, 2021, pp. 480–482. DOI: 10.1109/ISSCC42613.2021.9365808.

3

Design and Characterization of CMUT-on-ASIC and PZT-on-ASIC Prototypes

This chapter is planned for publication in IEEE Transactions on Ultrasonics, Ferroelectrics, and Frequency Control

3.1. Introduction

Chapter 2 has presented an ultrasound probe design with a Philips (now Xiver) CM5 capacitive micromachined ultrasound transducer (CMUT) [1] array monolithically integrated on 2 application-specific integrated circuits (ASICs), one of the first successful active probes with a large transducer array integrated this way. In addition, the ASIC was designed to be compatible with bulk lead zirconate titanate (PZT) transducers. This provides the unique benefit of a high-end ultrasound imaging system serving as a test platform for multiple different transducer technologies. As a result, a consistent comparison between transducer technologies is more easily done. Moreover, broadened compatibility offers reduced project risks, as a specific transducer technology can prove too difficult to integrate without the overall probe development being negatively affected. However,

the increased flexibility comes at the cost of increased design complexity of both the ASIC itself, and the integration into the full probe casing.

Two types of transducers were initially considered: the CM5 device and a PZT transducer that was designed within the Ultra-X-Treme consortium, both introducing different design challenges. As mentioned in Chapter 2, the CM5 transducer requires a 120 V bias, which is not natively compatible with the TSMC 180-nm bipolar-CMOS-DMOS (BCD) fabrication process that is used for the ASIC. Moreover, while not a fundamental issue, damaged elements can destructively discharge, (partially) damaging the underlying ASIC. To mitigate the risk of rendering a prototype completely unusable, the ASIC is electrically partitioned in sections with different bias sources. However, this adds significant packaging complexity. Moreover, the desired transducer pad layout for PZT is centered to the transducer, unlike with CMUTs, where the pads are at the corners of the transducers, further increasing design complexity. The two different transducers also have a significantly different performance characteristics. Mainly the impedance difference of both devices have design implications for both the transmit (TX) and receive (RX) circuits.

This chapter gives an overview of the trade-offs in circuit design and system integration, and presents the results from characterization of both aforementioned devices. The structure of this chapter is as follows. In Section 3.2, the layout and design trade-offs in the ASIC are presented, as well as the packaging of both the CMUT and PZT arrays. The measurement setup for evaluation of both devices is also shown. In Section 3.3, the results from the device characterizations are presented. Sections 3.4 and 3.5 present a discussion and conclusions, respectively.

3.2. Methods

3.2.1. Overview of Integrated Transducer Technologies

Figure 3.1(a) shows a (simplified) layer stack of the CMUT transducer on the ASIC. It consists of a vibrating membrane with a conducting layer on top of a conducting plate, acting as two electrodes, separated by a cavity and a thin dielectric. The membrane is actuated by a time-varying electrostatic force between the electrodes. To increase the sensitivity of the transducer, a large direct-current (DC) bias voltage V_{bias} is applied to the top membrane. To produce acoustic waveforms, an alternating current (AC) voltage is applied to the bottom plate.[1],

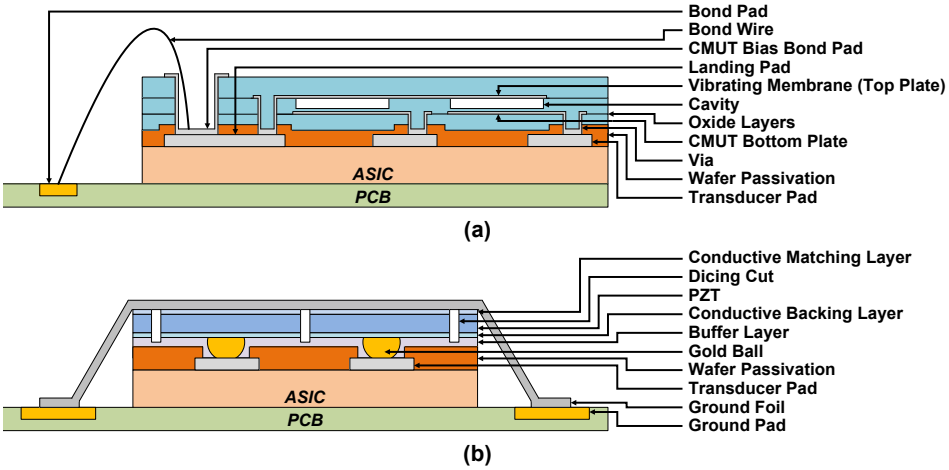

Figure 3.1: (a) Simplified layer stack of CM5 CMUT. (b) Layer stack of TU Delft 'In house' PZT.

[2] As mentioned in Section 2.4.1, the CM5 device operates in 'collapse mode' [1], [2]. This requires the voltage across the CMUT to remain above 80 V [1]. The nominal V_{bias} of the CM5 device is 120 V, leaving 40 V of headroom for the pulser in the ASIC to drive the device.

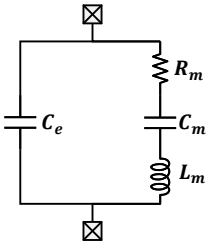

(a)

	C_e	C_m	L_m	R_m
CM5 (V_{bias} = 120 V)	3.6 pF	1.7 pF	2245 µH	53 kΩ
Bulk PZT	3.5 pF	3.3 pF	921 µH	5.6 kΩ

(b)

Figure 3.2: (a) BVD model for ultrasound transducer. (b) BVD model parameters for CM5 and bulk PZT transducers.

Figure 3.1(b) shows a layer stack of the PZT transducer on the ASIC. The PZT interfaces via a conductive backing layer to a bottom electrode, and via a conductive matching layer to a top electrode. The device uses the piezoelectric properties of PZT to produce acoustic waveforms when actuated, where the geometries of the PZT dictate its electrical and acoustic characteristics [3], [4]. Figure

3.2 shows the Butterworth-Van Dyke (BVD) model [5] of both transducers. The small-signal model parameters of the CMUT are with the device linearized around V_{bias}. C_e is the electrical parasitic capacitance of the transducer. C_m, L_m and R_m represent the electro-mechanical resonance behavior of both devices. While C_e for both devices is similar, the main impedance difference at resonance stems from R_m.

3.2.2. Fabrication of Transducer Arrays

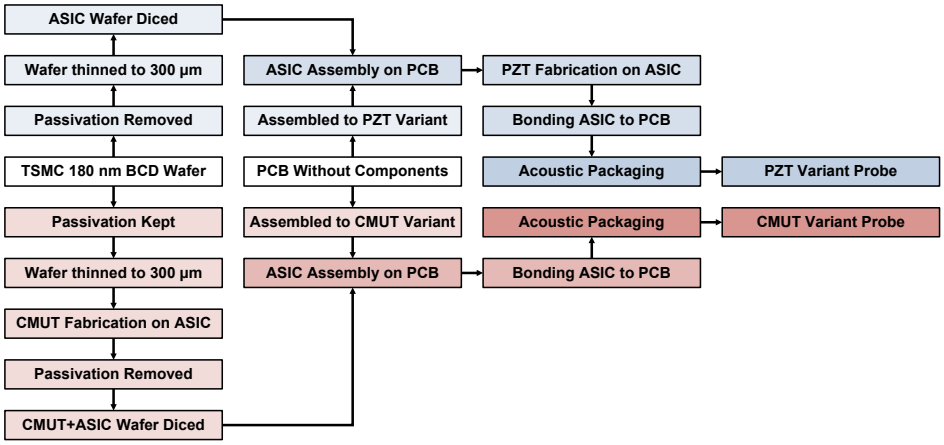

Figure 3.3: Basic fabrication flow for both probe variants.

Figure 3.3 shows the fabrication flow for both probe variants. Both the ASIC and printed circuit board (PCB) in the probe are designed to be reconfigurable for both fabrication flows, each having their own design trade-offs. To fabricate both variants of the probe, both the ASIC and PCB undergo a processing split. For the device wafers containing the ASIC, the passivation layer is processed differently. The PCB on which the ASICs and acoustic array are manufactured are assembled with different components. Section 3.2.3 covers the ASIC design trade-offs and Section 3.2.4 covers the packaging and PCB design trade-offs.

CM5 Transducer Design

The micro-fabrication of the CM5 transducer array on the ASIC device wafers is similar as described in [6], which covers the same device. First the TSMC device

wafers are thinned and flattened. After which, holes are etched in the passivation to the transducer pads on the ASIC. An aluminum alloy is then deposited and patterned, which acts as the CMUT bottom electrode and forms an electric contact to the transducer pads. A dielectric (SiO_2) layer is then deposited. After which, a sacrificial metal layer is deposited and patterned, which acts as a sacrificial layer to form the vacuum cavity shown in Figure 3.1(a). Next, another dielectric layer is deposited, on which the top electrode is deposited and patterned. A part of the membrane (SiO_3N_4) layer is then deposited and holes are etched at the edge of the CMUTs, through which the sacrificial material is removed. Finally, another membrane layer is deposited, finishing the CMUTs. Contacts to the bond pads of the ASICs are etched and patterned, finishing the ASIC+CMUT tiles.

PZT Transducer Design

The fabrication of the probe variant with the custom PZT array is similar to the processing steps in [7], [8], [9], [10]. First, ASIC(s) are mounted on the same PCB as with the CMUT variant. After which, gold balls are placed on the transducer pads and the acoustic surface area is filled with a buffer epoxy layer. This buffer epoxy is then ground down, to expose flat electric contacts. The acoustic region is then coated with a conductive glue, after which the PZT and matching layer are deposited. This acoustic stack is diced with a 50 µm dicing blade to form the 315×315 μm^2 PZT transducers. The ASIC(s) are then bonded to the PCB and coated with an insulator. Finally, a ground foil is applied over the PZT array and electrically insulated with a protective acoustically transparent layer [11].

3.2.3. ASIC Compatibility with Different Transducers

Circuit Design Considerations

Figure 3.4(a) shows a simplified diagram of the circuits interfacing with each transducer, which are covered in detail in Section 2.3. These consist of a 2-level class-D driver and a transmit/receive (T/R) switch for TX, and a variable gain amplifier (VGA) which consists of a trans-impedance amplifier (TIA) cascaded by a current amplifier (CA) for RX. HVGND is the ground of the driver, TGND is the transducer ground, and TGND' is an on-chip routed sense line of the off-chip TGND, which acts as reference for the VGA.

The driver and T/R switch consist of transistors M_{P1}, M_{N1}, M_{N2}, and M_{N3}.

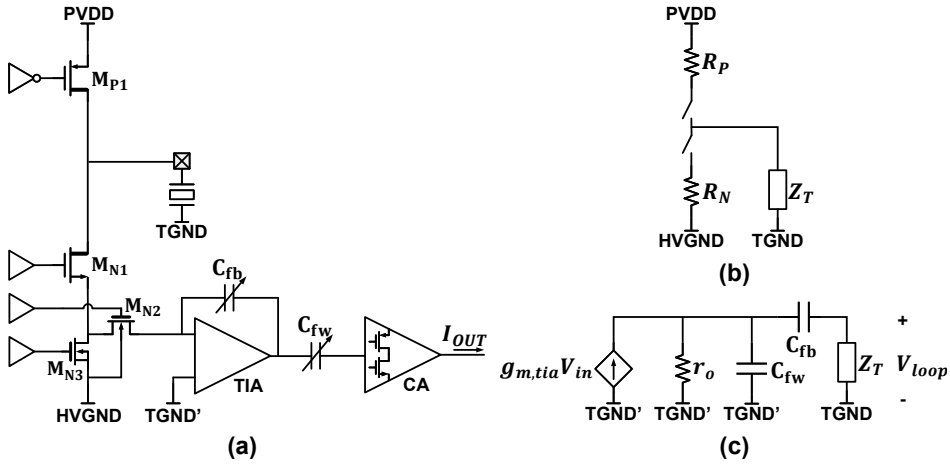

Figure 3.4: (a) Simplified diagram of the TX and RX circuits interfacing with a transducer. (b) Simplified circuit diagrams of the pulser in TX. (c) Simplified loop gain circuit diagram of the TIA.

Most of the time they operate in the triode region, or are off. As such, to maximize power transfer in TX, they are all scaled such that the transducer impedance Z_T dominates. Given that the resistive part of the transducer impedance is dominant within the bandwidth of interest, for scaling of the transistors, the pulser can be modeled as shown in Figure 3.4(b), where R_N is the series on-resistance of M_{N1} and M_{N3}, and R_P is that of M_{P1}.

Given that Z_T of the PZT transducer is much lower than that of the CMUT transducers (Figure 3.2), the scaling of R_P and R_N are based on that lower impedance, resulting in the necessary over-scaling for the CMUT transducers. Similarly, as the VGA takes a current input, the series on-resistance of M_{N1} and M_{N2} is scaled for noise assuming the Z_T of the PZT transducer. As is covered later in this section, the trace impedance of the power supplies is finite and carefully scaled. Therefore, to relax their requirements, the drivers of M_{P1} and M_{N1} are scaled as a trade-off between minimizing the supply current changes per pulse transition (dI/dt) and power efficiency.

Figure 3.4(c) shows the simplified loop-gain circuit model of the TIA, where the loop gain is V_{loop}/V_{in}, r_o is the output impedance of the TIA, C_{fb} its feedback capacitor, and C_{fw} its feedforward capacitor. As the TIA is the first stage in the RX circuit, its trans-conductance $g_{m,tia}$ is ideally scaled for noise. As described in Section 2.3.3, the VGA implements a time-gain compensation (TGC) range of 36 dB, where the thermal noise of its stages ideally scale with this TGC range to

maximize power efficiency. However, given the low Z_T of the PZT transducers, at low TGC gain settings, $g_{m,tia}$ is scaled to retain a sufficiently high loop gain within the bandwidth of interest. Therefore, the TIAs are overscaled for the CMUT transducers in a part of the TGC gain range.

Pad Placement

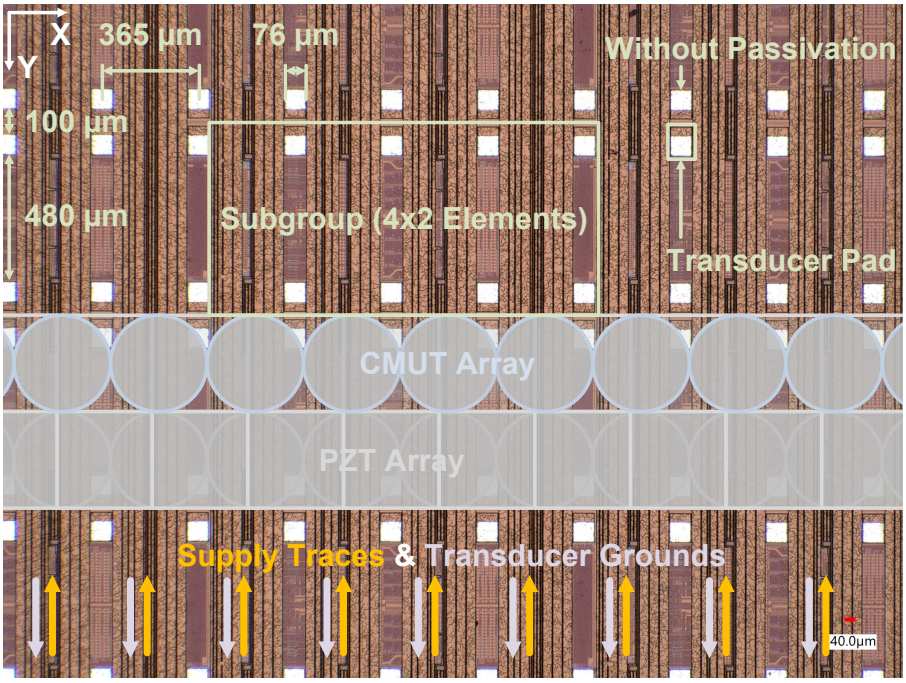

Figure 3.5: Section of the ASIC without transducers, with indications of the positions of the different transducer arrays.

As shown in Figure 3.1, the CMUT interfaces with the ASIC through a micro-machined via next to the device bottom electrode, whereas the PZT does so through a gold ball contact. As a result, the desired location of the transducer pad, relative to the center of the transducer is offset. To accommodate both devices, the pad layout on the ASIC is as shown in Figure 3.5. While the pads are equidistant along the X-axis, they are shifted outwards per subgroup along the Y-axis. This provides a landing zone compatible with both the CMUT vias and the PZT bottom electrodes.

As aforementioned, for fabrication of the ASIC, two variants of the mask that

defines the openings in the passivation layer were produced. The CMUT variant has none of the passivation layer removed, while the PZT variant has passivation removed around the wire bond pads and a 76×73 µm^2 section from the transducer pads. This leaves at least 100 µm spacing (Figure 3.5) between exposed sections for a 50 µm dicing blade to pass through (covered in Section 3.2.2). To ensure alignment for the dicing blade, marking structures were placed at the ASIC periphery.

Trace Routing

As the transducer ground is the return path for a large part of the currents drawn during TX, the ASIC supply lines are routed directly under the transducers, following this return current (Figure 3.5), to minimize their loop inductance. For RX, a transducer ground sense line is used as a reference for the VGAs (Section 2.3.3), routed in the same way as the supply lines. A supply ring in the periphery around the transducer array connects the LV supplies going into the transducer array to the periphery LV circuits and bond pads.

3.2.4. Packaging for CMUT Arrays

Figure 3.6(a) shows the packaging also shown in Section 2.4.2, with added layer thicknesses (along Z). The co-integrated ASICs + CMUTs are tiled on a steel plate that is mounted on a PCB. The steel plate serves as a flat mounting surface and a thermal conductor. After bonding the ASICs to the PCB, an injection molded TPX-MX002 window is mounted on top of the array and makes acoustic contact via a silicone viscous glue. An O-ring, pressurized via a custom anodized aluminum casing and backside clamp, ensures that the entire front side of the probe is watertight. The backside clamp also serves as a heatsink, and makes thermal contact to the steel plating via a thermal paste and an array of thermal vias in the PCB.

As covered in Chapter 2, the CM5 transducer is biased at a voltage V_{bias} of +120 V to reliably operate in collapse mode. To accommodate this, the CMUT top electrodes are routed to the ASIC periphery to be bonded to the PCB that provides V_{bias}. Figure 3.6(b) shows the applied biasing scheme. To easily disconnect faulty CMUT columns, the decoupling capacitor C_B that AC grounds the CMUT bias lines (Figure 2.8) is split into a capacitor C_{B1} that is shared by two bias lines, and

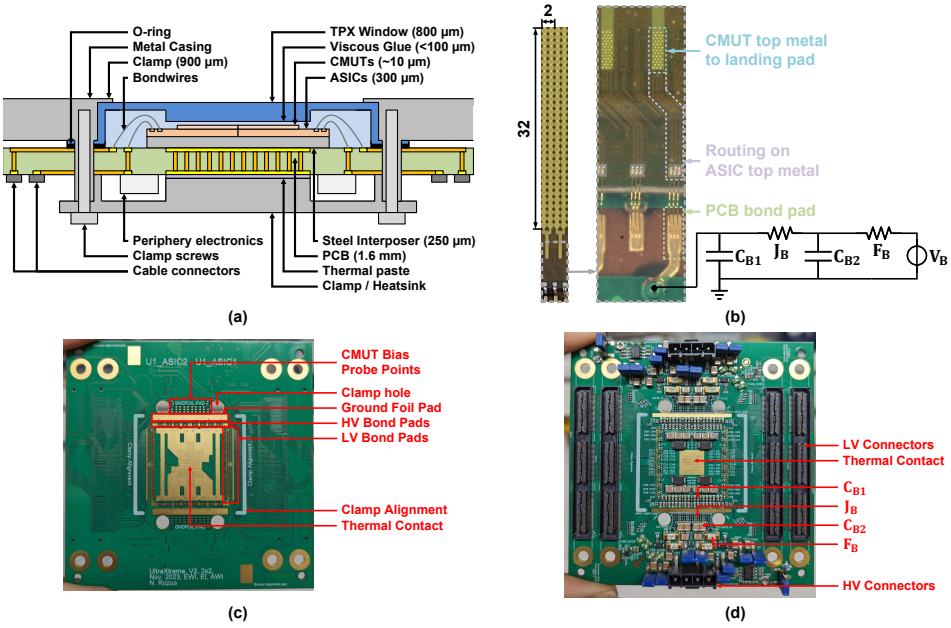

Figure 3.6: (a) Overview of the CMUT variant probe packaging. (b) Overview of the CMUT biasing per two columns of the imaging array. (c) Front of PCB in probe. (d) Back of PCB in probe.

a global second-level decoupling capacitor C_{B2}. These are separated by an array of jumpers J_B, which can be removed to disconnect 2 columns from the array, thus avoiding faulty CMUTs (further) damaging the underlying ASIC.

Figure 3.6(c) shows the front-side of the PCB. Each CMUT bias bond pad is also separately connected to an array of probe points, which can be used to power 2 columns at a probe station. This is intended for future validation of arrays, and/or to test potential apodization techniques. However, they are currently unused. The ground foil pads serve a dual purpose of acting as alignment markers for the metal casing, and serving as the ground for the PZT transducers, which are covered in more detail later in this section. Figure 3.6(d) shows the backside of the PCB. To limit the damage to the ASIC when a CMUT discharges and/or shorts, high-speed fuse F_B connects the dc bias supply V_B to the CMUTs. The resistance of F_B is low enough such that the supply network time constants are much lower than a T/R cycle to ensure that the bias voltage remains constant over continuous use.

3

3.2.5. Packaging for PZT Arrays

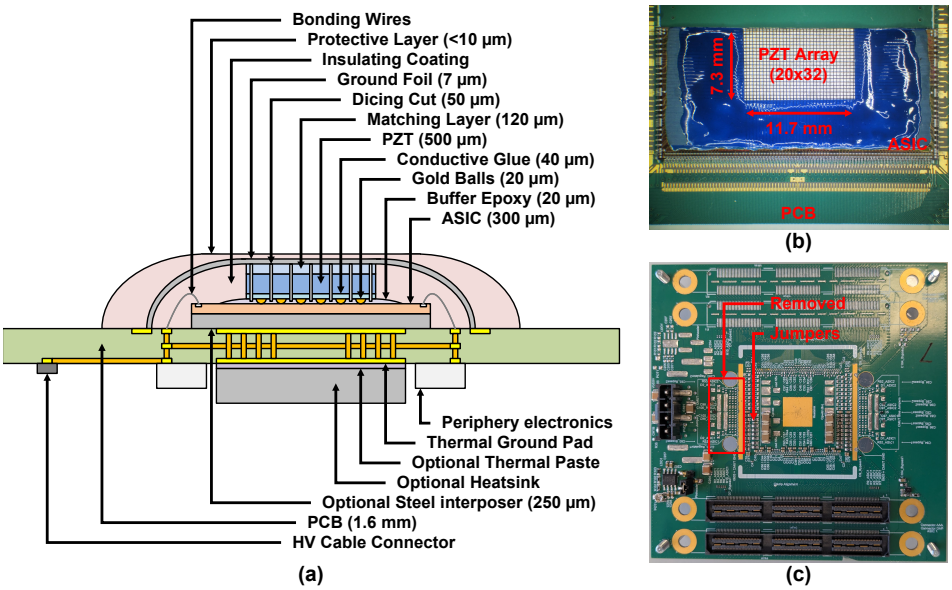

Figure 3.7: (a) Overview of the PZT variant probe packaging and layer stack. (b) PZT array without ground foil and top coating. (c) Back of PCB in probe.

Figure 3.7(a) shows an overview of the packaged PZT probe with layer dimensions. While the front side of the probe is watertight, it requires mounting in a casing to safely interface with water, which is covered in more detail in Section 3.2.7. Figure 3.7(b) shows the front side of the PCB without ground foil and protective coating. While for a fully working array, a steel interposer is present between the ASICs and the PCB, it is omitted in the measured sample, as only one ASIC is mounted on the PCB. Therefore, the added thermal coupling and tile flattening it provides is not needed. Moreover, the fabricated array is also smaller than what one ASIC can accommodate. This resulted from yield issues, likely originating from damage to the specific diced ASICs that were used and mechanical damage from the dicing process during the array manufacturing. However, these are not fundamental issues, which is covered in more detail in Section 3.4.

Figure 3.7(c) shows the backside of the PCB, and changes made versus the CMUT variant. As the CMUT landing pads on the ASIC do not need to be biased, capacitors C_{B1} (Figure 3.6) are replaced by an array of jumpers. Moreover, C_{B2}, F_B and J_B are omitted. A heatsink is also not mounted on the backside of

the PCB for the same relaxed thermal sinking requirements for this prototype as aforementioned.

3.2.6. Measurement Setup for Validating Transducer Process Spread

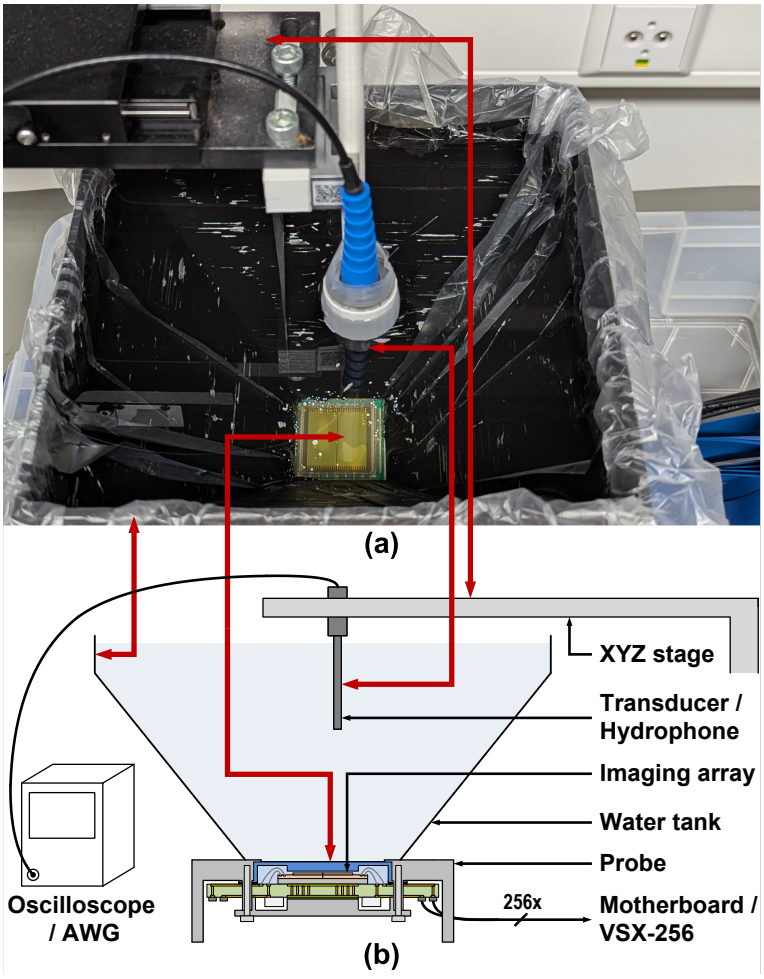

Figure 3.8: (a) Picture of the measurement setup for measuring the RX spread. (b) Diagram of the measurement setup for measuring the RX and TX spread. For the RX measurements, a transducer is connected to an AWG. For the TX measurements, a hydrophone is connected to an oscilloscope.

Figure 3.8 shows the measurement setup for validating the spread over the transducer array. A 3-D-printed water tank is placed on a probe with standoffs to level it relative to an XYZ stage. For measuring the TX sensitivity of the array, a pre-calibrated 200 µm hydrophone [12], connected to an oscilloscope, is placed 1.0 cm from the imaging array, and centered to a CMUT element in a 32×32-element grid. To ensure that the XY movement of the stage tracks the XY coordinates of the array, the hydrophone is aligned to a subset of elements in advance.

While scanning the 32×32-element element grid, each element produces a 50-period pulse at a 10 V amplitude, with the hydrophone centered to that transmitting element. To compensate for small misalignments between the center of the transducer and the hydrophone, the estimated distance and the known pre-calibrated distance along the Z-axis are used to estimate the angle of the misalignment. The gain error from the hydrophone directivity function $D_H(\theta)$ is adjusted using the following equation [13]:

$$D(\theta) = \frac{\sin[kr\sin(\theta)]}{kr\sin(\theta)} \tag{3.1}$$

$D(\theta)$ is the directivity of a cylindrical piston, $k = 2\pi f/c$, f is the frequency of the sound wave, c is the speed of sound, and r is the radius of the piston. To adjust for the gain error from the directivity of the CMUT, its directivity measurements are used as a reference, which are covered later this chapter.

For measuring the RX sensitivity of the array, a pre-calibrated 2 mm diameter transducer [14], connected to an arbitrary waveform generator (AWG), is placed 10.4 cm from the imaging array. A similar alignment method is used as with TX. However, the transducer is moved to the center of a 4×4-element sub-array instead. At the center of each sub-section, the transducer produces 8 2.5 MHz 30-period pulses as the ASIC multiplexes between the 8 input channels of each subgroup.

3.2.7. Measurement Setup for Validating Transducer Directivity

Figure 3.9 shows the measurement setup for validating the RX directivity. The prototype probes are placed in a waterproof casing [7] that can be rotated along a center axis of the probe's array (θ). The casing contains a 25 µm thick polyamide acoustic window, to which the probes are interfaced via an acoustic gel. The casing has mounting/alignment screws for the PCB used in each prototype probe. How-

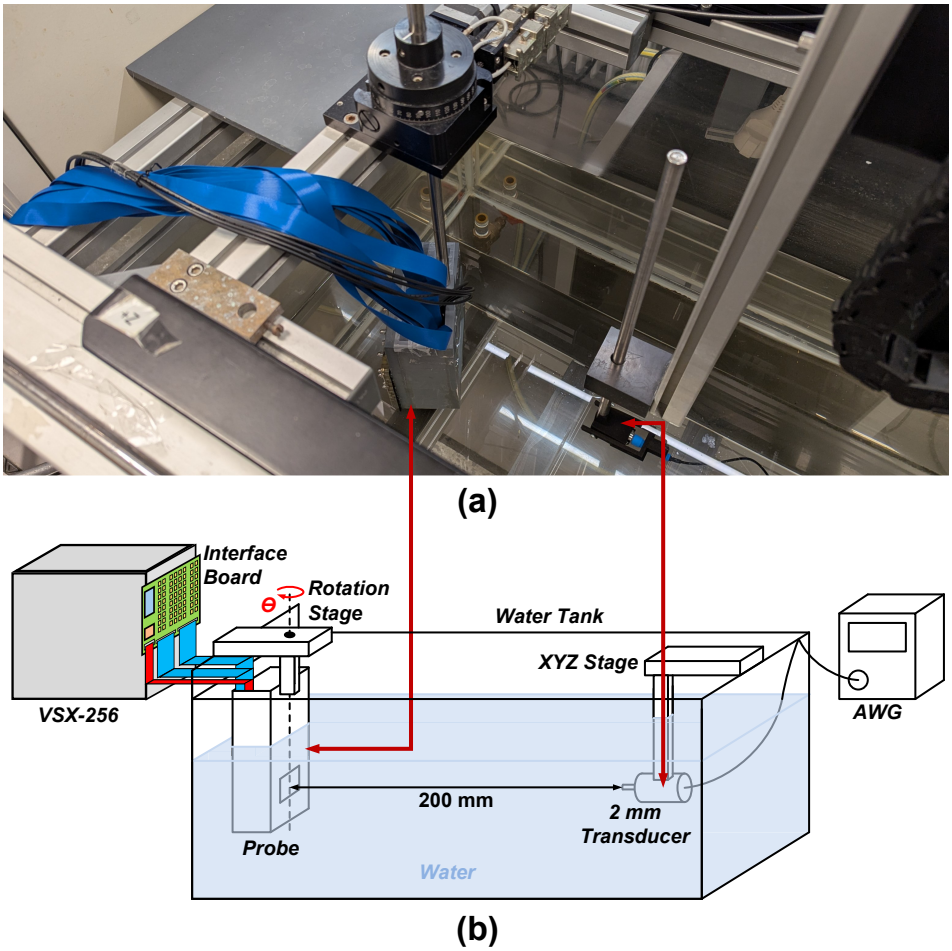

Figure 3.9: (a) Picture of the measurement setup for measuring transducer RX directivity. (b) Diagram of the measurement setup.

ever, it is incompatible with the aluminium casing of the CMUT variant. Therefore, a sample is used without this casing, but with the same polymethylpentene (TPX) window. An XYZ stage positions a pre-calibrated 2 mm diameter circular single element transducer [14] to the center of a transducer in the probe's array at a 20 cm distance.

Figure 3.10 shows the measurement setup for validating the TX directivity. The probe is placed in the surface of the water tank, with a pre-calibrated 200 µm diameter hydrophone [12] facing it from the bottom. This hydrophone is

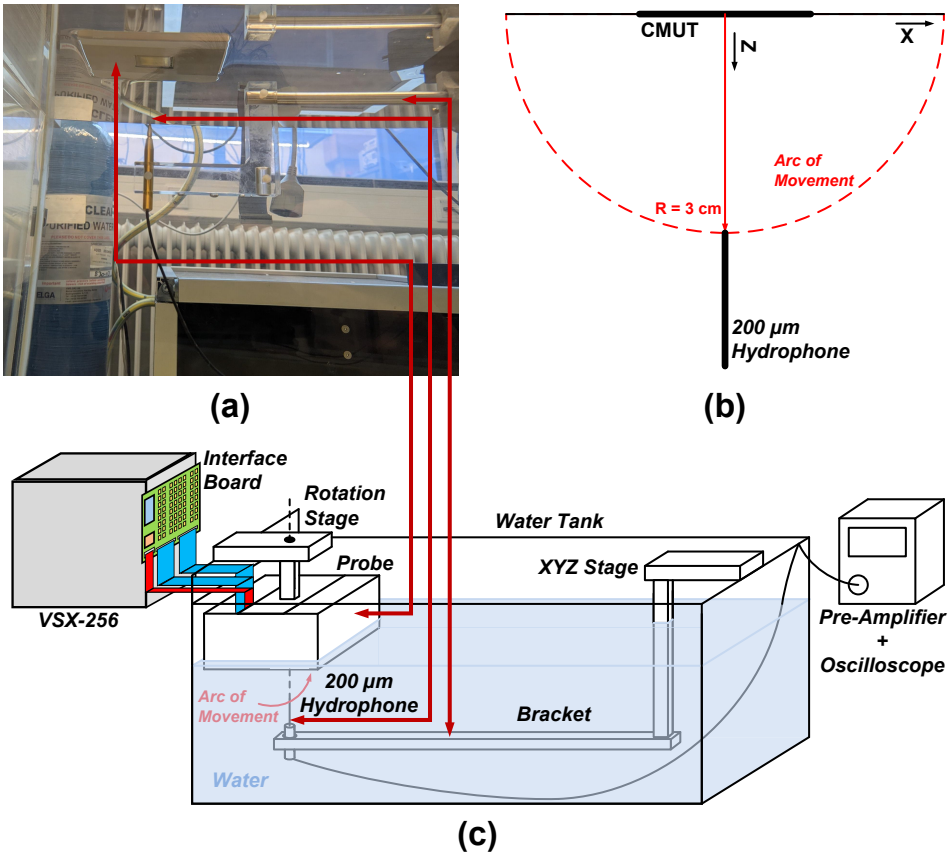

Figure 3.10: (a) Picture of the measurement setup for measuring CMUT TX directivity. (b) Diagram of the movement of the hydrophone around a CMUT transducer. (c) Diagram of the measurement setup.

connected to the XYZ stage via a bracket, allowing it to make an arcing motion around the transducers. The radius of the arc is 3 cm as a trade-off between minimizing measurement tolerances and the SNR of the measured data. The hydrophone connects to a two-stage pre-amplifier. The first stage [15] connects to the hydrophone in the water tank, the second stage [16] is added for increased signal gain outside of the water tank. To adjust for misalignments between the plane of the imaging array and the hydrophone, it is triangulated using three corner elements of the array. Equation 3.1 is used to compensate for the directivity of the hydrophone. The ASIC pulsers drive the CMUTs at a 5 V peak-peak amplitude.

Two types of excitation are used for characterizing the directivity of the trans-

ducers: a 2-period pulse and a 2.6 MHz continuous-wave function. While the pulsed waveform is more representative of the waveform used when imaging, the continuous waveform shows the effects of measurement asymmetries and crosstalk better, due to any resulting constructive/destructive interference being represented in the magnitude of the waveform, which is only partially the case for the pulsed waveforms.

3.3. Results

3.3.1. Prototypes Under Test

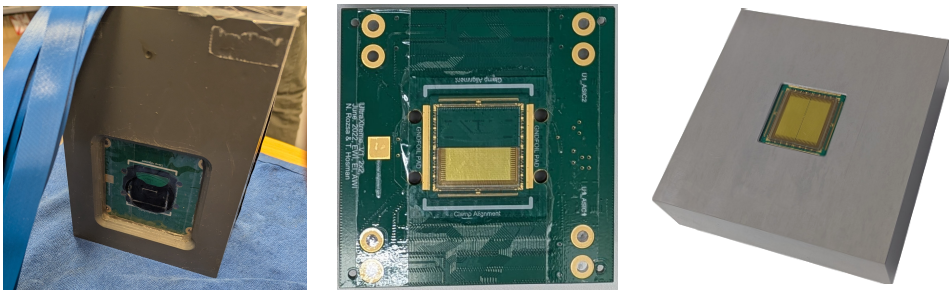

Figure 3.11: (a) Picture of the measured PZT probe prototype in waterproof casing. (b) Picture of the CMUT probe prototype used for measuring RX directivity. (c) Picture of a CMUT probe prototype with aluminium casing as used for all other measurements.

Figure 3.11 shows pictures of the prototypes used for the measurement results presented in this section. Figure 3.11(a) shows the measured PZT probe prototype in the waterproof casing shown in Figure 3.9. Due to the aforementioned yield issues, no fully working PZT probe prototype has been produced. For the prototype shown, a short between the TX power line (PVDD) and a ground line (Section 2.3.2) prevents the sample from working in TX. Therefore, the sample can only be operated in RX mode. Figure 3.11(b) shows the CMUT probe prototype used for measuring RX directivity. As aforementioned, this sample does not have the aluminum casing shown in Figure 3.6(a) to be mountable in the waterproof casing shown in Figure 3.11(a). Figure 3.11(c) shows a CMUT probe prototype with the aluminium casing, used for all measurements except RX directivity.

3.3.2. CMUT Sensitivity Spread

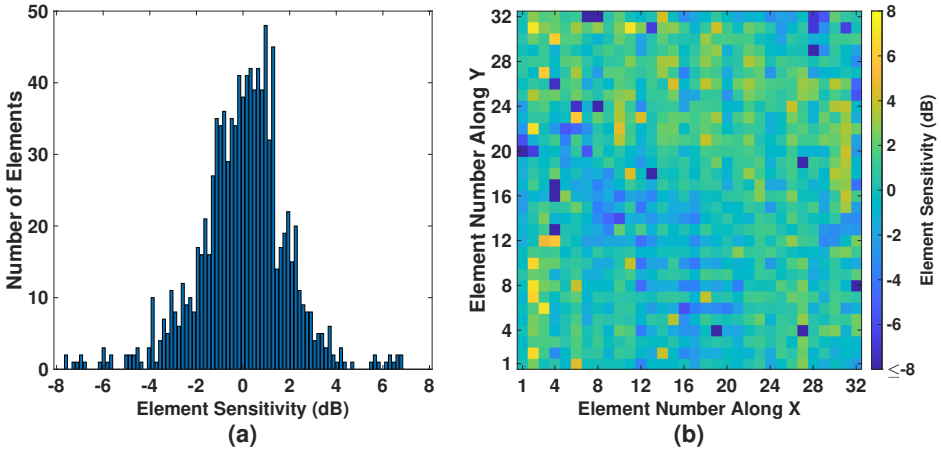

Figure 3.12: (a) Histogram of the normalized TX sensitivity of 1013 elements. (b) Spatial map of the normalized TX sensitivity of 1024 elements.

Figure 3.12 shows the distribution of the TX sensitivity of 1024 elements. The TX pressures shown are derived from a fast Fourier transform (FFT) of 40 periods of the 2.6 MHz 50-period square wave transmitted, only taking into account the first harmonic. The measured sample mean pressure magnitude is 1.15 kPa. Using the exact diffraction derivation of a circular piston [17], the estimated CMUT surface pressure is 60.8 kPa, which results in a TX efficiency of approximately 12.2 kPa/V. Elements are considered working if their recorded pressure is no less than -8 dB from this mean. The element yield is 98.9%, and the 1013 working elements have sample standard deviation of 1.9 dB.

Figure 3.13 shows the distribution of the RX sensitivity of 1024 elements for varied gain settings of the VGAs in the ASIC. Their gain is controlled by a control voltage (VC), which is varied between 0 V and 1.2 V, as covered in Section 2.3.3. The RX pressures shown are derived from an FFT of 20 periods of the 2.5 MHz 30-period sine wave transmitted, only taking into account the first harmonic. It should be noted that this is a distribution from a different sample than for the TX sensitivity measurement, as that sample broke before the RX sensitivity could be measured, which is covered in more detail in Section 3.4.

The measured sample mean RX sensitivity is 1.4 nA/Pa, or ∼23.2 µV/Pa through the Thévenin equivalent using the simulated impedance of the CMUTs at

resonance (see Figure 3.2). This was determined at the highest gain, as the ASIC electronics influence the measurement result the least in this setting. Elements with a recorded pressure above -8 dB from the sample mean at the highest gain setting are considered working. Of the 1024 elements, 1019 meet this condition, resulting in an element yield of 99.5 %, which is in line with the TX sensitivity measurements. Figure 3.14 shows the change in sample standard deviation versus the VGA gain setting. At the highest and lowest gain settings, the sample standard deviation of the working elements is 2.0 dB, which is in line with the TX sensitivity measurements. Between these gain settings, a small gradient in the sensitivity is observed, increasing the sample standard deviation up to 3.2 dB. The expected reason for this gradient is covered in Section 3.4.

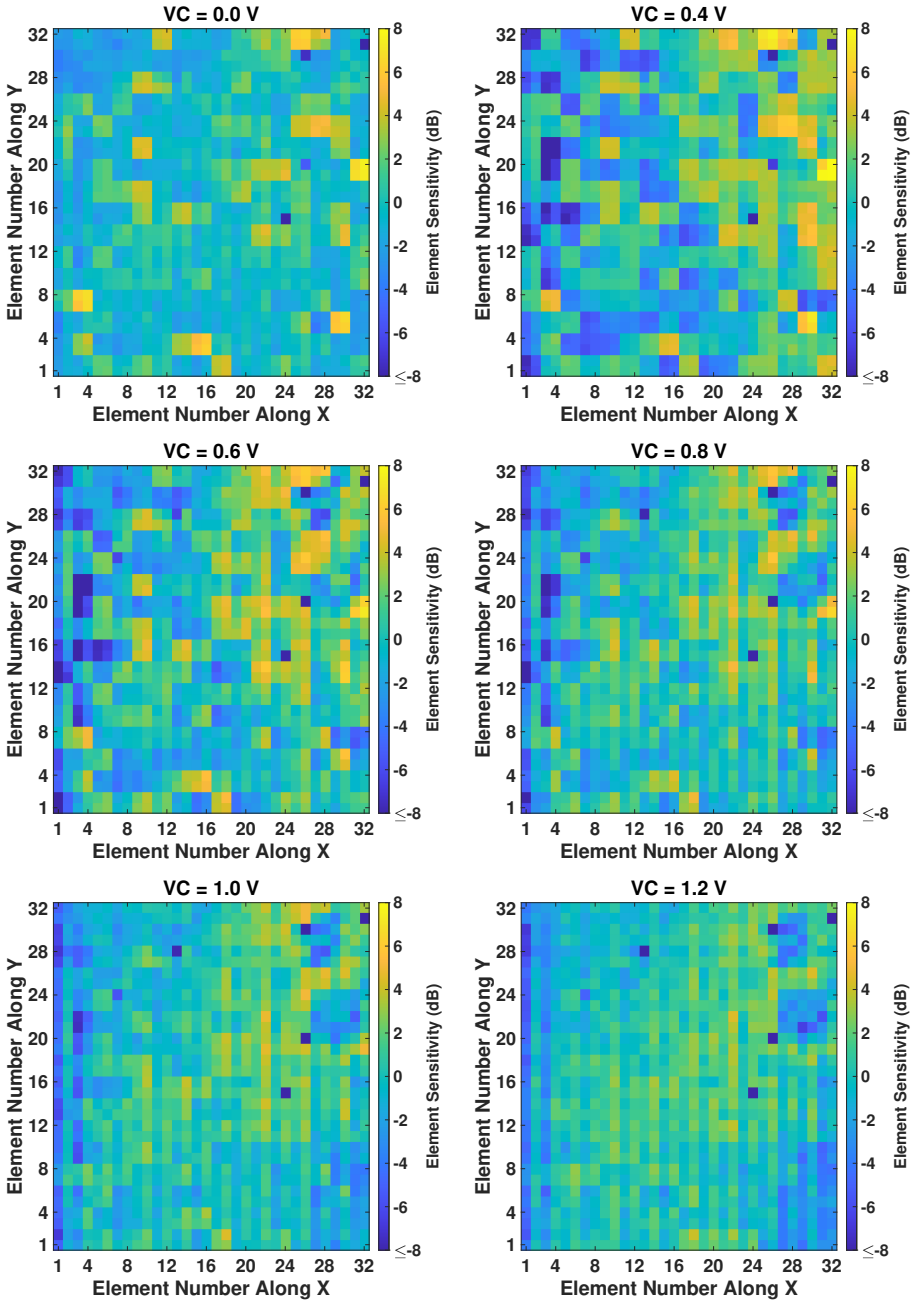

Figure 3.13: Spatial map of the normalized RX sensitivity of 1024 elements for VC varied between 0 V and 1.2 V.

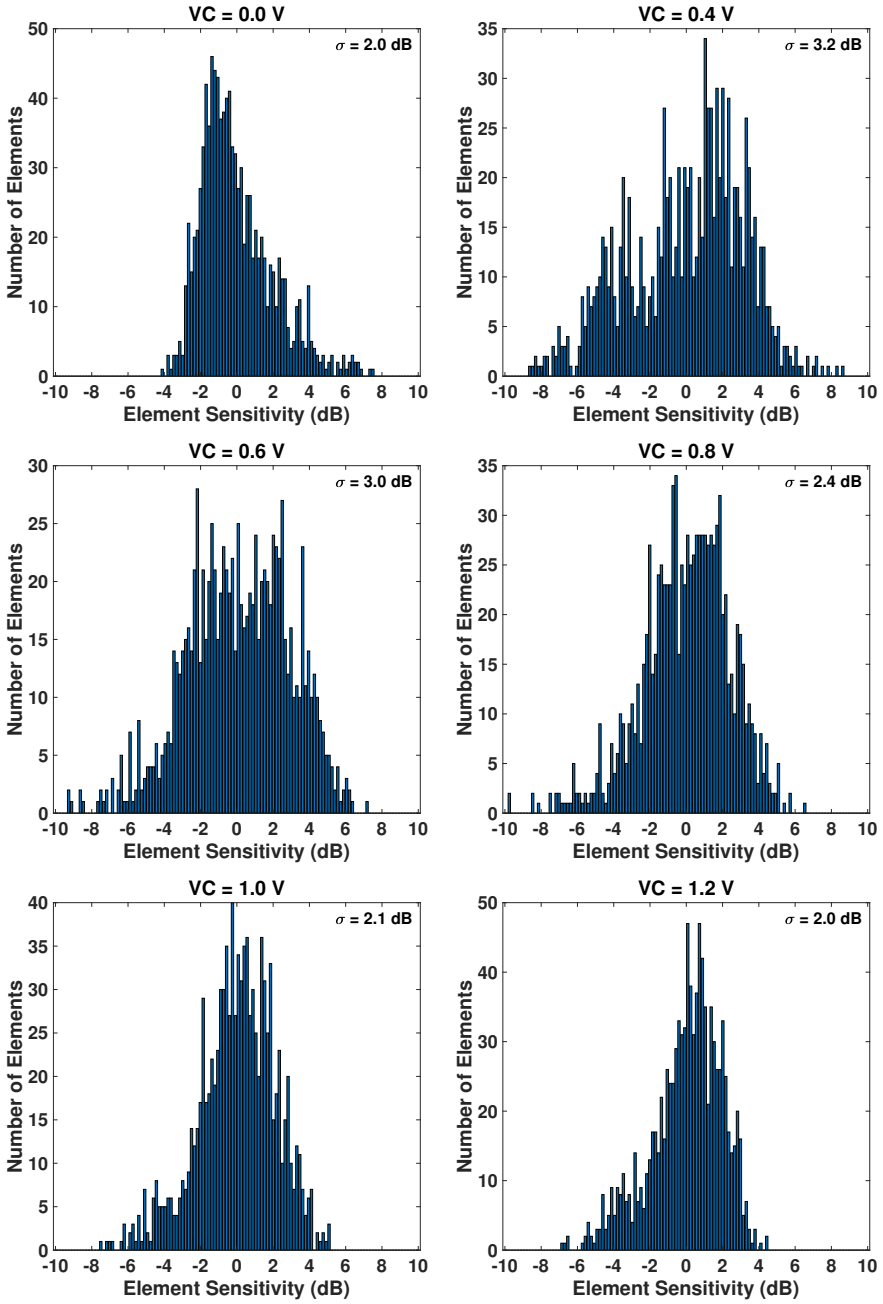

Figure 3.14: Histogram of the normalized RX sensitivity of 1019 elements for VC varied between 0 V and 1.2 V.

3.3.3. Transducer Directivity

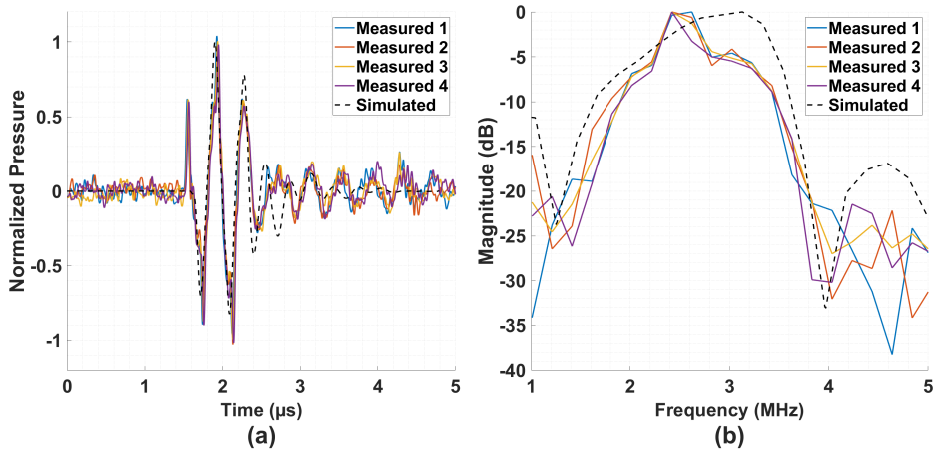

Figure 3.15: Transmitted 2-period pulse by the CMUT probe: (a) time domain waveform; (b) spectrum.

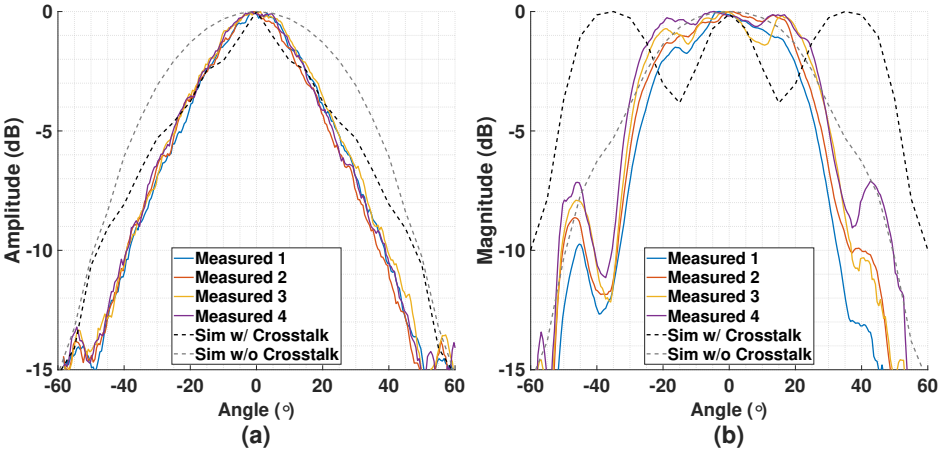

Figure 3.16: TX directivity pattern of 4 typical elements of the CMUT probe: (a) based on the peak-peak amplitude of a transmitted 2-period pulse; (b) based on the magnitude of a transmitted 2.6 MHz continuous wave.

Figure 3.15 shows the recorded TX waveform of a 2-period pulse produced by the CMUT probe and its spectrum after adjusting for the frequency response of the hydrophone. Due to a peak around the center-frequency, the -6-dB bandwidth reduces to 39% compared to the 58% from simulation. Figure 3.16 shows

the normalized TX directivity pattern of 4 typical elements in the CMUT probe compared to simulation when transmitting the 2-period pulse and when transmitting a 2.6 MHz continuous wave. The average -6-dB beam widths are 54° and 60°, for the 2-period pulse and continuous waveform, respectively. When taking into account crosstalk, the measurements align well with simulations up to ±25° when transmitting a 2-period pulse, but diverge from simulations when transmitting a continuous wave. However, although the amplitudes are different, similar side-lobes are observed.

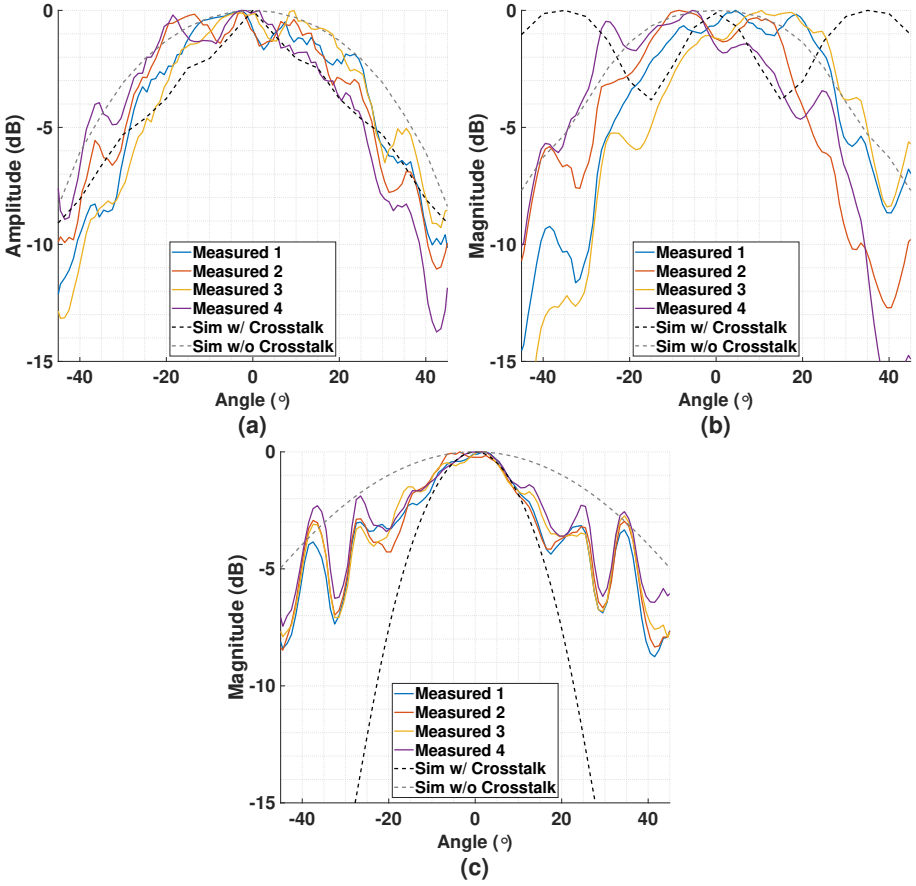

Figure 3.17: (a) CMUT probe RX directivity pattern of 4 typical elements based on the peak-peak amplitude of a transmitted 2-period pulse. (b) CMUT probe RX directivity pattern of 4 typical elements based on the magnitude of a transmitted 2.6 MHz continuous wave. (c) PZT probe RX directivity pattern of 4 typical elements based on the magnitude of a transmitted 2.6 MHz continuous wave.

Figure 3.17 shows the normalized RX directivity pattern of 4 elements of both probe variants. The average -6-dB beam widths of the CMUT variant are 61° and 60°, for the 2-period pulse and continuous waveform, respectively. The simulation results shown are the same as in Figure 3.15, assuming reciprocity. Like with TX, measurement results align well with simulations when transmitting a 2-period pulse, but diverge when transmitting a continuous wave. The observed asymmetries between beam profiles are likely a result of crosstalk, which is covered in Section 3.4.

The average -6-dB width of the PZT variant is 58.4°, which is between the simulated beam widths, with and without crosstalk. The notches observed around ±30° are consistent with the observations in [7], [8], making the acoustic window of the waterproof casing and the presence of more elements in the measured array than modeled the likely causes of the measurements diverging from the simulations, as is also covered in more detail in Section 3.4.

The RX sensitivity was also determined based on the peak magnitude of 40 measured elements, which is 2.5 nA/Pa and 1.1 nA/Pa for the PZT and CMUT variant, respectively. Through the Thévenin equivalent with their respective impedances at resonance (see Figure 3.2), the RX sensitivities translate to 13.3 µV/Pa and 17.9 µV/Pa. These results for the CMUT sample are consistent with results presented in Section 3.3.2. However, the RX sensitivity of the PZT variant is about 3× higher than simulations predict.

3.4. Discussion

3.4.1. Comparison Between Measurements

In Section 3.3.1 it was mentioned that the RX and TX sensitivity distribution were measured using different samples as a result of the first breaking. This was as a result of using a TX voltage above 10 V after CMUTs destructively discharged beforehand. It is likely, that either a destructive discharge, where a CMUT breaks, or a non-destructive discharge, where a faulty CMUT injects charge in the pulser as it is biased, damages the pulser to which the CMUT is connected. As a result, it still functions at lower voltages, but displays latch-up-like conditions when operating at voltages above 5-20 V. These yield issues are the reason why samples are currently operating at a TX voltage of 5 V as a precaution. However, a combination of ASIC+CMUT screening and improved device processing is likely to

completely remove these issues in future samples.

As aforementioned, different CMUT samples were also used between directivity and sensitivity measurements, due to compatibility issues with the rotation stage of the water tank. To improve consistency, in future measurements, a full waterproof encapsulation of the aluminum casing is intended to be fabricated. This allows, with some added mounting points, for the CMUT samples to become compatible, thus addressing this discrepancy. Alternatively, a smaller transducer could be used than the currently used 2-mm-diameter device, lowering compensation errors of the device directivity, enabling sufficiently low measurement errors when measuring directivity for RX the same way as done for TX.

Because of time restrictions and yield issues with the PZT sample fabrication, its characterization was limited to RX for a relatively low number of elements. The most likely cause of these yield issues is damage to the ASICs during the wafer dicing process. This issue is not fundamental, and is expected to be resolved in the near future. After which, new samples can be produced with the described method and re-measured in the same way as done for the CMUT samples.

3.4.2. Comparison with Simulation Results

For the CMUT variant, both the TX sensitivity and the RX sensitivity are lower by a factor of 2-3 versus simulations. However, this is only the case for measurements that use the 200-µm-diameter hydrophone as a reference. For measuring the TX sensitivity, it was the recording instrument. For the RX measurements, it was used to calibrate the 2-mm-diameter transducer. While not reported in this Chapter, the TX sensitivity was also measured using a 1-mm-diameter hydrophone [18], with a similar setup as shown in Figure 3.9. In these measurements, the CMUT RX sensitivity is in line with simulations. It is therefore assumed that the sensitivity of the hydrophone is not correctly calibrated. However, this does not explain the gap between the measured and simulated RX sensitivity of the PZT transducers, for which there currently is no clear explanation other than a high acoustic crosstalk.

As aforementioned, the CMUT directivity is in line with simulations when transmitting a 2-period pulse. However, this is when taking into account the acoustic window and crosstalk between adjacent elements. A single CMUT drum has a directivity similar to what Equation 3.1 would predict, which is significantly broader than what was measured. Moreover, the axis-symmetric model used for simulations does not take into account the dampening that occurs in the TPX

and silicone glue layers (see Section 3.2.4) and also does not accurately take into account the symmetries of the rectangular CMUT grid. Therefore, the effects of crosstalk are only modeled qualitatively. This also explains why the measurement results do not align well with simulations when transmitting a continuous wave, where mismatches in crosstalk magnitudes are more exacerbated.

The inconsistency observed in the PZT element RX directivity in Figure 3.17(c) is expected to be due to the added window of the waterproof casing (Figure 3.9), which was not modeled. Moreover, the simulations taking into account crosstalk from adjacent elements only model a 3×3 (sub)array, which does not take into account the crosstalk from the full array. As noted in [7], [8], a combination of acoustic crosstalk and the addition of the window cause dips in the directivity pattern, which also explains the dips observed in Figure 3.17(c).

3.4.3. VC-Dependent RX Sensitivity Gradient

In Figure 3.13, a gradient was observed in the measured RX sensitivity as the VGAs are in the middle of their gain range. As aforementioned, the gain of the VGAs is derived from a control voltage VC, which is compared to a globally routed supply reference. However, the VGA supply has a limited effect on this reference. Therefore, due to the voltage drops across the global VGA supply network, a small gain gradient is caused, which scales with VC. As the VGA gain saturates, this gradient disappears, as also observed.

While this gradient could be removed from the measurements by disabling sections of the array, reducing the supply voltage gradients, this would not be representative for nominal operation. Moreover, the spread of the CMUT array itself can still be assessed based on the lowest and highest VGA gain settings. Additionally, the increased channel spread is still considered acceptable for the imaging application of the probe. Also, given that this gradient is systematic, the probe's RX channels can be calibrated based on the presented measurement results if a decreased device spread is required across the VGA gain range.

3.5. Conclusion

Table 3.1: Overview of measurement results.

	TX Sensitivity μ [kPa/V] / σ [dB]	RX Sensitivity μ [nA/Pa] / σ [dB]	RX Sensitivity μ [μV/Pa]	TX/RX Beam Width Pulse [°] / Continuous Wave [°]	TX Pulse BW [%]
CM5	12.2 / 1.9	1.4 / 2.0	23.3	TX : 54 / 60 RX : 61 / 60	39
Bulk PZT	N.A.	2.5 / N.A.	13.3	RX : 56 / 58	N.A.

In this chapter, the fabrication and design trade-offs of an imaging system that is compatible with multiple transducer technologies have been presented. This reduces project risk and presents an improved method for characterizing and comparing transducer array technologies. The prototype probe consists of 2 ultrasound ASICs, integrated on a PCB, accommodating a transducer array of up to 64×64 elements. The ASICs are compatible with monolithic integration of CMUT devices and bulk PZT devices. This is achieved by a combination of careful layout of the transducer pad array, subgroups and supply routing, and routing in the periphery of CMUT HV bias lines. The PCB is made configurable, such that only modest component changes are required for compatibility with the different devices.

Characterization results of both devices were presented, of which an overview is shown in Table 3.1. In terms of device performance, the PZT array has a higher RX current sensitivity, whereas the CMUT array has a broader RX directivity. Moreover, co-integration of a large CMUT array on an ASIC has a higher yield than of a large bulk PZT array. While for different reasons yield of both characterized probe variants can still be improved, both variants are (partially) functional. Together with a high flexibility in TX waveform definition and element addressing, the system is a promising solution for standardization of future transducer technology validation and imaging array development.

References

[1] R. Van Schaijk and M. Devices, "CMUT: a versatile and low cost ultrasonic platform," in *Micromachined Ultrasonic Transducers 2019*, Philips Innovation Serv., 2019. Accessed: Mar. 2, 2025. [Online]. Available at: https://www.salland.com/wp-content/uploads/2019/06/11-Rob-van-Schaijk-Philips-InS-MEMS-Seminar-2019.pdf.

[2] K. Brenner, A. S. Ergun, K. Firouzi, M. F. Rasmussen, Q. Stedman, and B. Khuri–Yakub, "Advances in capacitive micromachined ultrasonic transducers," *Micromachines*, vol. 10, no. 2, p. 152, 2019.

[3] N. de Jong, N. Bom, J. Souquet, and G. Faber, "Vibration modes, matching layers and grating lobes," *Ultrasonics*, vol. 23, no. 4, pp. 176–182, 1985, ISSN: 0041-624X. DOI: https://doi.org/10.1016/0041-624X(85)90027-7. [Online]. Available at: https://www.sciencedirect.com/science/article/pii/0041624X85900277.

[4] D. S. dos Santos et al., "Experimental investigation of the effect of subdicing on an ultrasound matrix transducer," in *2021 IEEE International Ultrasonics Symposium (IUS)*, 2021, pp. 1–3. DOI: 10.1109/IUS52206.2021.9593315.

[5] K. Van Dyke, "The piezo-electric resonator and its equivalent network," *Proceedings of the Institute of Radio Engineers*, vol. 16, no. 6, pp. 742–764, 1928. DOI: 10.1109/JRPROC.1928.221466.

[6] R. van Schaijk, M. in 't Zandt, P. Robaeys, M. Slotboom, J. Klootwijk, and P. Bekkers, "Reliability of collapse mode cmut," in *2023 IEEE International Ultrasonics Symposium (IUS)*, 2023, pp. 1–4. DOI: 10.1109/IUS51837.2023.10307882.

[7] D. S. dos Santos et al., "An ultrasound matrix transducer for high-frame-rate 3-D intra-cardiac echocardiography," *Ultrasound in Medicine & Biology*, vol. 50, no. 2, pp. 285–294, 2024, ISSN: 0301-5629. DOI: https://doi.org/10.1016/j.ultrasmedbio.2023.11.001. [Online]. Available at: https://www.sciencedirect.com/science/article/pii/S0301562923003459.

[8] E. Kang et al., "A reconfigurable ultrasound transceiver ASIC with 24 × 40 elements for 3-D carotid artery imaging," *IEEE Journal of Solid-State Circuits*, vol. 53, no. 7, pp. 2065–2075, 2018. DOI: 10.1109/JSSC.2018.2820156.

[9] V. Daeichin et al., "Acoustic characterization of a miniature matrix transducer for pediatric 3d transesophageal echocardiography," *Ultrasound in Medicine & Biology*, vol. 44, no. 10, pp. 2143–2154, 2018, ISSN: 0301-5629. DOI: https://doi.org/10.1016/j.ultrasmedbio.2018.06.009. [Online]. Available at: https://www.sciencedirect.com/science/article/pii/S0301562918302643.

[10] D. S. dos Santos et al., "A tiled ultrasound matrix transducer for volumetric imaging of the carotid artery," *Sensors*, vol. 22, no. 24, 2022, ISSN: 1424-8220. DOI: 10.3390/s22249799. [Online]. Available at: https://www.mdpi.com/1424-8220/22/24/9799.

[11] P. Acoustics, *AptFlex F7*, English, Precision Acoustics, 5 pp. Accessed: Mar. 2, 2025. [Online]. Available at: https://www.acoustics.co.uk/wp-content/uploads/2023/06/Aptflex-F7NC-TDS-V2-0423.pdf.

[12] P. Acoustics, *0.2 mm needle hydrophone (nh0200)*, English, Precision Acoustics, 8 pp. Accessed: Mar. 2, 2025. [Online]. Available at: https://www.acoustics.co.uk/wp-content/uploads/2022/03/NH0200-0.2mm-Needle-hydrophone-TDS-V1-0222.pdf.

[13] L. W. Schmerr, *Fundamentals of Ultrasonic Phased Arrays*. Springer, 2015, pp. 20–24.

[14] P. Acoustics, *Transducer test certificate*, English, Precision Acoustics, 4 pp.

[15] P. Acoustics, *Submersible Preamplifier & DC Coupler*, English, Precision Acoustics, 3 pp. Accessed: Mar. 2, 2025. [Online]. Available at: https://www.acoustics.co.uk/wp-content/uploads/2022/03/Submersible-preamplifier-and-DCPS-TDS-V1-0222.pdf.

[16] Miteq, *AU-1519*, English, Miteq, 3 pp.

[17] P. H. Rogers and A. L. Van Buren, "An exact expression for the lommel-diffraction correction integral," *the Journal of the Acoustical Society of America*, vol. 55, no. 4, pp. 724–728, 1974.

[18] P. Acoustics, *1.0 mm needle hydrophone (nh1000)*, English, Precision Acoustics, 8 pp. Accessed: Mar. 2, 2025. [Online]. Available at: https://www.acoustics.co.uk/wp-content/uploads/2022/03/NH1000-1.0mm-Needle-hydrophone-TDS-V1-0222.pdf.

4

High-Volume-Rate Imaging Using The CMUT-on-ASIC Probe

This chapter is planned for publication in IEEE Transactions on Ultrasonics, Ferroelectrics, and Frequency Control

4.1. Introduction

This chapter covers the characterization and comparison of a set of imaging strategies that have been designed for the abdominal aorta (AA) probe described in Chapters 2 and 3, using both simulation and experimental results. As aforementioned, a 60°×60°×10 cm imaging volume is targeted to image all but the most extreme abdominal-aortic-aneurysm (AAA) sizes at various depths, as indicated in Figure 4.1. Given a 1540 m/s (typical) speed of sound in human tissue, imaging a 10 cm depth allows for a pulse-repetition frequency (PRF) of 7.7 kHz, allowing 4 pulse-echo acquisitions to reconstruct a volume at a ∼2 kHz volume rate. This necessitates diverging-wave transmissions with large opening angles to cover the full volume, with synthetic focusing in receive (RX) to reconstruct images.

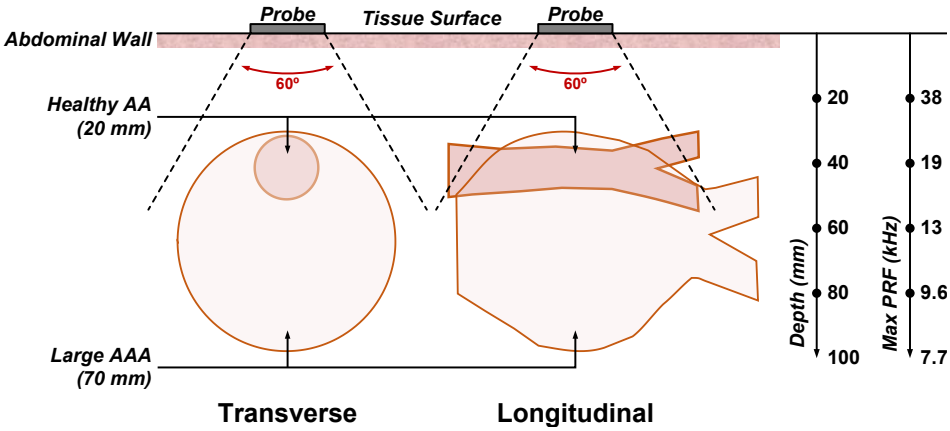

Figure 4.1: Overview of volume to be imaged to cover most AAAs.

Section 2.5.4 qualitatively demonstrated the performance of this imaging strategy. However, to evaluate suitability for AAA imaging, a quantitative analysis of the probe's imaging performance is also necessary. Moreover, as demonstrated in [1], image resolution improves marginally and contrast improves substantially with coherent compounding of beamformed RX data from differing angles, at the cost of volume-rate. As flow speeds in the AA and other medical applications where this probe is potentially suitable can widely vary [2], [3], it is desirable to understand how trading off volume-rate for improved image quality works out for this probe. Imaging schemes with up to 9 pulse-echo acquisitions per image are considered, as that many transmit (TX) profiles can be pre-loaded in the probe to maximize the volume-rate.

The probe consists of 2 32×64-element tiles, the imaging arrays of which are subdivided into 8-element subgroups, consisting of two 2×2-element sub-apertures (SAPs) (Section 2.2.2). The SAPs implement 4× channel-count reduction via a delay-and-sum micro-beamformer (µBF), the outputs of which are combined via 2× time-division multiplexing (TDM). In addition, the reduction in TDM-induced crosstalk by channel equalization was demonstrated (Section 2.5). However, the effect of this crosstalk on image quality was not quantified, which this chapter also aims to do.

Due to yield issues with getting both tiles in a probe fully functional, imaging performance has been evaluated with only one tile. While a loss in resolution along the short-axis of one tile is expected, use of one tile still provides a significant

improvement over the state-of-the art [1], [4], [5], [6], [7], [8]. A comparison of image performance along the long-axis of one tile is expected to give a decent quantitative indication of how the full array will perform along both axes due to symmetry.

The outline of this chapter is as follows. Section 4.2 covers the methods for the comparison of the imaging schemes of interest. This involves a short overview of the imaging array used, the set of TX beams used for all imaging schemes, and the method of RX beamforming. In addition, the measurement setups for quantifying the achievable image resolutions and capabilities of tracking flow speeds are covered. Section 4.3 covers the TX and RX performance of the array, and presents a comparison of the imaging performances achieved. Section 4.4 discusses these results and Section 4.5 presents the conclusions of this chapter.

4.2. Methods

4.2.1. Imaging Array Definition

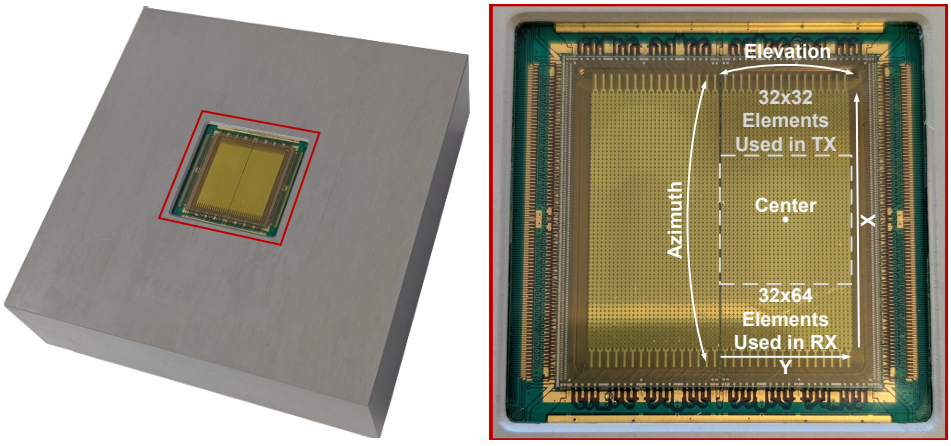

Figure 4.2: Definition of the imaging array dimensions of the probe used.

For AA imaging, pulses with a center frequency around 2 MHz to 4 MHz are typically used. This is a result of the trade-off between penetration depth, which decreases with a higher center frequency, and resolution, which increases with a higher frequency [9]. The choice of center frequency also affects the amount of

channel-count reduction possible for a given RX channel bandwidth and volume rate. As a trade-off between these different design considerations, a transducer array with a center frequency around 3 MHz and a -6 dB bandwidth of at least 50% was targeted. Towards this end, results with the Xiver CM5 capacitive micro-machined ultrasound transducer (CMUT) device are presented, which has a drum size of 364 µm, a 2.6 MHz center frequency (f_c) and 93% bandwidth (BW) [10], and a 365 µm pitch.

Figure 4.2 shows the definition of the array that will be adhered to in this chapter. As one tile is used for imaging, the array consists of 32×64 elements, where the Y-axis is the short side of the array, and the X-axis is the long side. The elevation axis is along the Y-axis of the array and the azimuthal axis is along the X-axis of the array.

4.2.2. Definition of Imaging Schemes

As the aforementioned imaging array has a pitch that is larger than half the wavelength of the transmitted ultrasound waveforms, and consists of 2×2 SAPs with µBFs, the grating-lobe-free FoV that can be imaged per pulse-echo acquisition is limited. As such, to avoid illuminating grating lobes, while maximizing the field-of-view (FoV) per acquisition, the TX beams and SAP directivity used for the investigated imaging schemes are covered next.

Definition of TX Beams

Figure 4.3 shows the dimensions of the set of 9 TX beams used for all imaging schemes under test and simulated cross-sections of 3 beams. The beams were simulated in Field-II [11] using the same delays that are programmed to the TX BF in the probe. The central 32×32-element section of the array is used to make the beams symmetrical along azimuth and elevation to avoid illuminating grating lobes in RX (see Appendix A.1). Each TX beam has a 30°×30° opening angle, where the angles along both azimuth and elevation are varied from -15° to 15°. The transmitted waveforms are 2-period pulses at f_c, which have a 39% BW (Section 3.3.3).

	Beam 1	Beam 2	Beam 3	Beam 4	Beam 5	Beam 6	Beam 7	Beam 8	Beam 9
Angle Azimuth	-15°	-15°	-15°	0°	0°	0°	15°	15°	15°
Angle Elevation	15°	0°	-15°	15°	0°	-15°	15°	0°	-15°
Opening Angle	30°×30°	30°×30°	30°×30°	30°×30°	30°×30°	30°×30°	30°×30°	30°×30°	30°×30°

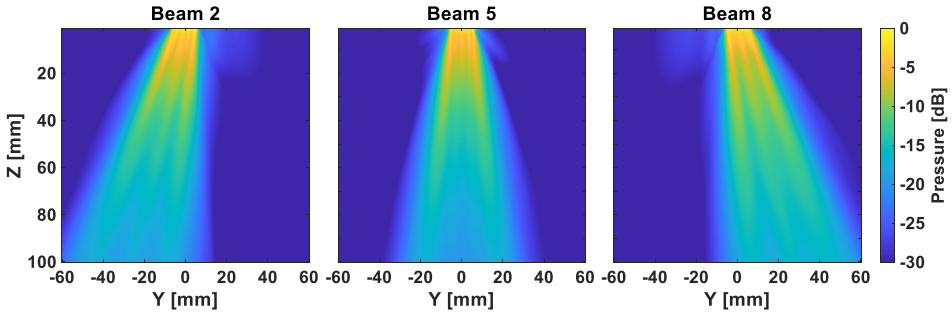

Figure 4.3: Overview of TX beams for investigated imaging schemes and simulated cross-sections of 3 beams.

Table 4.1: Overview of imaging schemes

Scheme	TX Beams	Subgroup SAP Output
1	[1 3 7 9]	TDM (Both 1 and 2)
2	[1 2 3 4 5 6 7 8 9]	TDM (Both 1 and 2)
3	[1 1 3 3 7 7 9 9]	[1 2 1 2 1 2 1 2]
4	[1 2 3 4 5 6 7 8 9 1 2 3 4 5 6 7 8 9]	[1 1 1 1 1 1 1 1 1 2 2 2 2 2 2 2 2 2]

Overview of Investigated Imaging Schemes

Table 4.1 gives an overview of the TX beams and the subgroup settings used to image a volume at a high volume-rate. The steering angle of all SAPs in the array are configured to be the same as the TX beam steering angle. In total, 4 imaging schemes are compared: One with 4 pulse-echo acquisitions per frame (Scheme 1), one with 9 (Scheme 2), one with 8 (Scheme 3), and one with 18 (Scheme 4). Schemes 1 and 2 use TDM to output both SAPs in each subgroup per acquisition. Schemes 3 and 4 multiplex the SAPs, thus requiring sections to be scanned twice to read out the whole array. In static phantoms, the only difference in image quality between Schemes 1 and 3, and 2 and 4, are TDM-induced crosstalk, thus allowing the degradation in image quality from this artifact to be quantified. For

investigating Doppler imaging performance and image quality, only Schemes 1-3 are used due to their higher volume rate versus Scheme 4. At a PRF of 8 kHz, these are 2 kHz, ∼888 Hz, and 1 kHz respectively.

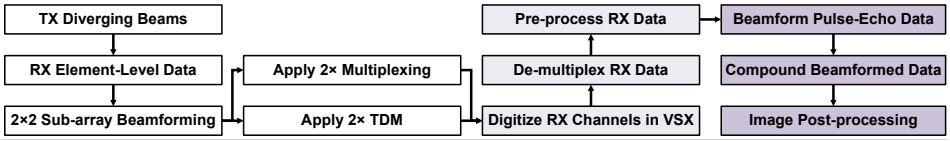

Figure 4.4: Block diagram of the imaging acquisition and processing steps.

Figure 4.4 shows a block-diagram of the imaging acquisition and processing steps. As will be covered in more detail in Section 4.3.1, once the VSX digitizes the RX output channels of the probe, equalization can be applied during the de-multiplexing step to reduce TDM-induced crosstalk. The RX data is then post-processed, which involves correcting for any time-offsets between TX and RX that the system introduces and optionally applying TGC. Data from individual pulse-echo acquisitions are then beamformed, where the data is apodized with a Tukey window with 50% tapering and an f-number as close as possible to 1.0 is used for beamforming each point. The sub-images are apodized with a Hanning window and an f-number of 1.2 is used when reconstructing the final image data by compounding the beamformed data from a set of pulse-echo acquisitions (see Table 4.1). To render the images, the image data is post-processed by applying the Hilbert transform and log compression.

For Doppler imaging, which is further covered in Section 4.2.6 and Section 4.3.4, a singular value decomposition (SVD) is applied to the beamformed frames. The first N columns and last M columns of the resulting singular value matrix (Σ) are made zero to band-pass-filter the data. A lag-1-autocorrelation is then applied to ensembles with a length of 15 frames. These are spatially filtered with a 3×3×3 Hamming window. The phase is then extracted to find the estimation of the axial velocity, after which 85 resulting frames are averaged to produce the final Doppler image.

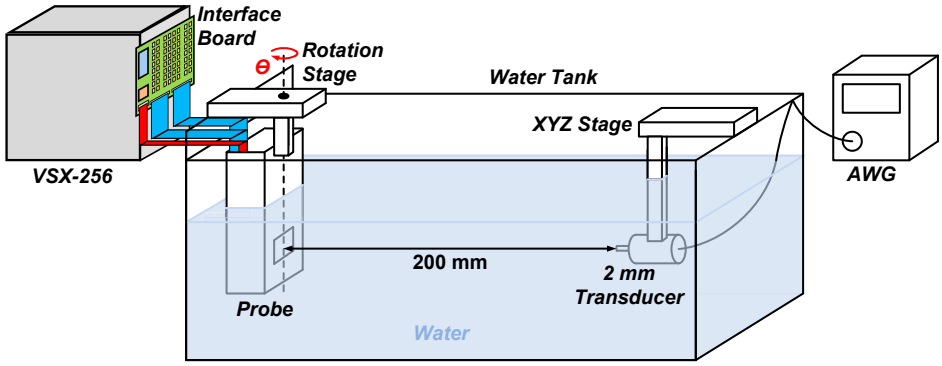

Figure 4.5: Measurement setup for validating the SAP directivity.

4.2.3. Simulation and Measurement of TX and RX Directivity

Figure 4.5 shows the measurement setup for validating the SAP directivity, which is the same as the setup used for measuring the element RX directivity in Section 3.2.7 (Figure 3.9). The same sample was also used. All other measurements use the sample shown in Figure 4.2. A first-order approximation of the SAP directivity in one dimension ($D(\Theta, \Phi)$), which is used as a reference, is described by the following equation [12]:

$$D(\Theta, \Phi) = \frac{\sin\left[Mks(\sin\Theta - \sin\Phi)/2\right]}{M\sin\left[ks(\sin\Theta - \sin\Phi)/2\right]} \tag{4.1}$$

where M is the SAP element count in one dimension, $k = 2\pi f/c$ with f the RX frequency and c the speed of sound, s is the element pitch, Φ is the steering angle, and Θ is the RX angle.

Figure 4.6 shows the measurement setup for validating the directivity of the set of TX beams, which is the same as the setup used in Section 2.5.3 (Figure 2.16). The hydrophone is the same as the pre-calibrated 200 µm device [13] used in Section 3.2.6, and the same method for compensating for the directivity of the hydrophone is applied. The TX beams are also simulated in Field-II [11] for reference, where the same 2-period pulse is used for excitation and the same delays are used for the 32×32-element TX array.

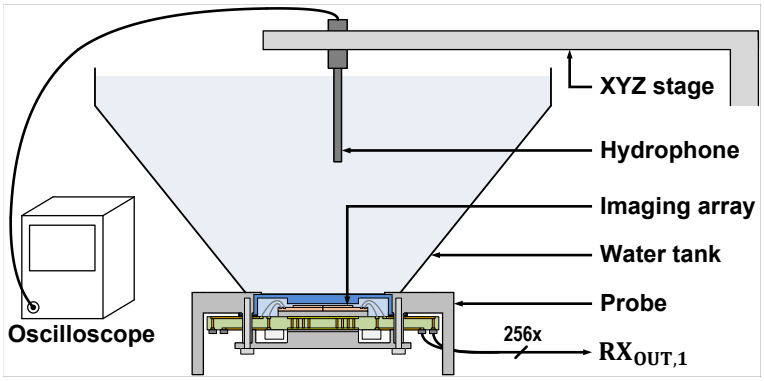

Figure 4.6: Measurement setup for validating the TX beams used in Schemes 1-4.

4.2.4. Simulation and Measurement of the Point Spread Function

To evaluate the point spread function as a function of depth, the elevation and azimuth angle, a 3-dimensional (3D) phantom was made using wires with diameters less than 10 µm [14], which is about 60× smaller than the wavelength at the center frequency f_c of the pulses transmitted, and thus will not significantly affect the full-width-half-maximum (FWHM) of the point-spread-function (PSF). Figure 4.7(a) shows a picture of the wire phantom and Figure 4.7(b) shows a diagram with the approximate locations of the wires. The wires are spun at 5 angles along both the X and Y axis of the probe, covering most of the full FoV. To image the wires, the phantom is placed in a container filled with demiwater, on which the probe is mounted. As demiwater is an (almost) non-attenuating medium, the application-specific integrated circuit (ASIC) pulsers drive the CMUTs in the array at a 5 V peak-peak amplitude, rather than the 40-V maximum they are capable of.

The exact positions of the wires are determined from imaging the phantom (covered in Section 4.3.2). The imaging schemes are also simulated in Field-II [11] with an emulated phantom that models the cross-section of each wire in azimuth and elevation as a single point scatterer in the same positions as measured. In measurement, the FWHM in the axial direction (ρ) is determined from cross-sections of all spun wires, whereas the FWHM in elevation is determined from the cross-section of wires spun along the X-axis of the probe and the FWHM in azimuth from those spun along the Y-axis. In simulation, as the cross-section of each wire is modeled as ideal point scatterer, all points are used to determine the

FWHM in all three dimensions.

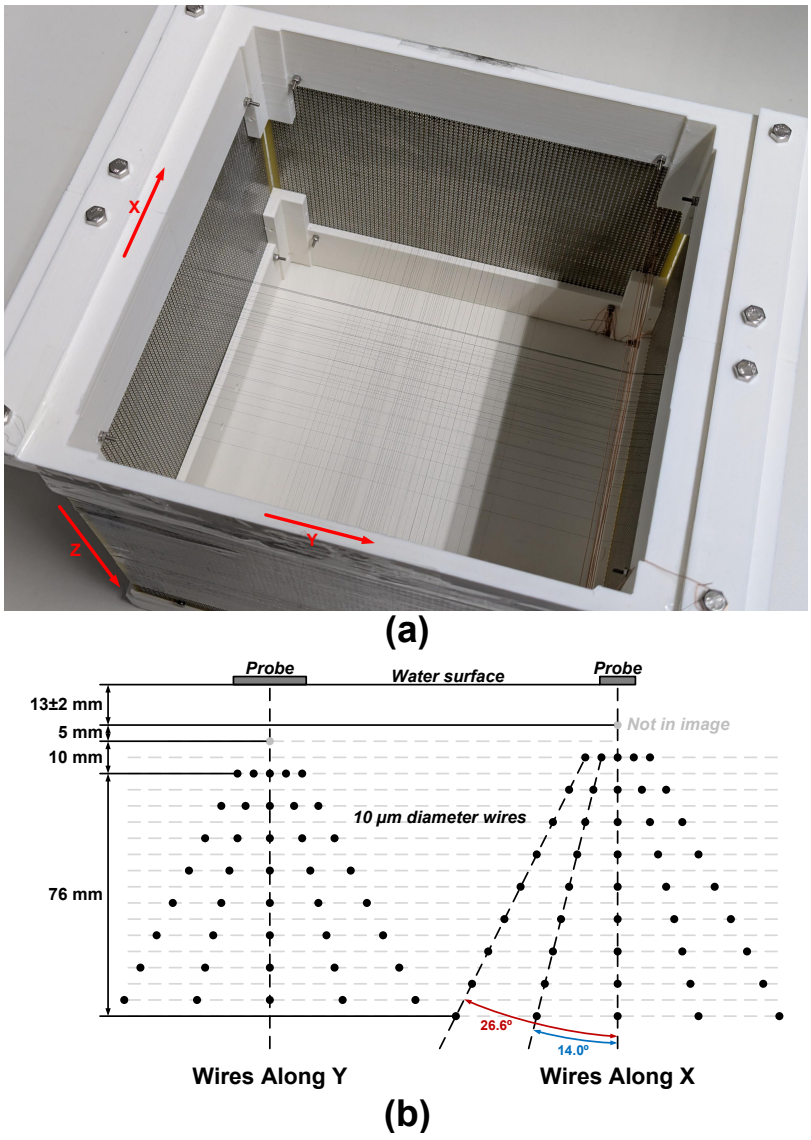

Figure 4.7: (a) Picture of the fabricated wire phantom outside of a water tank. (b) Diagram of the wire phantom in a water tank.

4.2.5. Simulation and Measurement of Image Quality

A CIRS 040GSE phantom [15] is used to evaluate the image quality of Schemes 1-3. Figure 4.8(a) shows an overview of the measurement setup used to evaluate the image quality along elevation and azimuth. In both cases, the probe is positioned to approximately cover the same region in the phantom. An ultrasound gel pad [16] is used as interposer to acoustically couple the probe to the phantom. Figure 4.8(b) shows a diagram of the imaged medium with the associated offset from the interposer.

The image quality is assessed based on the hyperechoic cylinder and the two stepped anechoic cylinders, of which the diameters change in the phantom, within the FoV. As the metric for quantifying contrast varies in literature [17], [18], [19], [20], both the contrast ratio in dB (CR_{dB}) and contrast-to-noise ratio (CNR) are used. The CR_{dB} is determined using the following equation [17], [18]:

$$CR_{dB} = 10\log\frac{\mu_i}{\mu_o} \tag{4.2}$$

where μ_i is the mean signal power inside a cylinder, and μ_o is the mean signal power outside a cylinder. As both the spatial resolution (in cartesian coordinates) and signal-to-noise ratio (SNR) decrease versus distance, μ_o is determined based on speckle close to the evaluated cylinders. The blue, purple and red circles in Figure 4.8(b) indicate where the CR_{dB} are calculated for the hyperechoic and two anechoic cylinders, which will be referred to as the $CR_{dB,h}$, $CR_{dB,a1}$ and $CR_{dB,a2}$, respectively.

The CNR is determined using the following equation [19], [20]:

$$CNR = \frac{|\mu_i - \mu_o|}{\sqrt{\sigma_i^2 + \sigma_o^2}} \tag{4.3}$$

where μ_i and μ_o are the mean signal powers, and σ_i and σ_o are the standard deviation of the signal powers within the assessed regions inside and outside a cylinder, respectively. Similar to the CR_{dB}, the CNR_h, CNR_{a1} and CNR_{a2} represent the CNR for the same cylinders, calculated using the same blue, purple and red highlighted regions in Figure 4.8(b).

To validate the effect of noise on the image quality, the CMUTs in the array are driven with the same 5 V 2-period pulse as for the aforementioned wire phantom measurements. To distinguish between noise and clutter, the CR_{dB} and CNR will be compared for one acquired frame, and with 16 averaged frames. In addition, to minimize the effect of signal attenuation in the medium, an exponential time-gain

compensation (TGC) is applied such that the average background signal intensity from speckle and clutter is ρ-independent.

To ensure this, the average attenuation in the medium and a first-order indication of the imaging depth that the probe can achieve are derived by averaging the beamformed data in azimuth and elevation, which provides an estimate of the average signal levels in the medium along ρ. The scatterers in the CIRS phantom are assumed to have a random, uncorrelated distribution. As a result, the background speckle, clutter, and noise in the signal floor are expected to scale in the same way with averaging, whereas correlated signals from the wires and cylinders coherently add. As the speckle and clutter signal levels scale with the attenuation in the phantom, but the system noise is medium-independent, the signal floor is flat when speckle and clutter dominate after a correct TGC is applied, whereas the signal floor will exponentially increase when noise becomes dominant. This transition provides a first-order indication of the achievable imaging depth.

To compare measurement results, two similar phantoms were constructed and simulated in Field-II [11]. The objects in Figure 4.8(b) highlighted in purple are modeled in both. One phantom (Sim 1) consists of 100,000 point scatterers spread out over a 60×10×80 mm region, which visually emulate the speckle in the CIRS phantom, at a 30 mm depth from the probe aperture. The wire targets are also modeled as single point scatterers. While the anechoic stepped cylinders vary in diameter across the region of interest in the CIRS 040GSE phantom, the diameter of the bottom anechoic cylinder is fixed to 10 mm, and the top cylinder has a 6.7 mm diameter.

The second phantom (Sim 2) consists of 1,400,000 point scatterers spread out over a 140×60×80 mm region at a 30 mm depth from the probe aperture, and has the same scatterer density as Sim 1. The hyperechoic cylinder and wire targets are the same as in the first phantom, but the modeled anechoic cylinders have their diameters reduced to 6.7 mm and 4.5 mm, for the bottom and top cylinder, respectively. While the first phantom is a more ideal model for assessing the expected image quality, this second phantom more accurately models measurement conditions.

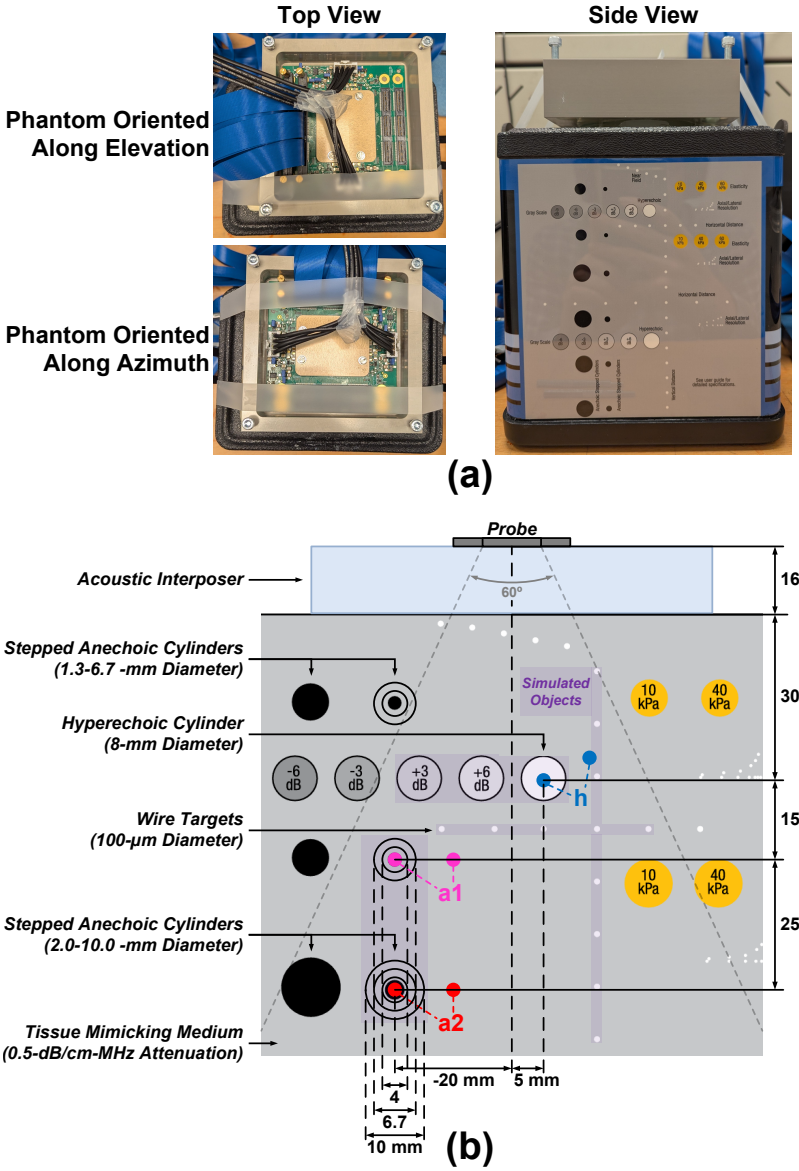

Figure 4.8: (a) Pictures of the measurement setup for imaging a CIRS 040GSE phantom oriented along azimuth and elevation. (b) Diagram of the objects imaged in the phantom. The colored circles indicate sections of the phantom used for CR_{dB} and CNR calculations. The objects highlighted in purple are modeled in Field-II simulations.

4.2.6. Flow Imaging Setup

Figure 4.9 shows the measurement setup for evaluating the Doppler imaging performance of the probe when using Schemes 1-3. CIRS 769DF Blood-mimicking fluid [21] is pumped at a constant flow rate by a syringe pump [22] through a CIRS ATS524 flow phantom [23] containing a tube with a 4 mm diameter. To acoustically couple the aperture of the probe to the acoustic medium of the phantom, the cavity on top of the phantom (see Figure 4.9(a)) is filled with water.

To determine the performance of the probe for flow in both azimuth and elevation, the phantom is angled along both the X and Y axis of the array, respectively. In both cases, the center of the probe is at an angle of approximately 8° and a radial distance of 26 mm to the cross-section of the tube, which is 15 mm below the surface of the phantom [23]. As this is lower than the maximum depth the probe is capable of, with an attenuation coefficient of 0.5 dB/cm-MHz, the medium attenuates ∼19-22 dB less than at the 10 cm depth the probe is designed for. To obtain an SNR comparable to what would be expected at the maximum depth, the voltage at which the ASICs pulsers drive the CMUTs in the imaging array is proportionally lowered to 5 V.

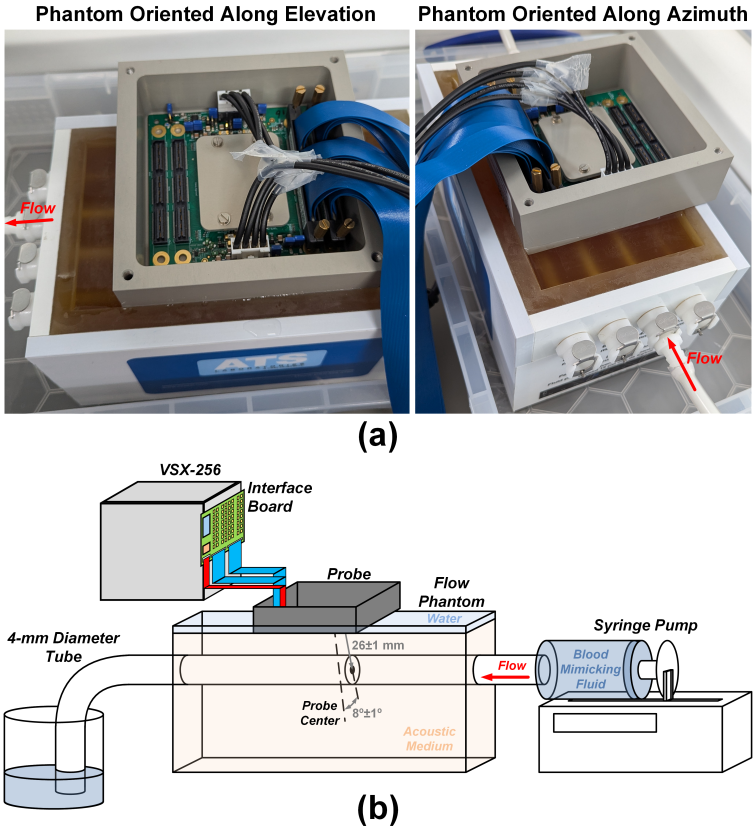

Figure 4.9: (a) Pictures of the measurement setup for imaging the flow through a 4 mm tube in a CIRS ATS524 flow phantom oriented along azimuth and elevation. (b) Diagram of the measurement setup.

4.3. Results

4.3.1. TX and RX Directivity

Figure 4.10 shows the measured directivity of a SAP when its µBF steers to the angles corresponding to TX beams 2, 5 and 8 (Figure 4.3). When receiving a 2-period pulse, which is representative for the typical ultrasound waveform transmitted, the average -3-dB beam widths of 20 SAPs are 29°, 38° and 28° for the -15°, 0° and 15° steering angles, respectively. When receiving a 2.6-MHz continuous wave, which is a conservative waveform for evaluating directivity, the average -3-dB beam widths are 26°, 41° and 27°. At 0°, the results are in line with equa-

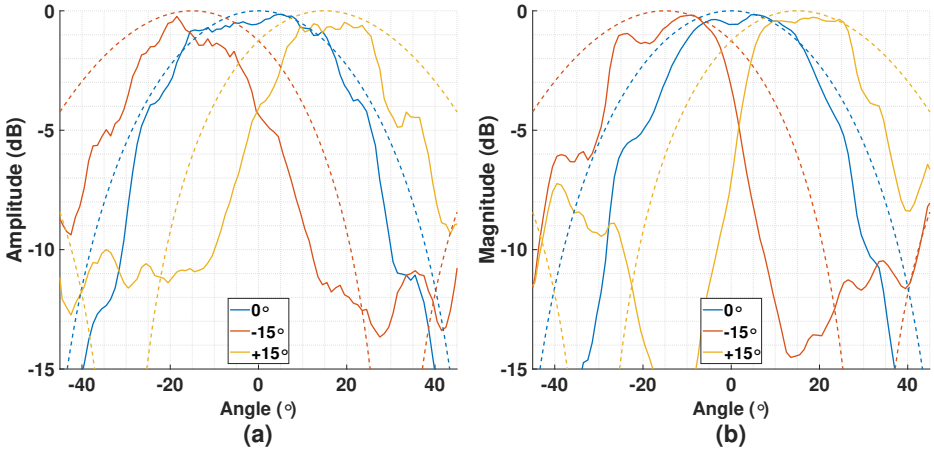

Figure 4.10: SAP directivity at a -15°, 0° and 15° steering angle. The solid lines are measured results, the dashed lines are from an analytical model. (a) Based on the peak-peak amplitude of a transmitted 2-period pulse. (b) Based on the magnitude of a transmitted 2.6-MHz continuous wave.

tion 4.1. However, at -15° and 15°, the measured beams are more narrow than the model predicts, which is likely due to crosstalk, which has been evaluated in more detail in Chapter 3. Nevertheless, the SAP has a sufficiently large FoV at all steering angles to cover the region of interest.

Figure 4.11(a) shows C-planes of the set of 9 TX beams (Figure 4.3) at 35 mm from the aperture and their respective -6-dB beam widths. As aforementioned, these results were simulated in Field II [11] using the same array delays as programmed in the probe. Figure 4.11(b) shows the corresponding measurement results. As the hydrophone acquired each point in the C-plane, the probe cycled through the 9 pre-loaded TX beam profiles at a PRF of 18 kHz. As demonstrated, the measured TX beams are in good agreement with the simulations.

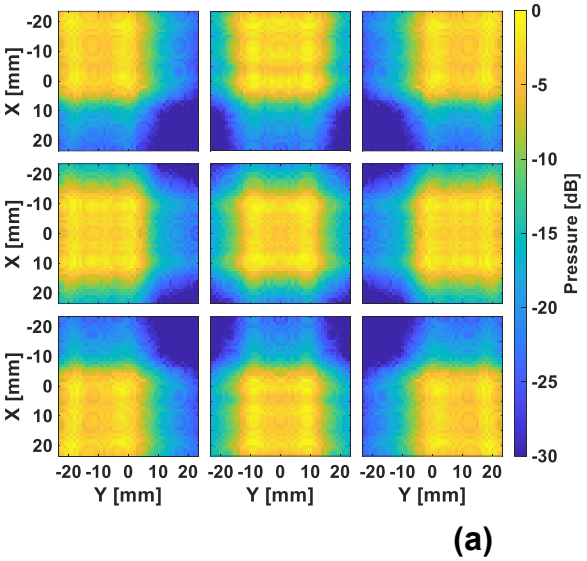

Beam No.	Beamwidth Along X	Beamwidth Along Y
1	27 mm	28 mm
2	26 mm	27 mm
3	27 mm	28 mm
4	27 mm	28 mm
5	24 mm	24 mm
6	27 mm	28 mm
7	27 mm	28 mm
8	29 mm	28 mm
9	27 mm	28 mm

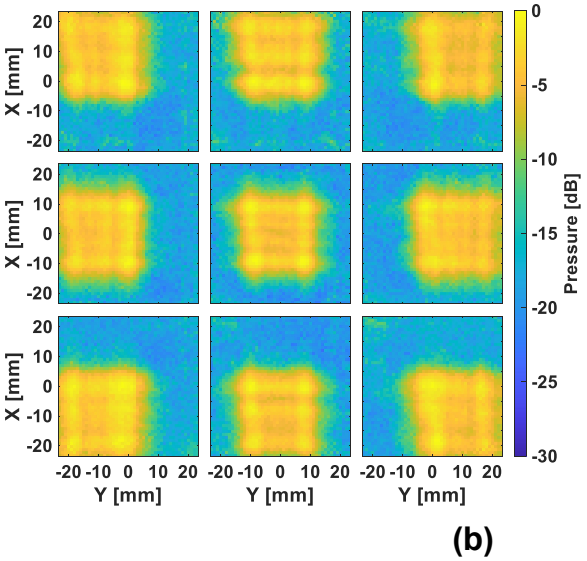

Beam No.	Beamwidth Along X	Beamwidth Along Y
1	26 mm	27 mm
2	25 mm	25 mm
3	27 mm	27 mm
4	24 mm	24 mm
5	23 mm	23 mm
6	24 mm	26 mm
7	24 mm	24 mm
8	27 mm	25 mm
9	25 mm	26 mm

Figure 4.11: C-plane at 35 mm from the array of 9 TX beams: (a) simulated; (b) measured.

4.3.2. Point Spread Function

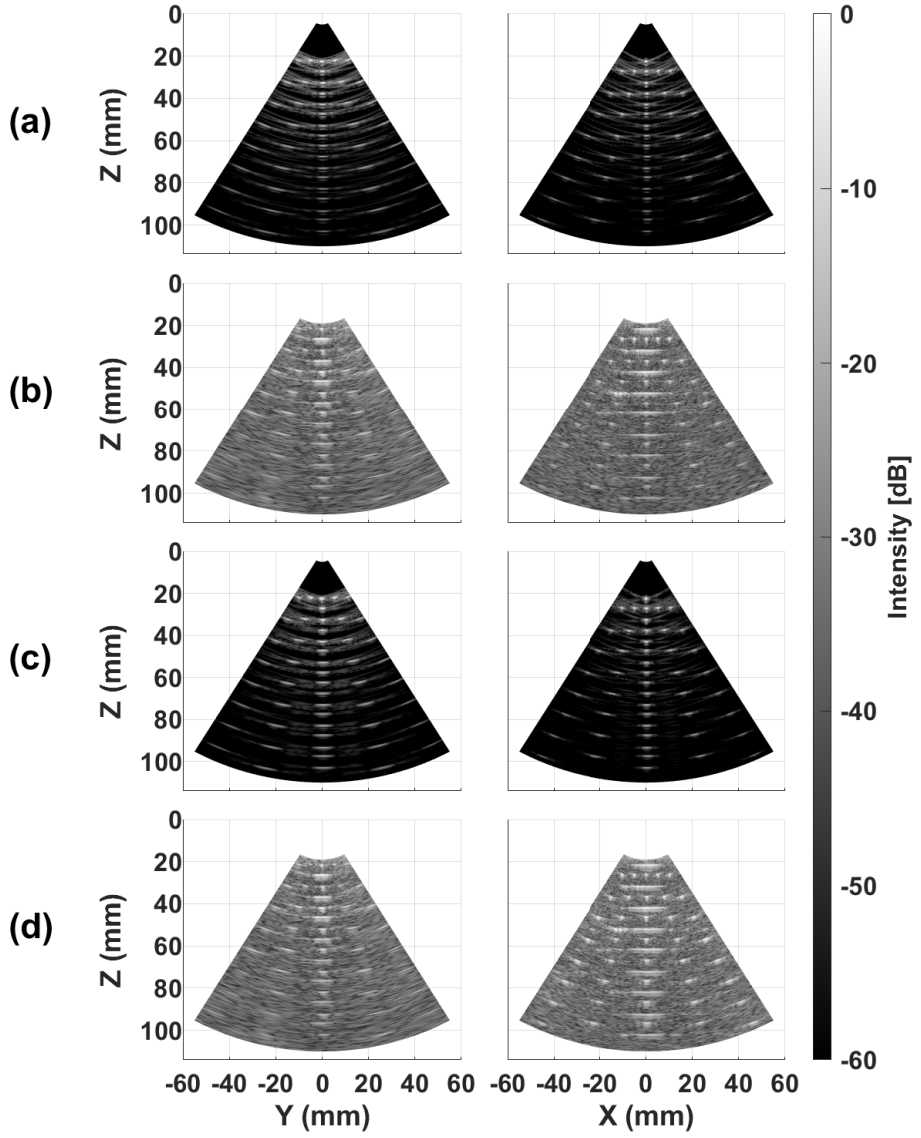

Figure 4.12: B-mode images of a wire phantom in azimuth and elevation. In the simulated phantom, wires are modeled as single point scatterers at the cross-sections of wires in the measured phantom. (a) Simulated using Scheme 1/3. (b) Measured using Scheme 1 with EQ. (c) Simulated using Scheme 2/4. (d) Measured using Scheme 2 with EQ.

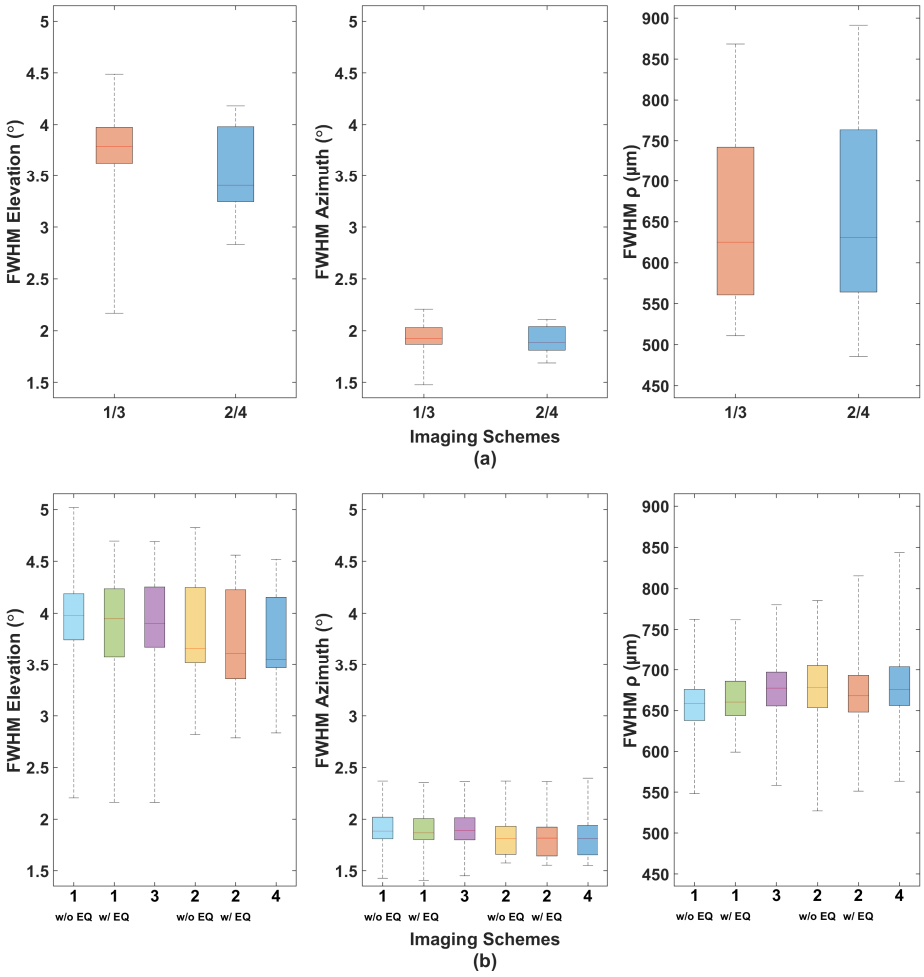

Figure 4.13: Distribution of the FWHM of the wire phantom using Schemes 1-4: (a) simulated; (b) measured.

Figure 4.12 shows an overview of B-mode images of the simulated and measured wire phantom along the X-axis and Y-axis of the probe. As the B-mode images using Scheme 1, with and without an equalizer (EQ) applied, and Scheme 3 look almost identical, only the images using Scheme 1 with EQ are shown in Figure 4.12(b). The same applies for Figure 4.12(d) regarding the use of Scheme 2 with EQ or without EQ, and Scheme 4.

Figure 4.13 shows corresponding box plots of the FWHM in elevation, azimuth and ρ compared to simulation. The median FWHM from measurement corre-

sponds well to simulation, where the medians using Schemes 1/3 diverge between 3-6%, and the medians using Schemes 2/4 diverge between 1-8%. As shown in Figure 4.13(b), the difference in the median FWHM between Scheme 1 and 3, and Scheme 2 and 4 is $\leq$3%, meaning that TDM-induced crosstalk does not significantly effect it, although the difference increases for outlying points. The typical reduction in FWHM when using 9 angles versus 4 (Schemes 2/4 versus Schemes 1/3) is 9%, 4% and -3% for elevation, azimuth and ρ, respectively.

4.3.3. Image Quality

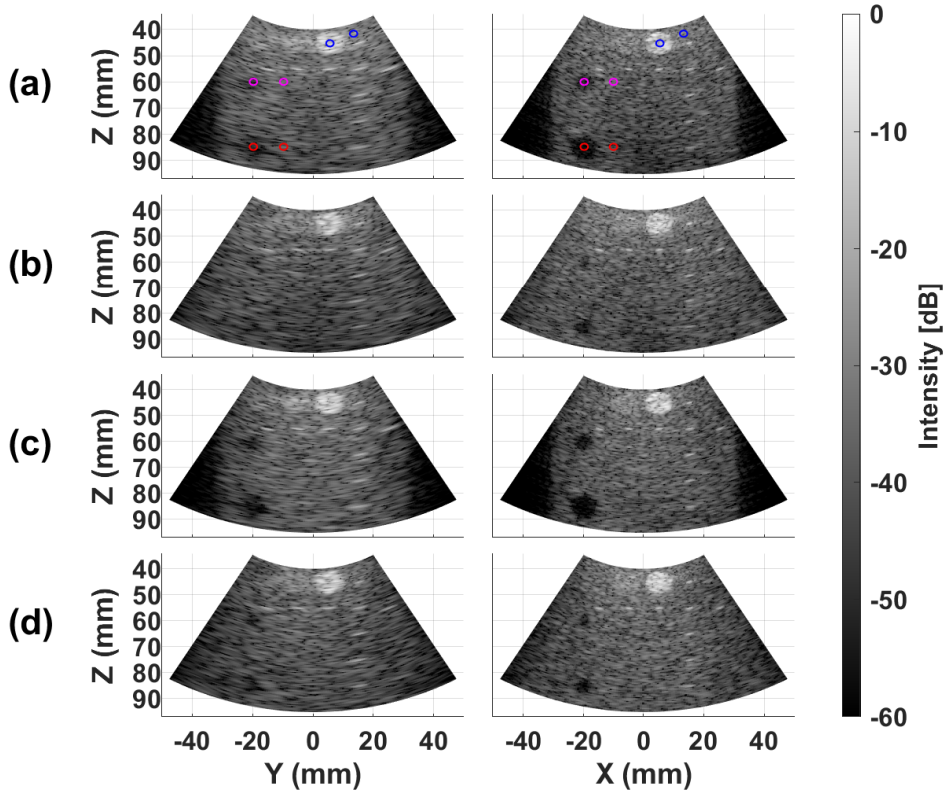

Figure 4.14: B-mode images of simulated CIRS phantoms Sim 1 and 2 with the probe rotated along azimuth and elevation. The colored circles indicate the regions used for CNR/CR calculations. (a) Sim 1 acquired with Scheme 1/3. (b) Sim 2 acquired with Scheme 1/3. (c) Sim 2 acquired with Scheme 2/4. (d) Sim 2 acquired with Scheme 2/4.

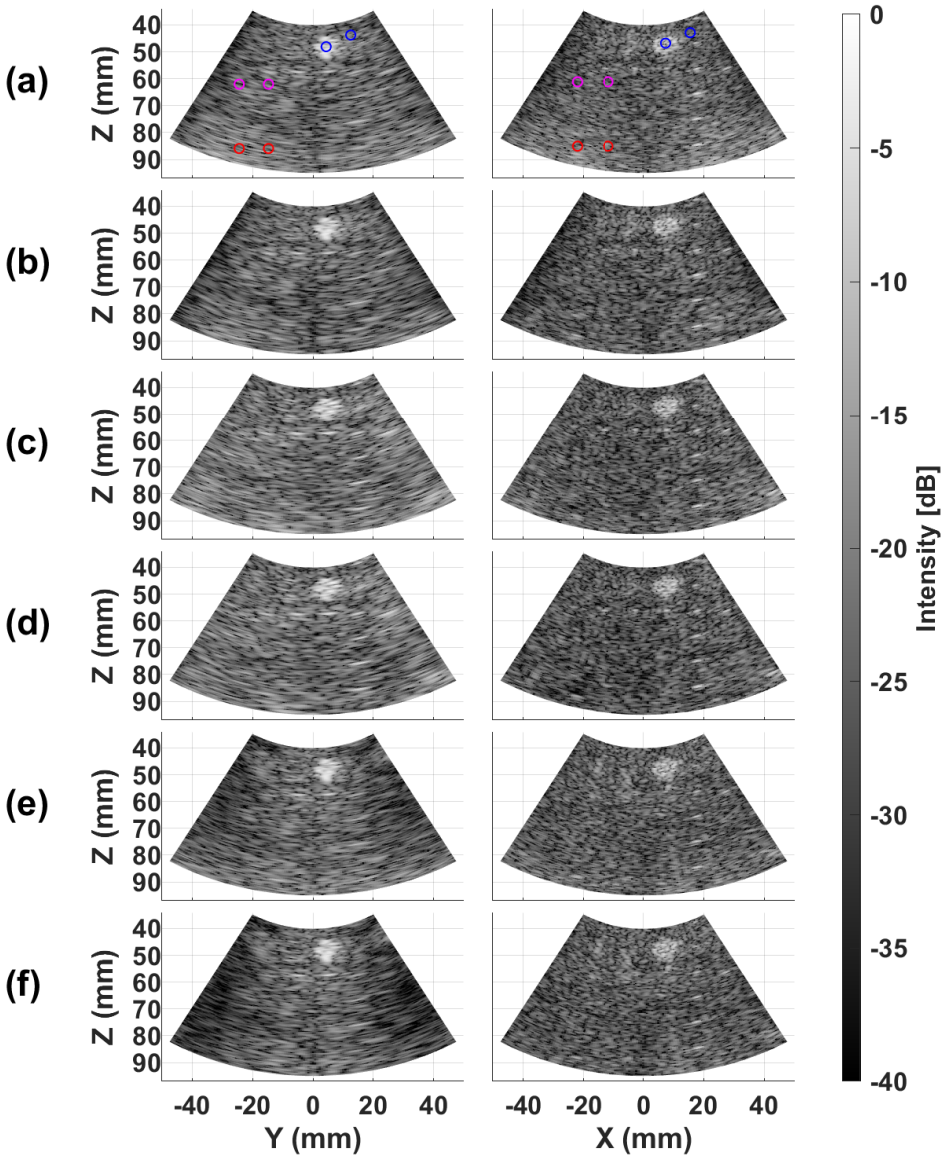

Figure 4.15: B-mode images of a measured CIRS phantom with the probe rotated along azimuth and elevation. The colored circles indicate the regions used for CNR/CR calculations. (a) Acquired with Scheme 1, with EQ. (b) Acquired with Scheme 1, with EQ, and with 16× averaging. (c) Acquired with Scheme 2, with EQ. (d) Acquired with Scheme 2, with EQ, and with 16× averaging. (e) Acquired with Scheme 3. (f) Acquired with Scheme 3, with 16× averaging.

Table 4.2: Overview of CR_{dB} and CNR simulations and measurements at the points shown in Figures 4.14 and 4.15.

		Elevation						Azimuth					
		1 Frame			16x Avg.			1 Frame			16x Avg.		
		h	a1	a2	h	a1	a2	h	a1	a2	h	a1	a2
CNR	**1 w/o EQ**	1.2	0.5	0.1	1.2	0.6	0.1	1.2	0.4	0.0	1.1	0.6	0.5
	1 w/ EQ	1.2	0.5	0.2	1.2	0.6	0.0	1.1	0.4	0.0	1.1	0.6	0.5
	2 w/o EQ	1.2	0.3	0.3	1.2	0.4	0.6	1.0	0.7	0.2	1.0	0.8	0.5
	2 w/ EQ	1.2	0.1	0.1	1.2	0.2	0.3	1.0	0.7	0.3	1.0	0.8	0.6
	3	1.2	0.5	0.0	1.2	0.6	0.5	1.2	0.3	0.1	1.2	0.4	0.2
	Sim 1 : 1/3	0.9	0.8	0.8	N/A	N/A	N/A	1.1	0.8	1.0	N/A	N/A	N/A
	Sim 2 : 1/3	0.7	1.0	0.8	N/A	N/A	N/A	0.9	0.9	0.8	N/A	N/A	N/A
	Sim 1 : 2/4	1.0	0.8	0.7	N/A	N/A	N/A	1.1	1.0	1.0	N/A	N/A	N/A
	Sim 2 : 2/4	0.8	1.1	0.9	N/A	N/A	N/A	1.0	0.8	0.9	N/A	N/A	N/A
CR_{dB}	**1 w/o EQ**	13.7	-4.4	0.4	14.4	-5.4	-0.4	12.3	-3.0	0.2	12.4	-4.8	-3.2
	1 w/ EQ	12.2	-3.7	1.1	12.6	-4.4	0.3	11.8	-3.3	0.2	11.9	-4.6	-2.9
	2 w/o EQ	13.1	-1.7	-2.2	13.2	-2.6	-3.9	12.7	-5.1	-1.6	12.8	-5.7	-6.2
	2 w/ EQ	11.9	-0.7	-0.8	12.1	-1.4	-1.9	12.4	-4.6	-2.0	12.5	-5.3	-6.3
	3	15.0	-5.0	-0.3	15.2	-7.0	-3.5	12.4	-2.1	0.9	12.3	-2.7	-1.1
	Sim 1 : 1/3	13.5	-12.3	-13.7	N/A	N/A	N/A	17.7	-14.2	-11.9	N/A	N/A	N/A
	Sim 2 : 1/3	14.6	-8.4	-9.0	N/A	N/A	N/A	15.7	-10.3	-9.2	N/A	N/A	N/A
	Sim 1 : 2/4	16.6	-16.9	-16.7	N/A	N/A	N/A	21.1	-20.8	-17.5	N/A	N/A	N/A
	Sim 2 : 2/4	18.2	-14.6	-13.0	N/A	N/A	N/A	19.6	-14.8	-16.5	N/A	N/A	N/A

h : hyperechoic cylinder at ∼46 mm depth.
a1 : anechoic cylinder at ∼61 mm depth.
a2 : anechoic cylinder at ∼86 mm depth.

Figures 4.14 and 4.15 show a set of B-mode images of the CIRS phantom oriented along azimuth and elevation using Schemes 1-3. Table 4.2 shows the CR_{dB} and CNR in the highlighted regions in both figures. All schemes perform well in the hyperechoic region (h) along both axes, although a slight degradation in performance for both the CR_{dB} and CNR are observed with EQ applied. However, performance in the anechoic regions (a1,a2) is substantially worse.

Using Scheme 1/3, the CNR_{a1} does not significantly improve with averaging in elevation and by $\leq$0.2 dB in azimuth. When using Scheme 2, averaging improves the CNR_{a1} by $\leq$0.1 dB in both directions. Similar for the $CR_{dB,a1}$, averaging only provides a minor improvement, meaning that it is likely a higher clutter that degrades imaging performance versus Sim 1 and 2. The CNR_{a2} and $CR_{dB,a2}$ see an improvement with averaging of 0-0.5 and 0.8-4.6 dB, depending on the imaging scheme, respectively.

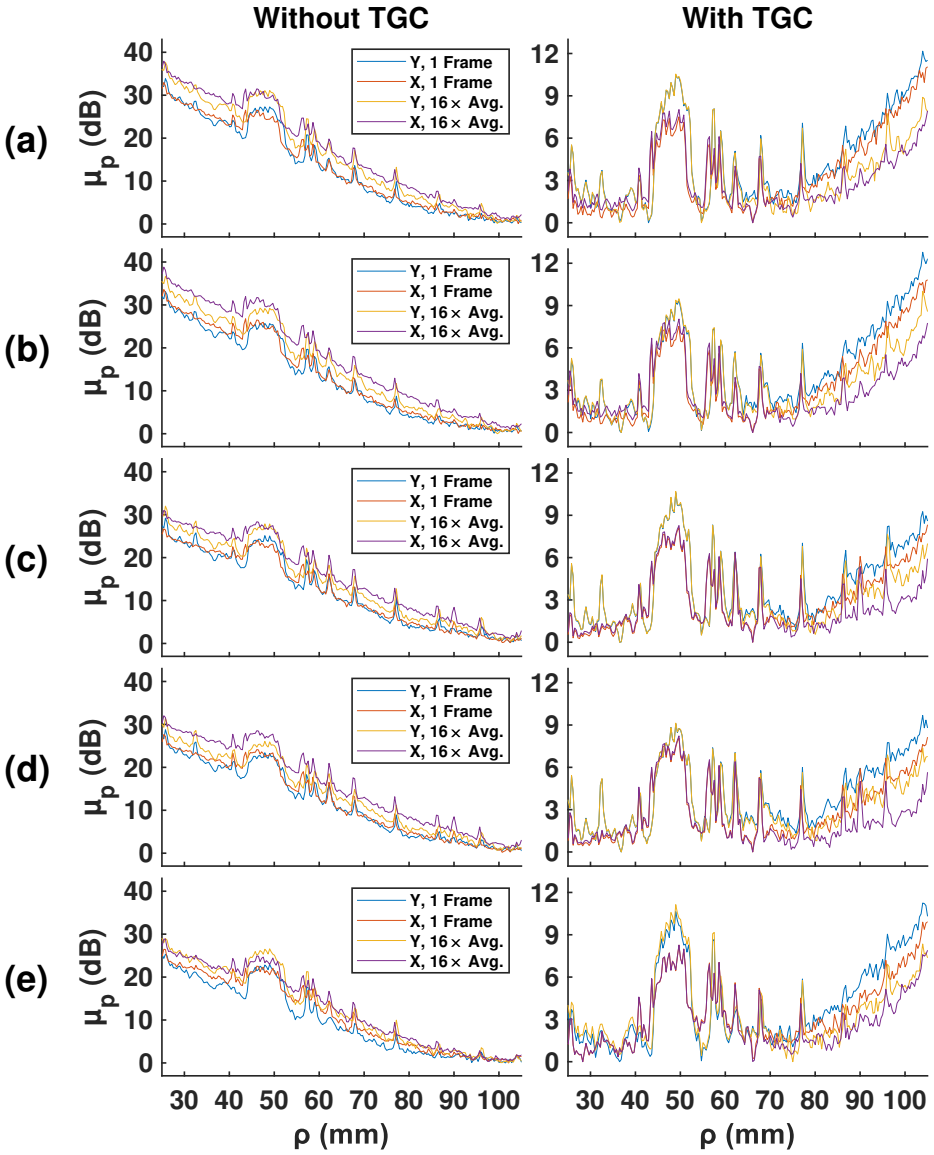

Figure 4.16: Mean power levels along ρ (μ_p), averaged in azimuth and elevation of the beamformed image data of a tissue mimicking (CIRS 040GSE) phantom, with and without TGC applied. (a) Acquired with Scheme 1, without EQ. (b) Acquired with Scheme 1, with EQ. (c) Acquired with Scheme 2, without EQ. (d) Acquired with Scheme 2, with EQ. (e) Acquired with Scheme 3.

This is in line with observations of the average background power levels in the beamformed data after TGC, as shown in Figure 4.16. Here, the mean power levels along ρ (μ_p), averaged in azimuth and elevation of the beamformed image data of the tissue mimicking (CIRS 040GSE) phantom, with and without TGC applied are shown. As mentioned in Section 4.2.5, the peaks are from reflections of wires and cylinders in the medium, whereas the signal floor is from reflections of the tissue-mimicking medium, clutter and noise, of which noise dominates from ∼75 mm with Scheme 1/3 and from ∼80 mm with Scheme 2 without averaging. With 16× averaging, this noise corner shifts to ∼85 mm with Scheme 1/3 and to ∼100 mm with Scheme 2.

However, even with averaging, there is a significant discrepancy in CR_{dB} and CNR between measurements and simulations, as shown in Table 4.2. The discrepancy between the averaged measured CR_{dB} and Sim 2 in regions a1 and a2 are 1.4-13.2 dB and 5.5-11.1 dB, respectively. The discrepancy between the averaged measured CNR and Sim 2 in regions a1 and a2 are 0.0-0.9 and 0.3-0.8, respectively. These discrepancies are expected to be due to added clutter, as the image quality of Sim 2 is significantly lower than Sim 1, which only models a larger part of the phantom and a different section of the stepped anechoic cylinders.

4.3.4. Flow Imaging

Figure 4.17 and 4.18 show color Doppler images of the flow phantom (Figure 4.9), oriented along elevation and azimuth at varying flow speeds, imaged using Schemes 1-3. These images have been made from 100 beamformed frames. During the SVD-filtering step (see Section 4.2.2), the first 8 and 13 columns of Σ are made zero when imaging 100 mm/s and 400 mm/s flow speeds, respectively. In both cases, columns 69 and above are also made zero. In both directions, Scheme 1 and 2, with and without EQ perform similar at 100 mm/s, whereas images using Scheme 2 have aliasing artifacts at a flow speed of 400 mm/s. This can be observed through the apparent velocity in the middle of the tube, where the flow speed is the highest, which is opposite to the expected flow direction in the tube. Similar artifacts are also present in the Doppler images when using Scheme 3, in addition to an overestimation of flow speeds at 100 mm/s.

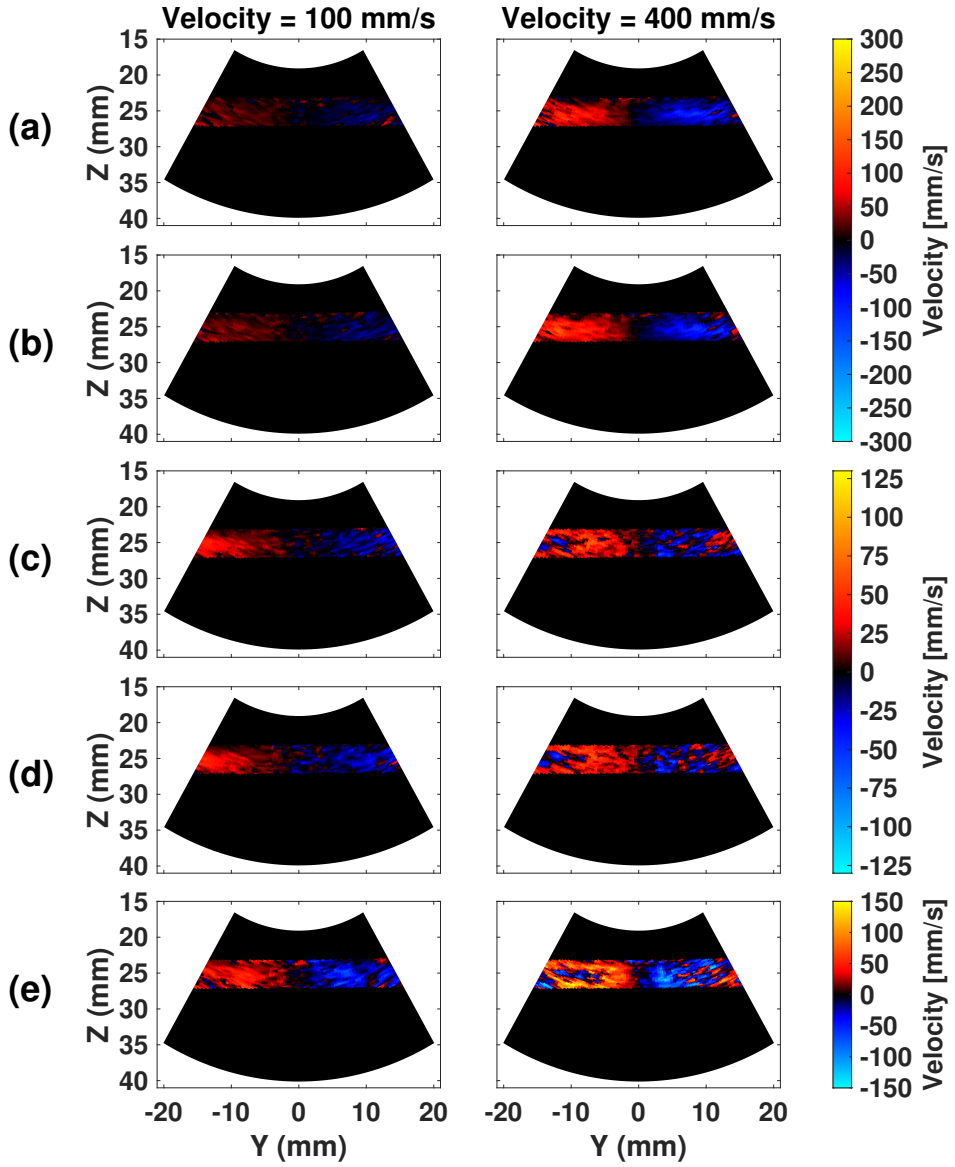

Figure 4.17: Color Doppler images of blood mimicking fluid flowing along elevation through a tube with a 4-mm inner diameter at varied velocities, scaled to the maximum velocity that can be tracked [24] without compensating for the angle between the probe and the tube. (a) Acquired with Scheme 1, without EQ. (b) Acquired with Scheme 1, with EQ. (c) Acquired with Scheme 2, without EQ. (d) Acquired with Scheme 2, with EQ. (e) Acquired with Scheme 3.

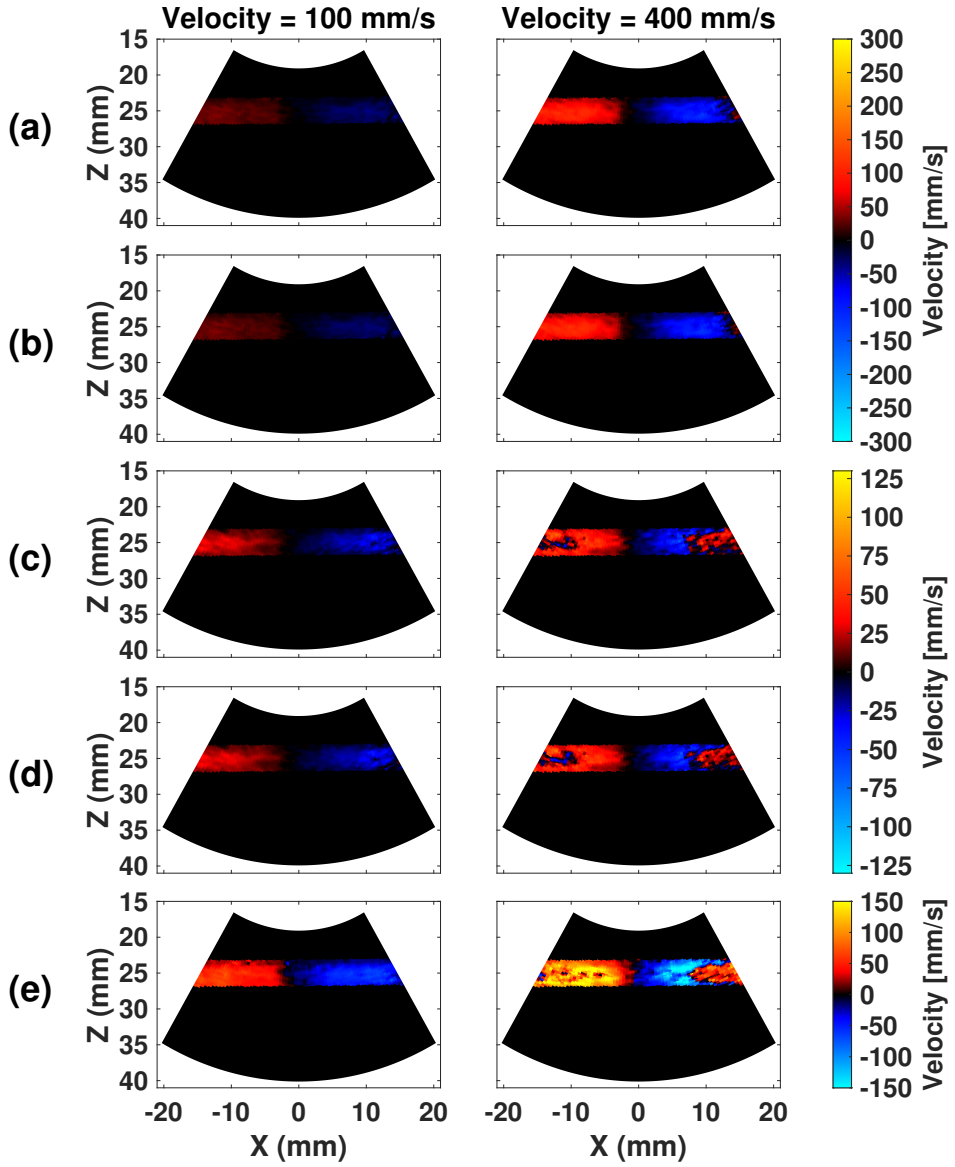

Figure 4.18: Color Doppler images of blood mimicking fluid flowing along azimuth through a tube with a 4-mm inner diameter at varied velocities, scaled to the maximum velocity that can be tracked [24] without compensating for the angle between the probe and the tube. (a) Acquired with Scheme 1, without EQ. (b) Acquired with Scheme 1, with EQ. (c) Acquired with Scheme 2, without EQ. (d) Acquired with Scheme 2, with EQ. (e) Acquired with Scheme 3.

4.4. Discussion

4.4.1. Directivity Measurements

As demonstrated in Section 4.3.1, both the TX and RX directivity cover the desired FoV. However, there is a discrepancy in the method of evaluating both, where the RX directivity was evaluated radially along one axis of the array using the axis-symmetry of the SAPs, whereas the TX beams were evaluated based on a C-plane scan. These discrepancies are present due to limitations in the XYZ-stage used for the TX directivity measurements (see Figure 4.6), where movements in the XY-plane can be automated, but adjustments along the Z-axis are manual. A more consistent method of evaluating the TX directivity would be to use a similar method as described in Section 3.2.7 (Figure 3.9), where the XYZ-stage is capable of moving in an automated way along all three axis, thus allowing radial scanning around the origin of the array and providing a direct measurement of directivity in degrees, rather than a derived one.

4.4.2. Image Quality

As aforementioned, the measured PSF in the evaluated images and contrast measurements of the hyperechoic cylinder in the evaluated CIRS phantom align with expectations. However, the measured contrast of the anechoic cylinders are lower than simulations predict. While noise partially contributes to this reduction in contrast for anechoic cylinders deeper in the phantom, it does not explain the discrepancy for the cylinder evaluated at a relatively shallow depth (∼60 mm). While higher-than-expected clutter is therefore the more likely cause, it is currently unknown what the source of this clutter is. A possible explanation for the discrepancy could be due to the limitations of the Born approximation used in Field-II [11], [25], which does not take into account multiple scattering within the phantom.

4.4.3. Flow Imaging

While a laminar flow of blood-mimicking fluid through a phantom was measured to showcase the basic capabilities of the probe and the evaluated imaging schemes,

further evaluation is required to determine how effective the presented imaging strategies are for imaging the 3D flow through a AAA. The maximum average flow speed evaluated was 400 mm/s, as this is the maximum speed that could be generated through the phantom by the syringe pump that was available. While this is similar to typical peak velocities in AAAs [26], [27], they can be as high as 1 m/s [28]. As such, a repeat of the presented measurements at higher flow speeds using a different pump could act as a better benchmark. In addition, a well-defined pulsatile flow through a larger tube would also be more representative for imaging a AA than the evaluated constant laminar flow.

As indicated in Section 4.2.6, the angle at which the flow was measured is also the most conservative orientation of the probe, where it is at a 90° angle to the flow direction. While a region at an up to 30° angle to the probe is scanned, the outer angles of the 60°×60° scanning volume have a 6 dB or lower SNR than at the peak-SNR regions of any evaluated imaging scheme. Therefore, for future evaluation, it could also be valuable to measure the flow with the probe oriented at multiple angles, which are more realistic in practical applications.

4.4.4. Expanding the Number of TX Beams

As the TX BF register of the probe can contain at most 9 TX profiles, the number of TX beams was limited. However, at the cost of a reduction in the PRF, more TX beams can also be used. For a single TX beam profile to be uploaded in the row-column mode (see Figure 2.3), 384 bits are required. While the ASIC in the probe can handle a higher bit-rate, the FPGA on the motherboard (see Figure 2.2) currently programs the ASIC at a bit-rate of 10 MHz, meaning that the upload of a new profile takes ∼40 µs. While this is less than one pulse-echo acquisition when uploading in parallel to RX, this is currently avoided as a precaution to ensure minimal supply noise in the ASICs. Given a 1540 m/s speed of sound in human tissue, one pulse-echo acquisition takes ∼130 µs when imaging a 10 cm depth. Adding this potential upload time per pulse-echo acquisition would result in a maximum PRF of ∼6 kHz, which depending on the application could still yield a sufficient volume-rate when more than 9 TX beams are desired.

Moreover, a higher PRF could be achieved by uploading during echo reception, although the impact of potential associated crosstalk to the RX signals has not been investigated yet. Given that not all applications require the high volume-rate that the probe was designed for, a potentially valuable expansion to the

results presented in this chapter could be an evaluation of the achievable imaging performance when the amount of pulse-echo acquisitions per volume are not as constrained.

4.4.5. Expanding the Array

As covered in Section 4.1, while the probe consists of 2 tiles, due to yield issues, no probe has been produced so far of which *both* tiles are fully functional in both RX *and* TX. While the evaluation of the imaging performance along the X-axis of one tile is indicative of the potential performance of the probe along both axes, a fully-functional probe is expected to provide an additional increase in SNR. As the full array can be used to transmit in the same region, rather than a 32×32 subsection (see Section 4.2.2), the SNR can increase by up to 12 dB. In addition, as the amount of elements in RX doubles, a further 3 dB improvement in SNR is expected, leading to a total increase in SNR up to 15 dB. The added SNR is not as critical for imaging static phantoms (see Figure 4.15), as the maximum voltage at which the probe can drive the transducers already lowers the noise below the clutter level. However, the benefit for flow imaging can be more substantial, as the SNR currently limits the accuracy of velocity estimations along the Y-axis of 1 tile.

4.5. Conclusion

In this chapter, a quantitative analysis of the imaging performance of a 32×64-element section of the developed AA probe has been presented. This analysis serves the goal of estimating the performance for the full 64×64-element array of the probe, and to find how well one of the two tiles in each probe performs by itself. In addition, multiple imaging schemes that can be pre-loaded into the probe have been compared to find how a modest increase in TX beams and the use of TDM affect image quality. Besides image quality, how well the schemes would perform for 3D Doppler imaging has also been evaluated.

While a small reduction in the PSF was observed for Scheme 2 versus Scheme 1/3, the improvement when increasing the amount of TX beams from 4 to 9 is modest, the largest being in elevation with a median decrease in the FWHM of 9%. Rather, the main benefit is an increased contrast at large imaging depths

from an improved SNR. However, as expected, this benefit comes at the price of aliasing at flow speeds typical for AAAs. Therefore, the use of more than 4 TX beams has limited overall benefits for the intended application.

When comparing Scheme 1 and 3, where TDM or multiplexing is applied, a small reduction in image quality with TDM due to induced artifacts was observed. The FWHM increases by 3-6%, and the contrast when imaging a hyperechoic cylinder reduced by <2.8 dB when assessing CR_{dB} and <0.4 when assessing CNR. However, these reductions in image quality are considered minor, whereas the added channel-count reduction that TDM provides without the need of multiplexing substantially improves accuracy when assessing flow imaging performance. The biggest difference was observed for flow along the X-axis of the array, where Doppler images using Scheme 3 suffer from aliasing.

Overall, the imaging performance with only 1 tile is promising for the high-volume-rate large-volume imaging that the probe was designed for. However, the penalty of not using the full array is a significant reduction in image quality along the Y-axis of the array. While future activities should focus on improving the yield of the array, such that the full 64×64-element array can be utilized, a probe variant containing only 1 tile is a promising intermediate solution for imaging of the AA.

References

[1] J. Provost et al., "3D ultrafast ultrasound imaging in vivo," *Physics in Medicine & Biology*, vol. 59, no. 19, p. L1, Sep. 2014. DOI: 10.1088/0031-9155/59/19/L1. [Online]. Available at: https://dx.doi.org/10.1088/0031-9155/59/19/L1.

[2] J. Voorneveld et al., "High-frame-rate contrast-enhanced ultrasound for velocimetry in the human abdominal aorta," *IEEE Transactions on Ultrasonics, Ferroelectrics, and Frequency Control*, vol. 65, no. 12, pp. 2245–2254, 2018. DOI: 10.1109/TUFFC.2018.2846416.

[3] J. Voorneveld et al., "4-D echo-particle image velocimetry in a left ventricular phantom," *Ultrasound in Medicine & Biology*, vol. 46, no. 3, pp. 805–817, 2020, ISSN: 0301-5629. DOI: https://doi.org/10.1016/j.ultrasmedbio.2019.11.020. [Online]. Available at: https://www.sciencedirect.com/science/article/pii/S0301562919316217.

[4] Y. M. Hopf et al., "A pitch-matched high-frame-rate ultrasound imaging ASIC for catheter-based 3-D probes," *IEEE Journal of Solid-State Circuits*, vol. 59, no. 2, pp. 476–491, 2024. DOI: 10.1109/JSSC.2023.3299749.

[5] P. Guo et al., "A 125 μ m-pitch-matched transceiver ASIC with micro-beamforming ADC and multi-level signaling for 3-D transfontanelle ultrasonography," *IEEE Journal of Solid-State Circuits*, pp. 1–14, 2024. DOI: 10.1109/JSSC.2024.3355854.

[6] Y. Igarashi et al., "Single-chip 3072-element-channel transceiver/128-subarray-channel 2-D array IC with analog RX and all-digital tx beamformer for echocardiography," *IEEE Journal of Solid-State Circuits*, vol. 54, no. 9, pp. 2555–2567, 2019. DOI: 10.1109/JSSC.2019.2921697.

[7] J. M. Rothberg et al., "Ultrasound-on-chip platform for medical imaging, analysis, and collective intelligence," *Proceedings of the National Academy of Sciences*, vol. 118, no. 27, e2019339118, 2021.

[8] R. Wodnicki, J. Zhang, Q. Zhou, J. Foiret, C. Notard, and K. W. Ferrara, "Electronically scanned large apertures for interventional and diagnostic liver," in *2023 IEEE International Ultrasonics Symposium (IUS)*, 2023, pp. 1–4. DOI: 10.1109/IUS51837.2023.10306431.

[9] R. Lopata, E. Maas, M. Thirugnanasambandam, E. van Disseldorp, and M. van Sambeek, "Ultrasound imaging for aortic biomechanics," in *Biomechanics of the Aorta*, Elsevier, 2024, pp. 139–162.

[10] R. Van Schaijk and M. Devices, "CMUT: a versatile and low cost ultrasonic platform," in *Micromachined Ultrasonic Transducers 2019*, Philips Innovation Serv., 2019. Accessed: Mar. 2, 2025. [Online]. Available at: https://www.salland.com/wp-content/uploads/2019/06/11-Rob-van-Schaijk-Philips-InS-MEMS-Seminar-2019.pdf.

[11] J. A. Jensen. "Field-II simulation program," Accessed: Mar. 2, 2025. [Online]. Available at: https://field-ii.dk/.

[12] L. W. Schmerr, *Fundamentals of Ultrasonic Phased Arrays*. Springer, 2015, pp. 20–24.

[13] P. Acoustics, *0.2 mm needle hydrophone (nh0200)*, English, Precision Acoustics, 8 pp. Accessed: Mar. 2, 2025. [Online]. Available at: https://www.acoustics.co.uk/wp-content/uploads/2022/03/NH0200-0.2mm-Needle-hydrophone-TDS-V1-0222.pdf.

[14] Most-Models. "AMMO MIG 8016 rigging - super fine 0,01mm - 2 meters kabel(s)," Accessed: May 6, 2025. [Online]. Available at: https://www.most-models.com/ammo-mig-8016-rigging-super-fine-0-01mm-2-meters-kabel-s--7789.

[15] CIRS Inc. "Multi-purpose, multi-tissue ultrasound phantom model 040GSE," Accessed: Mar. 2, 2025. [Online]. Available at: https://www.cirsinc.com/wp-content/uploads/2021/09/040GSE-DS-093021.pdf.

[16] Parker Laboratories Inc. "Aquaflex® Ultrasound Gel Pad," Accessed: May 11, 2025. [Online]. Available at: https://www.parkerlabs.com/products/aquaflex-ultrasound-gel-pad/.

[17] S. Smith, H. Lopez, and W. Bodine Jr, "Frequency independent ultrasound contrast-detail analysis," *Ultrasound in medicine & biology*, vol. 11, no. 3, pp. 467–477, 1985.

[18] H. Bendjador et al., "A theranostic 3d ultrasound imaging system for high resolution image-guided therapy," *Theranostics*, vol. 12, no. 11, p. 4949, 2022.

[19] M. Patterson and F. Foster, "The improvement and quantitative assessment of b-mode images produced by an annular array/cone hybrid," *Ultrasonic Imaging*, vol. 5, no. 3, pp. 195–213, 1983, ISSN: 0161-7346. DOI: https://doi.org/10.1016/0161-7346(83)90001-9. [Online]. Available at: https://www.sciencedirect.com/science/article/pii/0161734683900019.

[20] A. Rodriguez-Molares et al., "The generalized contrast-to-noise ratio: A formal definition for lesion detectability," *IEEE Transactions on Ultrasonics, Ferroelectrics, and Frequency Control*, vol. 67, no. 4, pp. 745–759, 2020. DOI: 10.1109/TUFFC.2019.2956855.

[21] CIRS Inc. "Doppler fluid," Accessed: May 6, 2025. [Online]. Available at: https://www.sunnuclear.com/uploads/documents/datasheets/769DF-DS-072220-1.pdf.

[22] Harvard Apparatus. "Standard Infuse/Withdraw PHD ULTRA™ Syringe Pumps," Accessed: May 6, 2025. [Online]. Available at: https://www.harvardapparatus.com/standard-infuse-withdraw-phd-ultra-syringe-pumps.html.

[23] CIRS Inc. "Peripheral vascular doppler flow phantom," Accessed: May 6, 2025. [Online]. Available at: https://www.sunnuclear.com/uploads/documents/datasheets/ATS524Phantom_0080822.pdf.

[24] T. L. Szabo and P. Kaczkowski, *Essentials of Ultrasound Imaging*. Elsevier, 2023.

[25] J. A. Jensen, "A model for the propagation and scattering of ultrasound in tissue," *The Journal of the Acoustical Society of America*, vol. 89, no. 1, pp. 182–190, 1991.

[26] K. H. Fraser, S. Meagher, J. R. Blake, W. J. Easson, and P. R. Hoskins, "Characterization of an abdominal aortic velocity waveform in patients with abdominal aortic aneurysm," *Ultrasound in Medicine & Biology*, vol. 34, no. 1, pp. 73–80, 2008, ISSN: 0301-5629. DOI: https://doi.org/10.1016/j.ultrasmedbio.2007.06.015. [Online]. Available at: https://www.sciencedirect.com/science/article/pii/S030156290700316X.

[27] Y. A. Algabri, O. Altwijri, and S. Chatpun, "Visualization of blood flow in aaa patient-specific geometry: 3-d reconstruction and simulation procedures," *Bionanoscience*, vol. 9, no. 4, pp. 966–976, 2019.

[28] B. M. Fadel et al., "Ultrasound imaging of the abdominal aorta: A comprehensive review," *Journal of the American Society of Echocardiography*, vol. 34, no. 11, pp. 1119–1136, 2021.

5

Conclusion

In this dissertation, the design, fabrication and evaluation of a high-volume-rate ultrasound probe for imaging large volumes, primarily abdominal aortic aneurysms, has been presented. In this chapter, the main contributions and general findings are summarized. In addition, recommendations for future activities to further develop the probe and for ultrasound systems in general are given.

5.1. Main Contributions

Chapter 2

An ultrasound probe has been presented which is the first to scale the combination of micro-beamforming and time-division multiplexing (TDM) to thousands of elements (4096) by means of in-probe application-specific integrated circuits (ASICs). It is capable of imaging a volume of 60°×60°×10 cm at a state-of-the-art volume-rate of 2000 volumes/s, demonstrating the scalability and efficacy of this channel-count reduction strategy. Moreover, the probe also contains a novel transmit beamformer (TX BF) that can steer arbitrary pulse-density modulated (PDM) waveforms, implemented as a programmable digital pipeline that treats its binary input as a sampled PDM signal. This significantly simplifies the implementation compared to the prior art [1], while retaining a very high degree of

flexibility in waveform definition. The performance of the probe has been evaluated in electrical, acoustical and imaging experiments.

Chapter 3
The ASICs in the ultrasound probe, presented in Chapter 2, have been used to do a systematic comparison between two different ultrasound transducer technologies. An overview of the design trade-offs for the ASIC and packaging design have been presented to make the probe compatible with both a bulk-fabricated piezoelectric transducer and capacitive micromachined ultrasound transducer (CMUT) technology. Two prototype variants have been produced and acoustically verified, demonstrating the potential of using the probe as a prototyping platform for further research activities, where validation of ultrasound arrays of up to thousands of elements can be done.

Chapter 4
Using the probe presented in Chapter 2 and the array characterization in Chapter 3, the imaging performance of one 32×64-element tile in the probe has been quantified. This includes an imaging scheme for achieving the peak volume-rate of 2000 volumes/s, as well as imaging schemes that trade off volume-rate for resolution and contrast by increasing the amount of pulse-echo repetitions per volume. The imaging performance characterization included a detailed quantification of resolution within the full field of interest, of achievable contrast and of Doppler performance when imaging high flow rates. Together, these results showcase the imaging capabilities of one tile and provide an indication of the expected performance of the full 64×64-element probe.

5.2. General Findings

The following items summarize the main findings during the development of the probe presented in this dissertation:

- An effective and scalable method of in-probe channel-count reduction is a combination of maximizing the utilization of the available bandwidth per output RX channel and exploiting the characteristics of the incoming ultrasound signals. As such, combining TDM and micro-beamforming is an effective method of maximizing the amount of channel-count reduction at

minimal cost. (Chapter 2)

- PDM modulating TX waves enables the use of highly flexible and relatively simple-to-implement TX BF architectures, as signals can directly be represented as bit-sequences without the need of decoding. For instance, the TX BF design for the probe presented in this dissertation is implemented as a programmable pipeline of D-flip-flops (DFFs), which is simple yet highly flexible. (Chapter 2)

- While monolithic integration of CMUT arrays with ASICs requires careful circuit and layout design, it is a highly scalable and well performing technology for ultrasound imaging, and is therefore very well suited for active imaging probes with thousands of elements. (Chapters 2, 3 & 4)

- While equalization is effective for reducing TDM-induced crosstalk, the overall effect on image quality is modest if the imaging array is sufficiently large. This is likely caused by the coherent compounding of the signal contents of each sub-aperture (SAP) when beamforming, while artifacts not being compounded coherently are thus suppressed. (Chapters 2 & 4)

- Probe yield becomes a significant fabrication challenge once active probes are scaled to arrays with thousands of elements. As different fabrication steps affect it, an effective intermediate screening procedure may prove critical when scaling fabrication of such ultrasound probes. This could involve pre-sorting dies on wafers with micro-fabricated ultrasound transducers and sorting the bonded ASICs with ultrasound array before further packaging based on an electrical evaluation. (Chapters 3)

- The main challenges in the design of ASICs for high volume-rate (HVR) ultrasound imaging are power consumption and power distribution, circuit area, and channel management. The first is mainly restricted by the sharp limit on temperature rise, which in turn is limited by the amount of heat that the packaging of a probe can sink. The second is mainly restricted by a finite supply impedance, both inside the ASICs and the electronics they interface with. The last two relate to managing the finite area per channel and limited cable count and bandwidth of each receive (RX) channel. (Chapter 2)

- An effective power distribution strategy in ultrasound ASICs with large arrays is to minimize the size of high-frequency loops as much as possible.

Typically this involves a multi-tiered approach, where there is a form of regulation at each supply at the sub-array-level, array-level, and packaging-level. These can be as simple as appropriately sized supply traces and decoupling capacitors, and more complex active regulation. As a result, power management design can not be done after-the-fact and must be co-designed with the load it is meant to supply. In this design, all supplies are stabilized by capacitive decoupling within the ASIC. Most supplies are also stabilized by capacitive decoupling at the packaging-level, but active regulation is used for the low-voltage (LV) analog supplies, which draw a large current relative to the other supplies. (Chapters 2 & 3)

- When the amount of in-probe channel-count reduction is limited, for active arrays consisting of thousands of elements, the ASIC's pad design and trace routing on the printed circuit board (PCB) to which the ASICs are bonded should be taken into account at an early stage in the project to avoid fabrication issues after the ASIC is finished. As such, fixing the amount of signal and power supply connections and designing the PCB trace routing was one of the early design activities for the probe in this work. (Chapters 2 & 3)

- As transducer arrays and their supplies are not well modeled in computer-aided design (CAD) tools, sufficient margin should be budgeted when designing and scaling interfacing circuits with these devices. Moreover, as most transducers have a ground that is not supplied from the ASIC they interface with, their integration must be considered from a system perspective, i.e. also taking into account the PCB on which the ASICs are mounted, and potentially also the supplies provided to the PCB. While difficult to validate its necessity in practice, this conservative design approach was applied to ensure that the probe presented in this work functions as intended. (Chapters 2 & 3)

- When designing a transducer array, it is important to take into account acoustical crosstalk between transducer elements, as this narrows their field of view. While an array that is sufficiently large may still produce beamformed images that have a sufficient signal-to-noise ratio (SNR) at large viewing angles, the effect on system-level imaging performance has to be taken into account, such as in the definition of the dynamic range of the probe. (Chapters 3 & 4)

- To avoid latch-up like behaviors and excessive substrate noise, strategic segmentation of supplies, the placement of isolation wells around all major circuit blocks, and ensuring sufficient spacing for guard rings have proven an effective strategy as the ultrasound ASICs in probes scale to accommodate thousands of elements.

5.3. Future Work

5.3.1. Near-term Improvements of the Imaging System

By 'near-term improvements', improvements are meant that do not require the ASIC described in Chapter 2 to change except for minor revisions that could be achieved with a metal mask change, in order to produce an improved version of the probe prototypes presented in this dissertation.

Achieving Further Channel-count Reduction (Analog)

The design presented in Chapter 2 only applies 2× TDM due to bandwidth limitations of the system back-end (Verasonics Vantage-256 (VSX) [2]). However, this is not a fundamental limitation, as demonstrated in [3]. Moreover, while 512 cables is a workable number (Chapter 2), it is not ideal, as cables form a significant part of the cost of an ultrasound probe in addition to requiring multiple of the most popular back-end systems [2], [4] to operate at peak capacity, further increasing cost. To further reduce channel-count, there are a few viable options that can be considered.

The most simple, but potentially restrictive solution would be to redesign the motherboard that connects to the imaging systems, or to design an add-on board that implements 2× multiplexing. As this only requires an array of off-the-shelf multiplexing chips, it is a cheap method of reducing the amount of system back-ends from two to one, while still being able to interface with all SAPs in a probe. However, this comes at the price of a 2× reduced volume rate, making the probe less suitable for tracking high flow rates, as demonstrated in Chapter 4.

An alternative, yet more demanding solution, would be to introduce a companion chip in the probe that implements an additional n× TDM to further reduce channel-count at the cost of increased bandwidth requirements per output channel. While this precludes the use of most conventional system back-ends, newer

systems have increased bandwidth [5], which the probe would still be compatible with. Moreover, this companion chip could still include a multiplexing option to offer compatibility with conventional systems at reduced performance. Alternatively a back-end could be custom built, in which case channel bandwidth becomes a design parameter, although this might cause issues with adoption.

Rather than increasing bandwidth, the aforementioned companion chip could also make more efficient use of the bandwidth available. A typical ultrasound transducer, including those compared in Chapter 3, has a bandwidth of $\leq$100% around its center frequency. As such, by IQ demodulating (and down-sampling) the RX signals, which is a well known technique for ultrasound signal processing [1], [6], [7], more TDM can be realized at the same overall bandwidth. For the design presented in Chapter 2, each SAP produces a $\sim$10 MHz sampled-and-held output of a $\sim$2.4 MHz bandwidth signal. By IQ-demodulating this signal, a $\sim$1.2 MHz bandwidth in-phase and quadrature signal are generated, which can each be sampled at a 4$\times$ lower frequency. To utilize the same $\sim$20 MHz bandwidth as the probe currently does, 8$\times$ TDM can be applied to modulate 4 IQ-pairs on a single output RX channel, achieving an additional 2$\times$ channel-count reduction over the current design, and reducing the amount of required system back-ends to one. However, this solution requires a suitable anti-aliasing filter before down-sampling to avoid excessive noise folding.

Achieving Further Channel-count Reduction (Digital)

As aforementioned, a companion chip to the design presented in Chapter 2 offers multiple options for reducing channel-count in the analog domain. However, further channel-count reduction is possible with in-probe digitization via digital TDM (D-TDM) without a crosstalk penalty such as with analog TDM. Moreover, while an ultrasound front-end is typically fabricated in a process suitable for implementing high-voltage (HV) transmitters to increase roundtrip SNR [1], [3], [8], [9], [10], the LV transistors in such nodes typically are much larger than processes containing only LV devices can achieve. As such, a companion chip is not limited to the same 180-nm LV devices that the design presented in Chapter 2 is.

Therefore, while the analog-to-digital converters (ADCs) required for in-probe digitization come at the cost of additional in-probe power dissipation, this may be offset to some extent by a potential reduction in power for data transmission with a proper choice of process node. This reduction in power can either be in the form of a more power-efficient data-link, and/or in-probe RX data pre-processing, which is

more easily achieved in the digital domain than in the analog domain. However, it should be noted that the aforementioned solutions require a custom system back-end to process the digitized data-stream from the probe. While overall system performance would likely improve, it might also introduce a barrier for adoption by users that currently use conventional ultrasound systems.

Reducing the Form-factor of the Probe

The prototype probe(s) presented in this dissertation were designed to have a form factor that is mainly suitable for research measurement setups and is usable for potentially measuring real AAs. However, for most applications, the large front-side dimensions are undesirable, as it makes manipulating the probe more difficult and it also increases difficulty when trying to image where bone blocks the region of interest, such as around the ribcage or cranium. To reduce the front-side form factor, the PCB on which the ASICs in the probe are mounted could be made rigid-flex [11]. This would allow regions on the PCB that mainly consist of routing traces and low-frequency power regulation to be mounted perpendicular to the probe's front side. Alternatively, the ASICs could be mounted on a rigid board that has mounting points for the assembly of additional perpendicular rigid PCBs.

Improving the Yield of the Probe

As briefly discussed throughout this dissertation, managing device yield has been a persistent challenge to overcome. The main challenges that were faced so far have been bonding yield and transducer yield. As bonding was done in a flexible research & development (R&D) environment, its process is not as tightly controlled as in a dedicated commercial setting. In addition, each probe requires more than a thousand bonds to be faultless. In practice, this resulted in a tile yield of ∼50-70%, meaning that only 1-in-3 to 1-in-4 probes would have two fully bonded tiles without any shorts. By using a better controlled process, this yield is expected to improve. Alternatively, the ASICs could be flip-chipped on an interposer with an opening for the array, avoiding the bonding process altogether.

Regarding the transducer yield, while a small amount of faulty elements do not affect the performance of the probe significantly, depending on the type of transducer, they can damage the underlying ASIC during and/or after their fabrication. For the probe variant with CMUTs (see Chapters 2 and 4), when a faulty CMUT shorts as its bias voltage is applied, the bias line discharges into an underlying

pulser in the ASIC, damaging its HV devices and either causing a latch-up like event, or reducing the maximum TX voltage they can withstand. To avoid integrating tiles with such faulty elements into probes, the fabrication process would benefit from a wafer-level screening process where the CMUTs are pre-validated, such as described in [12].

5.3.2. Long-term Improvements of the Imaging System

By 'long-term improvements', improvements are meant that could involve a complete revision of the probe(s) presented in this dissertation, including any ASICs it may contain.

Improving the Tileability of the Probe

As shown in Figure 2.1(b), each tile in the probe is bonded from three sides for ease of fabrication. The LV bond pads on the long side of a tile are a dense staggered array, while the HV bond pads on the top and bottom of the tile are widely spaced single rows. As shown in Figure 3.6(c,d), the layout eases routing complexity and allows the PCB on which the tiles are bonded to be fabricated in a standard process (with the exception of trace spacing and thickness) [13]. However, this solution only allows the pitch-matched tiling of two arrays. By adopting a more complex triple- or quad- staggered array, all pads could be fitted on one side of each ASIC, allowing additional pitch-matched tiling along the Y-axis of the probe, further increasing the array size if applications require it. However, this would require the design of a more complex and non-standard PCB, increasing fabrication costs and potentially decreasing yield.

Dynamic Scaling of the Probe Front-end

As shown in Section 3.3.2, the transducer, and by derivative the load of the interfacing front-end, has a non-negligible process spread. While this spread is deemed acceptable for imaging purposes, in a future design iteration, integrating a calibration option such as measuring C_e (see Figure 3.2(a)) by integrating a voltage on the transducers via a direct-current (DC) current source at the input would offer a simple method of further reducing it. Moreover, R_m can also be estimated with a second measurement where a current at f_c is injected.

As covered in Section 3.2.3, the front-end was scaled to handle a widely ranging

transducer input impedance. However, this came at the cost of power efficiency when a load is relatively modest. With C_e and R_m known, the gain can be trimmed to compensate transducer spread, but the g_m of the low-noise variable-gain amplifiers (VGAs) in the probe's ASICs can also be trimmed for a sufficient gain-bandwidth given their load. This would potentially (depending on the transducer) result in an improved power efficiency, while retaining a high degree of compatibility with a range of transducer technologies.

Improving the Transmit Beamformer

Section 2.2.2 describes the current implementation of the in-probe TX BF, which can delay an arbitrary PDM waveform across the array. However, a limitation is that this waveform is the same for all elements. This precludes TX apodization for reducing side-lobe levels [14] and/or transmitting multiple encoded TX beams in parallel, such as done in [15]. Therefore, a potential improvement to the probe could be to encode multiple TX waveforms in the arbitrary bit-sequence that is delayed across the array, similar as described in [1], where the beam of interest would be locally decoded an transmitted. Moreover, delay information can also be encoded in the same way by simply adding zeros to a sequence.

As such, an alternative architecture to the one described in Section 2.2.2 could be a TX beamformer where a signal is transferred via a data bus to all elements in the array instead. The signal would contain encoded delayed TX waveforms, where each element would pass the signal on the bus through a look-up table, decoding matrix, or digital filter to reconstruct when and what waveform to transmit (TX). While this could partially involve operating the data-bus at a higher clock rate than the TX BF described in Section 2.2.2, the redundancy that it introduces by allowing any bit-sequence also means that multiple waveforms could already be encoded at the same data rate.

Pulser Integration & Size Constraints

While not as big of a design constraint for the design in this dissertation as others [8], [9], [16], [17], a significant part of the available per-element area is consumed by the double-diffused metal-oxide semiconductor (DMOS) transistors in the pulsers that produce the HV waveforms to actuate the transducer array. In the bipolar-CMOS-DMOS (BCD) technology that was used, HV regions are isolated by reverse-biased PN junctions with a large lateral area. Alternatively, a silicon-

on-insulator (SOI) technology could be used, which uses an oxide layer for isolation [18]. This allows the lateral footprint of (HV) DMOS transistors in an SOI technology to decrease, allowing the pulsers to decrease in size. Alternatively, the TX voltage could be increased [10], [19], or multi-level pulsers could be implemented instead for added power efficiency and/or pulse-inversion [10], [20]. Conversely, the size of the pulser circuit can also be reduced by lowering its maximum TX voltage. While this would lower the roundtrip dynamic range of the probe for the same transducer, innovations in LV transducer technologies such as LV CMUTs allow for the same roundtrip dynamic range to be maintained.

References

[1] J. M. Rothberg et al., "Ultrasound-on-chip platform for medical imaging, analysis, and collective intelligence," *Proceedings of the National Academy of Sciences*, vol. 118, no. 27, e2019339118, 2021.

[2] Verasonics, *Vantage specifications for biomedical & general applications*, English, Verasonics, 2024, 4 pp., February, 2024.

[3] A. Rezvanitabar et al., "Integrated hybrid sub-aperture beamforming and time-division multiplexing for massive readout in ultrasound imaging," *IEEE Transactions on Biomedical Circuits and Systems*, vol. 16, no. 5, pp. 972–980, 2022. DOI: 10.1109/TBCAS.2022.3205024.

[4] E. Boni et al., "ULA-OP 256: A 256-channel open scanner for development and real-time implementation of new ultrasound methods," *IEEE Transactions on Ultrasonics, Ferroelectrics, and Frequency Control*, vol. 63, no. 10, pp. 1488–1495, 2016. DOI: 10.1109/TUFFC.2016.2566920.

[5] Verasonics, *Vantage NXT brochure and specifications*, English, Verasonics, 2024, 7 pp., January, 2024.

[6] S. Bae, H. Song, and T.-K. Song, "Analysis of the time and phase delay resolutions in ultrasound baseband i/q beamformers," *IEEE Transactions on Biomedical Engineering*, vol. 68, no. 5, pp. 1690–1701, 2021. DOI: 10.1109/TBME.2020.3019799.

[7] M. Liu, Z. Kou, Y. Zhao, J. W. Wiskin, G. J. Czarnota, and M. L. Oelze, "Spectral-based quantitative ultrasound imaging processing techniques: Com-

parisons of rf versus iq approaches," *Ultrasonic imaging*, vol. 46, no. 2, pp. 75–89, 2024.

[8] Y. M. Hopf et al., "A pitch-matched high-frame-rate ultrasound imaging ASIC for catheter-based 3-D probes," *IEEE Journal of Solid-State Circuits*, vol. 59, no. 2, pp. 476–491, 2024. DOI: 10.1109/JSSC.2023.3299749.

[9] P. Guo et al., "A 125 μ m-pitch-matched transceiver ASIC with micro-beamforming ADC and multi-level signaling for 3-D transfontanelle ultrasonography," *IEEE Journal of Solid-State Circuits*, pp. 1–14, 2024. DOI: 10.1109/JSSC.2024.3355854.

[10] Y. Igarashi et al., "Single-chip 3072-element-channel transceiver/128-subarray-channel 2-D array IC with analog RX and all-digital tx beamformer for echocardiography," *IEEE Journal of Solid-State Circuits*, vol. 54, no. 9, pp. 2555–2567, 2019. DOI: 10.1109/JSSC.2019.2921697.

[11] Multi-CB. "Rigid-Flex PCBs," Accessed: May 16, 2025. [Online]. Available at: https://www.multi-circuit-boards.eu/en/products/printed-circuit-boards/rigid-flex-pcb.html.

[12] M. U. Khan, M. La Mura, M. Saccher, R. van Schaijk, R. Dekker, and A. S. Savoia, "Fast and accurate estimation of collapse and snapback voltages of cmuts," in *2024 IEEE Ultrasonics, Ferroelectrics, and Frequency Control Joint Symposium (UFFC-JS)*, 2024, pp. 1–4. DOI: 10.1109/UFFC-JS60046.2024.10793933.

[13] Multi-CB. "Basic Design Rules," Accessed: May 19, 2025. [Online]. Available at: https://www.multi-circuit-boards.eu/fileadmin/user_upload/downloads/leiterplatten_design-hilfe/Multi-CB-Leiterplatten_Basic-Design-Rules_en.pdf.

[14] T. L. Szabo and P. Kaczkowski, *Essentials of Ultrasound Imaging*. Elsevier, 2023.

[15] Y. Saito and N. Tagawa, "One-shot beam-forming with adaptively weighted compound of multiple transmission angles and subbands," *Japanese Journal of Applied Physics*, vol. 61, no. SG, SG1079, 2022.

[16] Y. M. Hopf et al., "A pitch-matched transceiver ASIC with shared hybrid beamforming ADC for high-frame-rate 3-D intracardiac echocardiography," *IEEE Journal of Solid-State Circuits*, vol. 57, no. 11, pp. 3228–3242, 2022. DOI: 10.1109/JSSC.2022.3201758.

[17] P. Guo et al., "A 1.2-mW/channel pitch-matched transceiver ASIC employing a boxcar-integration-based rx micro-beamformer for high-resolution 3-D ultrasound imaging," *IEEE Journal of Solid-State Circuits*, vol. 58, no. 9, pp. 2607–2618, 2023. DOI: 10.1109/JSSC.2023.3271270.

[18] P. Wessels et al., "Advanced bcd technology for automotive, audio and power applications," *Solid-State Electronics*, vol. 51, no. 2, pp. 195–211, 2007, Special Issue: Papers Selected from the EUROSOI'06 Conference, ISSN: 0038-1101. DOI: https://doi.org/10.1016/j.sse.2007.01.019. [Online]. Available at: https://www.sciencedirect.com/science/article/pii/S0038110107000056.

[19] L. Novaresi et al., "A pmut transceiver front-end with 100-v tx driver and low-noise voltage amplifier in bcd-soi technology," in *ESSCIRC 2022- IEEE 48th European Solid State Circuits Conference (ESSCIRC)*, 2022, pp. 221–224. DOI: 10.1109/ESSCIRC55480.2022.9911390.

[20] K. Chen, H.-S. Lee, A. P. Chandrakasan, and C. G. Sodini, "Ultrasonic imaging transceiver design for cmut: A three-level 30-vpp pulse-shaping pulser with improved efficiency and a noise-optimized receiver," *IEEE Journal of Solid-State Circuits*, vol. 48, no. 11, pp. 2734–2745, 2013. DOI: 10.1109/JSSC.2013.2274895.

A

Appendix

A.1. Analysis of the Maximum Field-of-View per Pulse-Echo Acquisition

In Chapter 4 Section 4.2.2 it was mentioned that the TX beams were dimensioned to avoid illuminating grating lobes. Moreover, as covered multiple times in this dissertation, the maximum FoV that can be imaged per acquisition is 30°×30°. This section provides a brief overview on the analysis to justify this, which is based on the two-way beam profile analysis in [1].

Figure A.1 shows the two-way beam profile of one of the pulse-echo acquisitions covered in Section 4.2.2, simulated in Field-II [2]. A TX beam with a 30°×30° opening angle and -15°×-15° steering angle is used. The SAP steering angle is also -15°×-15° and the system beamformer focal point was varied between 0°×0° and -40°×-40° at a 4.1 cm distance from the array. As indicated, when beamforming the RX data, to keep grating lobe levels at least 20 dB lower than the focal point, the FoV per acquisition is constrained to 30°×30°, which is also the reason that the TX beams are constrained to the same width. As a result, at least 4 acquisitions are required to reconstruct the 60°×60° field of interest, as covered in this dissertation.

A

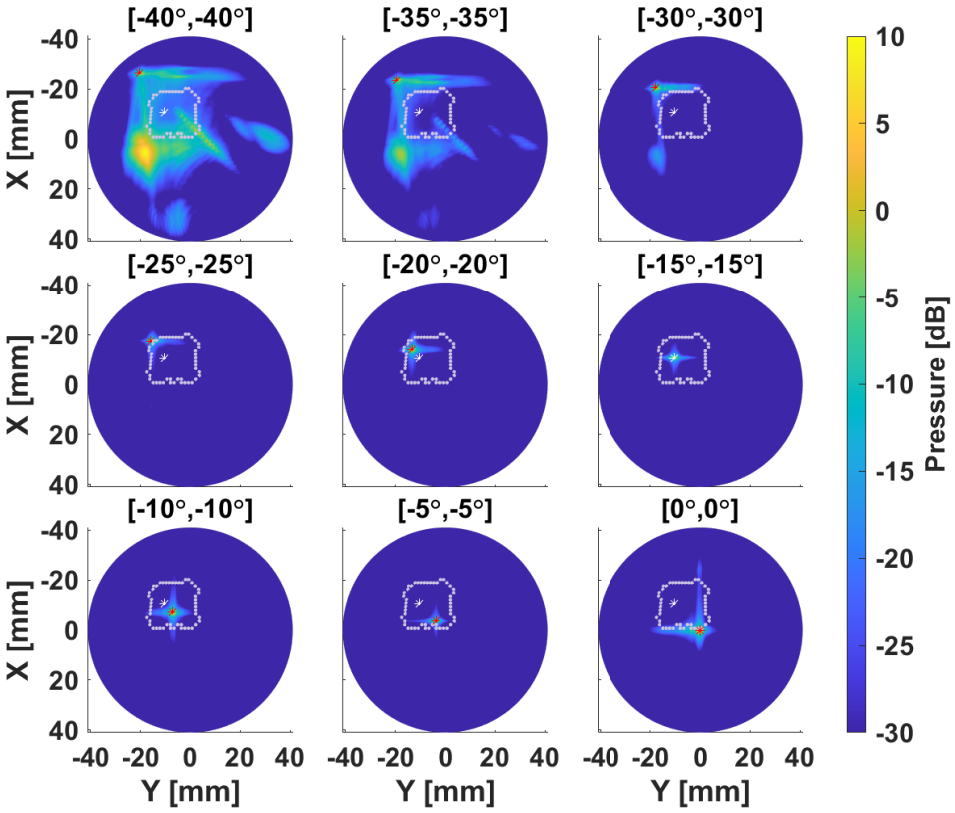

Figure A.1: Two-way directivity, normalized at the system beamformer focal point, evaluated at the boundaries of a sphere at 4.1 cm from the center of the probe (see Figure 4.2). The SAP steering angle is -15°×-15° , as indicated by the white markers. The system beamformer focus is varied between 0°×0° and -40°×-40°, as indicated by the red marker. The -6dB-boundary of the normalized TX beam pressure crossing the boundaries of the sphere is highlighted by the dotted purple line.

References

[1] P. Santos, G. U. Haugen, L. Løvstakken, E. Samset, and J. D'hooge, "Diverging wave volumetric imaging using subaperture beamforming," *IEEE Transactions on Ultrasonics, Ferroelectrics, and Frequency Control*, vol. 63, no. 12, pp. 2114–2124, 2016. DOI: 10.1109/TUFFC.2016.2616172.

[2] J. A. Jensen. "Field-II simulation program," Accessed: Mar. 2, 2025. [Online]. Available at: https://field-ii.dk/.

Summary

This dissertation covers the design, fabrication, and application of an ultrasound probe that can image a large (60°×60°×10 cm) volume at a very high (2000 vol/s) volume-rate to facilitate modern imaging techniques such as 3-dimensional (3D) flow and elastography, mainly for improved imaging of abdominal aortic aneurysms (AAAs). To achieve these goals, the probe needs a large aperture consisting of a dense 2-dimensional (2D) array of transducers to achieve the desired resolution and contrast, the resulting element count calls for in-probe channel-count reduction. Moreover, the potential initial users of such a probe are ultrasound researchers, which also require a high flexibility in how the probe can be operated. To meet these requirements, tileable application-specific integrated circuits (ASICs) have been developed which can directly interface with an imaging array of 4096 elements. Multiple prototypes have been fabricated and evaluated. This dissertation provides a detailed description of the design and evaluation of the ASICs, how they are integrated with different transducer technologies, and how they are packaged into usable prototypes. Moreover, a detailed description is given on how they perform for their intended application based on acoustic measurements. In the following, the individual chapters of the dissertation are summarized.

Chapter 1
This chapter covers the motivation and background of this work. It starts with a description of why improved diagnosis and risk assessment is necessary for improved treatment of AAAs, and how this benefits society. This is followed by a description of why ultrasound imaging is currently used for diagnosis and how these systems operate. The trade-off between frame-rate and resolution is then explained, leading to the main challenge associated with modern imaging schemes, which require both a high frame-rate, resolution, and imaging volume. To address this challenge, the probe that is covered in this dissertation is presented as a solution, together with the main requirements it should meet. Lastly, an outline of the remainder of the dissertation is given.

Chapter 2

This chapter covers the design of an ultrasound probe that can image a 60°×60°×10 cm volume at 2000 vol/s, mostly focusing on the ASIC and system electronics design. First, an overview is given of its architecture. The ASIC achieves 8× receive (RX) channel-count reduction with 4× delay-and-sum micro-beamformers (µBFs), of which two outputs are combined with 2× time-division multiplexing (TDM). An automatic calibration function trains equalizers (EQs) to reduce the associated TDM-induced crosstalk by 10 dB. In addition, the ASIC contains a novel transmit (TX) beamformer (BF) that operates as a programmable digital pipeline that steers arbitrary pulse-density modulated (PDM) waveforms to 65 V unipolar pulsers that drive a monolithically-integrated 365 µm pitch 32×64-element capacitive micromachined ultrasound transducer (CMUT) array. Two ASIC tiles are packaged into the 64×64-element probe prototype, which interfaces with two custom motherboards that connect to 2 Verasonics Vantage-256 (VSX) imaging systems. Electrical validation of the ASICs, which were produced in a TSMC 0.18 µm HV BCD technology, and acoustic validation of the packaged prototype demonstrate the performance of the system.

Chapter 3

This Chapter covers the design, fabrication process, and evaluation of two different ultrasound transducer arrays that were fabricated on two variants of the ultrasound probe which was covered in the previous chapter. One variant contains a 2.6 MHz CMUT array (Xiver, The Netherlands), and the other contains a 2.6 MHz in-house bulk-fabricated piezo-electric transducer array. First, the manufacturing flow for both probe variants are presented, followed by circuit and layout design trade-offs in the probe to be compatible with both transducer technologies. The packaging of both probe variants are then covered in detail. This is followed by the measurement setups for characterizing both transducer arrays in RX and TX. The CMUT array has a mean TX efficiency of 12.2 kPa/V with a 1.9-dB standard deviation and a mean RX efficiency of 0.93 nA/Pa with a 2.0-dB standard deviation. Due to fabrication issues, the piezo-electric transducer array could only be evaluated in RX, and has a mean efficiency of 2.5 nA/Pa. The directivity of both devices is more narrow than simulations predict, likely because crosstalk is not accurately modeled. Despite fabrication issues, the chapter demonstrates that the developed system can serve as a useful measurement platform for systematic evaluation of different transducer arrays.

Chapter 4

This chapter covers an evaluation of the imaging performance of one 32×64-element tile in the probe with integrated CMUT array, which was covered in the previous chapters. Multiple imaging schemes were compared that use a (sub)set of 9 diverging TX beams to cover the 60°×60°×10 cm volume of interest. To evaluate the schemes, a custom 3D wire phantom was made to estimate the point-spread-function (PSF) across the full volume. In addition contrast was measured via a CIRS 040GSE phantom and the 3D Doppler performance was evaluated by imaging blood mimicking fluid being pumped through a 4 mm tube in a CIRS ATS524 flow phantom. It was found that TDM-induced crosstalk does not have a significant affect on image quality. In addition, an imaging scheme requiring 4 pulse-echo acquisitions per volume is capable of tracking flow speeds that can be expected in AAAs (0.4 m/s), while retaining a sufficient resolution. However, the image contrast in anechoic regions using this scheme is lower than expected. While this contrast improves when using an imaging scheme that reconstructs volumes with 9 pulse-echo acquisitions, this comes at the cost of being able to track desired flow speeds.

Chapter 5

This chapter concludes the dissertation and provides an overview of the achievements. Multiple original contributions were made. One of the most important is that the presented probe scales an effective channel-count reduction strategy of micro-beamforming and TDM to an array of thousands of elements. Another main contribution is the TX beamformer in the probe, which achieves a high flexibility in TX waveform definition while being relatively simple to implement. Furthermore, the probe is also one of the first to monolithically integrate a CMUT array with thousands of elements on ASICs. The chapter also provides an outlook on future improvements to the developed system, both in the short and long term. The most important of which are means of further channel-count reduction.

Samenvatting

Dit proefschrift behandeld het ontwerp, de fabricatie, en de toepassing van een ultrageluid-probe die een groot (60°×60°×10 cm) volume kan beeldvormen met een zeer hoge snelheid (2000 vol/s) om moderne beeldvormingstechnieken zoals 3-dimensionale (3D) flow en elastografie te faciliteren, voornamelijk voor verbeterde beeldvorming van abdominale aorta-aneurysma's (AAA's). Om deze doelen te bereiken, heeft de probe een grote apertuur nodig die bestaat uit een dense 2-dimensionale (2D) matrix van transducers om de gewenste resolutie en contrast te behouden, wat als gevolg kanaalreductie binnen de probe vereist. Bovendien, aangezien de initiele gebruikers van deze probe ultrageluid onderzoekers zijn, is ook een hoge flexibiliteit in hoe de probe gebruikt kan worden noodzakelijk. Om aan deze eisen te voldoen, zijn betegelbare applicatie-specifieke geintegreerde schakelingen (ASICs) ontwikkeld, die direct kunnen interfaceren met een beeldvormingsmatrix met 4096 elementen. Meerdere beeldvormingsmatrices met ASICs zijn geintegreerd in prototypes voor de beoogde gebruikers en getest. Dit proefschrift geeft een gedetaileerde beschrijving van het ontwerp en de evaluatie van de ASICs, hoe ze geintegreerd zijn met verschillende transducer technologieën, en hoe ze in bruikbare prototypes zijn geïntegreerd. Bovendien wordt aan de hand van akoestische metingen een gedetailleerde omschrijving gegeven hoe goed ze voor de beoogde applicatie zullen werken. In de rest van deze samenvatting zullen de individuele hoofdstukken in dit proefschrift samengevat worden.

Hoofdstuk 1

Dit hoofdstuk behandelt de motivatie en achtergrond van dit werk. Het begint met een beschrijving van de redenen waarom verbeterde diagnose en risicoanalyse noodzakelijk zijn om AAA's beter te kunnen behandelen, en waarom dit waardevol is voor de samenleving. Vervolgens wordt beschreven waarom echografie momenteel wordt gebruikt voor diagnose en hoe echografiesystemen werken. Daarna wordt de afweging tussen beeldsnelheid en resolutie uitgelegd, wat leidt tot de hoofduitdaging die geassocieerd is met moderne beeldvormingstechnieken, die zowel een hoge beeldsnelheid als resolutie vereisen. Om deze uitdaging aan te pakken, wordt de probe die in dit proefschrift beschreven wordt, gepresenteerd, samen met de eisen

waaraan deze moet voldoen. Tot slot wordt een overzicht gegeven van de rest van het proefschrift.

Hoofdstuk 2

Dit hoofdstuk behandelt het ontwerp van een echoprobe die een volume van 60°×60°×10 cm kan beeldvormen met een snelheid van 2000 vol/s, waarbij vooral de focus ligt op het ASIC- en systeemelektronica-ontwerp. Eerst wordt een overzicht gegeven van de systeem architectuur. De ASIC reduceerd de ontvangst (RX) kanalen met 8× middels 4× delay-and-sum micro-beamformers (µBFs), waarvan twee uitgangen worden gecombineerd met 2× time-division multiplexing (TDM). Een automatische kalibratiefunctie traint equalizers (EQs) om de bijbehorende TDM-geïnduceerde overspraak met 10 dB te verminderen. Daarnaast bevat de ASIC een nieuwe zend (TX) beamformer (BF) die functioneert als een programmeerbare digitale pijplijn die willekeurige pulsdichtheid gemoduleerde (PDM) golfvormen stuurt naar 65 V unipolaire pulsers die een monolithisch geïntegreerde 365 µm pitch 32×64-element capacitieve microgefabriceerde echotransducer (CMUT) matrix aansturen. Twee ASIC-tegels zijn verpakt in een probe-prototype met 64×64 elementen, die interfaceert met 2 op maat gemaakte moederborden die verbinding maken met 2 Verasonics Vantage-256 (VSX) beeldvormingssystemen. Elektrische validatie van de ASICs, die geproduceerd zijn in een TSMC 0,18 µm HV BCD technologie, en akoestische validatie van het verpakte prototype demonstreren de prestaties van het systeem.

Hoofdstuk 3

Dit hoofdstuk behandelt het ontwerp, het fabricageproces en de evaluatie van twee verschillende echotransducermatrices die zijn gefabriceerd op twee varianten van de echoprobe die in het vorige hoofdstuk is beschreven. Een variant bevat een 2,6 MHz CMUT-matrix (Xiver, Nederland), en de andere bevat een 2,6 MHz inhouse bulk-gefabriceerde piëzo-elektrische transducermatrix. Eerst wordt het fabricageproces voor beide probevarianten gepresenteerd, gevolgd door ontwerp- en layout afwegingen in de probe om compatibel te zijn met beide transducertechnologieën. Vervolgens wordt de verpakking van beide probevarianten in detail besproken. Daarna worden de meetopstellingen voor het karakteriseren van beide transducermatrices in RX en TX behandeld. De CMUT-matrix heeft een gemiddelde TX-efficiëntie van 12,2 kPa/V met een standaardafwijking van 1,9 dB en een gemiddelde RX-efficiëntie van 0,93 nA/Pa met een standaardafwijking van 2,0 dB. Vanwege fabricageproblemen kon de piëzo-elektrische transducerarray alleen

in RX worden geëvalueerd en heeft een gemiddelde efficiëntie van 2,5 nA/Pa. De richtingsgevoeligheid van beide apparaten is smaller dan simulaties voorspellen, waarschijnlijk omdat overspraak niet nauwkeurig wordt gemodeleerd. Ondanks fabricageproblemen toont het hoofdstuk aan dat het ontwikkelde systeem kan dienen als een nuttig meetplatform voor systematische evaluatie van verschillende transducermatrices.

Hoofdstuk 4

Dit hoofdstuk behandelt de evaluatie van de beeldvormingsprestaties van één ASIC-tegel met een 32×64-element CMUT matrix in de probe, die in voorafgaande hoofstukken behandeld is. Meerdere beeldvormingsschema's die zijn vergeleken gebruiken een (sub)set van 9 divergerende TX-bundels om een 60°×60°×10 cm volume in beeld te brengen. Om de schema's te evalueren, is een speciaal 3D-draadfantoom gemaakt om de puntspreidingsfunctie (PSF) over het volledige volume te schatten. Daarnaast is het contrast gemeten met een CIRS 040GSE fantoom en zijn de 3D Dopplerprestaties geëvalueerd door beeldvorming van bloedimiterende vloeistof die door een 4 mm buis in een CIRS ATS524 flow fantoom is gepompt. Er werd vastgesteld dat TDM-geïnduceerde overspraak geen significante invloed heeft op de beeldkwaliteit. Bovendien kan een beeldvormingsschema dat 4 puls-echo opnames per volume vereist de stroomsnelheden volgen die in AAA's (0,4 m/s) te verwachten zijn, met behoud van voldoende resolutie. Het beeldcontrast in echovrije gebieden met dit schema is echter lager dan verwacht. Hoewel dit contrast verbetert bij gebruik van een beeldvormingsschema dat volumes reconstrueert met 9 puls-echo opnames, gaat dit ten koste van de mogelijkheid om de gewenste stroomsnelheden te volgen.

Hoofdstuk 5

Dit hoofdstuk sluit het proefschrift af en biedt een overzicht van de resultaten. Er zijn meerdere originele bijdragen geleverd. Een van de belangrijkste is dat de gepresenteerde probe een effectieve strategie voor kanaalreductie, bestaande uit micro-beamforming en TDM, schaalt naar een matrix van duizenden elementen. Een andere belangrijke bijdrage is de TX-beamformer in de probe, die een hoge flexibiliteit in de definitie van TX-golfvormen bereikt en tegelijkertijd relatief eenvoudig te implementeren is. Bovendien is de probe een van de eerste die een CMUT-matrix met duizenden elementen monolithisch integreert op ASIC's. Het hoofdstuk biedt ook een vooruitzicht op toekomstige verbeteringen aan het ontwikkelde systeem, zowel op de korte als de lange termijn. De belangrijkste hiervan

zijn manieren om het aantal kanalen verder te reduceren.

List of abbreviations

1D	1-Dimensional
2D	2-Dimensional
3D	3-Dimensional
AA	Abdominal Aorta
AAA	Abdominal Aortic Aneurysm
AC	Alternating Current
ADC	Analog-to-Digital Converter
ALE	Adaptive Linear Equalizer
ASIC	Application-Specific Integrated Circuit
AWG	Arbitrary Waveform Generator
BCD	Bipolar-CMOS-DMOS
BF	Beamformer
BVD	Butterworth-Van Dyke
BW	Bandwidth
CA	Current Amplifier
CAD	Computer-Aided Design
CMOS	Complementary Metal-Oxide Semiconductor
CMUT	Capacitive Micromachined Ultrasound Transducer
CNR	Contrast-to-Noise Ratio
CR	Contrast Ratio
CT	Computed Tomography
CVD	Cardiovascular Diseases
CW	Continuous Wave
DC	Direct Current
DFF	D-Flip-Flop
DMOS	Double-diffused Metal-Oxide Semiconductor
DR	Dynamic Range
D-TDM	Digital Time-Division Multiplexing
EQ	Equalizer

EVAR	Endovascular Aortic Aneurysm Repair
FDM	Frequency-Division Multiplexing
FFT	Fast Fourier Transform
FIR	Finite Impulse Responsee
FoV	Field-of-View
FPGA	Field-Programmable Gate Array
FWHM	Full-Width Half Maximum
HS LS	High-Side Level-Shifter
HV	High Voltage
HVR	High Volume-Rate
LDO	Linear Drop-Out Regulator
LS LS	Low-Side Level-Shifter
LV	Low Voltage
MRI	Magnetic Resonance Imaging
MUX	Multiplexing
OR	Open Aneurysm Repair
OTA	Operational Transimpedance Amplifier
PCB	Printed Circuit Board
PDM	Pulse-Density Modulated
PMUT	Piezo-electric Micromachined Ultrasound Transducer
PRBS	Pseudo-Random Bit Sequence
PRF	Pulse-Repetition Frequency
PSD	Power Spectral Density
PSF	Point-Spread-Function
PW	Pulsed-Wave
PZT	Lead Zirconate Titanate
R&D	Research & Development
RT-MRI	Real-Time Magnetic Resonance Imaging
RX	Receive
RX BF	Receive Beamformer
SAP	Sub-Aperture
SNDR	Signal-to-Noise+Distortion Ratio
SNR	Signal-to-Noise Ratio
SOI	Silicon-on-Insulator
SR	Shift Register
T/R	Transmit/Receive

TDM	(Analog) Time-Division Multiplexing
TGC	Time-Gain Compensation
TIA	Trans-Impedance Amplifier
TPX	Polymethylpentene
TX	Transmit
TX BF	Transmit Beamformer
VC	Control Voltage
VGA	Variable-Gain Amplifier
VSX	Verasonics Vantage-256
WHO	World Health Organization
µBF	Micro-Beamformer

List of publications

Related to the Contents of this Dissertation

N.N.M. Rozsa, D. Simoes Dos Santos, P. Timmermans, E. Noothout, Z. -Y. Chang, V.A. Henneken, R. van Schaijk, J. Voorneveld, N. de Jong, H.J. Vos, J.G. Bosch, M.D. Verweij, M.A.P. Pertijs, "Characterization of a CMUT and PZT Array Integrated on a Common ASIC Design," *2025 IEEE International Ultrasonics Symposium (IUS)*, September 2025, (presentation).

N.N.M. Rozsa, Z. Chen, T. Kim, P. Guo, Y. Hopf, J. Voorneveld, D. Simoes Dos Santos, E. Noothout, Z. -Y. Chang, C. Chen, V.A. Henneken, N. de Jong, H.J. Vos, J.G. Bosch, M.D. Verweij, M.A.P. Pertijs, "A 2000-volumes/s 3-D Ultrasound Probe With Monolithically-Integrated 23 × 23-mm^2 4096 -Element CMUT Array," in *IEEE Journal of Solid-State Circuits*, vol. 60, no. 4, pp. 1397-1410, April 2025, doi: 10.1109/JSSC.2025.3534087, (invited).

N.N.M. Rozsa, Z. Chen, T. Kim, P. Guo, Y. Hopf, J. Voorneveld, D. Simoes Dos Santos, E. Noothout, Z. -Y. Chang, C. Chen, V.A. Henneken, N. de Jong, H.J. Vos, J.G. Bosch, M.D. Verweij, M.A.P. Pertijs, "A 3D Ultrasound Probe with Monolithically-Integrated 4096-Element CMUT Array Imaging 60°×60°×10 cm at 2000 Volumes/s," *2024 IEEE International Ultrasonics Symposium (IUS)*, September 2024, (presentation & student paper competition winner).

N.N.M. Rozsa, Z. Chen, T. Kim, P. Guo, Y. Hopf, J. Voorneveld, D. Simoes Dos Santos, E. Noothout, Z. -Y. Chang, C. Chen, V.A. Henneken, N. de Jong, H.J. Vos, J.G. Bosch, M.D. Verweij, M.A.P. Pertijs, "A 2000-Volumes/s 3D Ultrasound Imaging Chip with Monolithically-Integrated 11.7×23.4mm^2 2048-Element CMUT Array and Arbitrary-Wave TX Beamformer," *2024 IEEE Symposium on VLSI Technology and Circuits (VLSI Technology and Circuits)*, Honolulu, HI, USA, 2024, pp. 1-2, doi: 10.1109/VLSITechnologyandCir46783.2024.10631363.

Unrelated to the Contents of this Dissertation

N. Radeljic-Jakic, A.J. Flikweert, **N.N.M. Rozsa**, H.J. Vos and M.A.P. Pertijs, "Using Image Quality Metrics to Optimize the Design of Integrated Medical Ultrasound ADCs," *IEEE Transactions on Ultrasonics, Ferroelectrics, and Frequency Control*, doi: 10.1109/TUFFC.2025.3577258.

I. Bellouki, **N.N.M. Rozsa**, Z.-Y. Chang, Z. Chen, M. Tan and M.A.P. Pertijs, "An Amplitude-Programmable Energy-Recycling High-Voltage Resonant Pulser for Battery-Powered Ultrasound Devices," in *IEEE Journal of Solid-State Circuits*, doi: 10.1109/JSSC.2024.3494536.

I. Bellouki, **N.N.M. Rozsa**, Z.-Y. Chang, Z. Chen, M. Tan and M. Pertijs, "6.4 A Resonant High-Voltage Pulser for Battery-Powered Ultrasound Devices," *2024 IEEE International Solid-State Circuits Conference (ISSCC)*, San Francisco, CA, USA, 2024, pp. 106-108, doi: 10.1109/ISSCC49657.2024.10454286.

D. Simoes Dos Santos, F. Fool, T. Kim, E. Noothout, **N.N.M. Rozsa**, H.J. Vos, J.G. Bosch, M.A.P. Pertijs, M.D. Verweij, N. de Jong, "Automated Characterization of Matrix Transducer Arrays using the Verasonics Imaging System," *2022 IEEE International Ultrasonics Symposium (IUS)*, Venice, Italy, 2022, pp. 1-4, doi: 10.1109/IUS54386.2022.9957544.

H. Zhang, **N.N.M. Rozsa**, M. Berkhout and Q. Fan, "A Chopper Class-D Amplifier for PSRR Improvement Over the Entire Audio Band," in *IEEE Journal of Solid-State Circuits*, vol. 57, no. 7, pp. 2035-2044, July 2022,
doi: 10.1109/JSSC.2022.3161136.

H. Zhang, **N.N.M. Rozsa**, M. Berkhout and Q. Fan, "A -109.1 dB/-98 dB THD/THD+N Chopper Class-D Amplifier with >83.7 dB PSRR Over the Entire Audio Band," *ESSCIRC 2021 - IEEE 47th European Solid State Circuits Conference (ESSCIRC)*, Grenoble, France, 2021, pp. 395-398,
doi: 10.1109/ESSCIRC53450.2021.9567786.

Acknowledgements

I don't often take the time to reflect on the successes of the past, but one of the biggest is the vast amount of friends and colleagues I've had the privilege to work with, and those who've supported me along the way. While I've enjoyed the journey of the past 4 years, it is certainly not one I've walked alone and in this section, I'd like to express my gratitude.

First and foremost, I would like to express my deep gratitude to my promotor, Michiel Pertijs, for his guidance the last 4 years, and hopefully more years to come. Throughout my PhD, he gave a lot of creative freedom to operate, while still consistently and frequently being available for discussions and feedback, where he had a lot of valuable insights to give. Not only was he almost always available to give his insights, I've also enjoyed the many discussions we've had in general. This varied from envisioning how the field of ultrasound is and should be moving, and discussing cool potential circuit and system ideas, to political and other topics. Overall, I've thoroughly enjoyed our collaboration so far and am looking forward to continuing it in the future.

I would also like to thank my co-promotor, Martin Verweij, for all his guidance. Especially his input for the acoustic design, fabrication and evaluation of the probe were invaluable. Moreover, his input in both the Ultra-X-Treme and my PhD project planning, his openness to looking for solutions when things were not going as planned, and his feedback on papers are greatly appreciated.

On a similar note, I would like to thank all the other PIs who were directly involved with my research - Jason Voorneveld, Hans Bosch, Nico de Jong, and Rik Vos - for their valuable input. I appreciate all the feedback they've given on papers and their frequent willingness to discuss the acoustical design and evaluation of the probe in depth. I also appreciate all the help Jason has given to make the imaging of the probe possible, from designing and providing most of the beamforming scripts, to simulating its imaging performance, and more. While not directly involved, I also want to thank Tiago Costa and Pieter Kruizinga for allowing me to borrow (a lot of) equipment from their groups/sections, and Kofi Makinwa for the feedback he has given on multiple occasions.

Multiple PhD students and postdocs also directly contributed towards the success of the probe covered in this dissertation, whom I would like to express a deep gratitude towards. First and foremost, these are Zhao Chen, Taehoon Kim and Djalma Simoes dos Santos. Zhao and Taehoon laid a significant amount of the ground work on the in-probe ASIC's architecture, did some of the block-level designs, and greatly helped during the layout phase of the ASIC. Djalma worked on the probe's acoustic design and helped with its acoustical validation. I've enjoyed our cooperation, the valuable insights and feedback they've given me, and the many great discussions we've had.

Furthermore, I'd like to thank Chao Chen, Peng Guo, and Yannick Hopf. Their help during the layout phase of the ASIC has been invaluable, not to mention the circuit designs that Peng and Yannick did during their PhD having directly benefited this ASIC design as well. Even though the tape-out of the ASIC was one of the most stressful times in my PhD, I see the great cooperation with everyone as one of the greatest highlights.

Within the Ultra-X-Treme consortium, I had the privilege of working with many academic and industrial institutions, of which I've already named a lot of people from TU Delft and Erasmus MC, but I also want to highlight the great collaboration I've had with Bas Jacobs, Davie Mtsuko, Eugene Timmering, Hans Huiberts, Johan Klootwijk, Juan Chacon, Peter Timmermans, Rob van Schaijk, Vincent Henneken, Zhao Chen, and more from Philips, and later (for most) Xiver, which made the monolithic integration of CMUTs on the ASICs in the probe, the probe's packaging and CMUT evaluation possible. While I don't have a lot of reference points, I can hardly imagine a better industry-academia partnership and I look forward to continuing it in the future.

Furthermore, I would like to express my sincere gratitude to everyone who contributed to the excellent support infrastructure at both the Department of Microelectronics and the Acoustical Wavefield Imaging Laboratory, starting with Emile Noothout, Henry den Bok, Jeroen Bastemeijer, Lukasz Pakula, Ron van Puffelen and Zu-Yao Chang. While always being available to discuss and assist with solving challenges in fabrication of the probe and its many measurement setups, they were also great brainstorming and conversation partners. In addition, I'd like to highlight the massive amount of fabrication work done by Emile and Zu-Yao to build the probes covered in this dissertation and their input for the ASIC's pad-ring design. I also want to highlight the considerable work done by Henry to build one

of the motherboards in the system and the contributions of Tim Hosman for the design of the first version of the PCB on which the ASICs are mounted. Furthermore, I want to thank Antoon Frehe for his efforts in keeping the Cadence servers running 24/7, which was essential for designing the probe. Last but not least, I want to thank all the management assistants of both departments, especially my main contacts Elisabeth van Eysinga, Joyce Siemers and Kellen Erb for all the organization work they do to keep things running smoothly.

I also want to thank everyone I've met in the Smart Ultrasound Group at TU Delft. Throughout the years I've greatly benefited from the knowledge and insights of its members Chao Chen, Douwe van Willigen, Eunchul Kang, Imad Bellouki, Mingliang Tan, Nikola Radeljic-Jakic, Peng Guo, Taehoon Kim, Tim Hosman, and Zhao Chen, either through architecture and design reviews, the many brainstorming sessions we've had, or debugging issues together. Moreover, as aforementioned, the many circuit blocks developed within the group have been essential building blocks in the presented probe. I think we created a great environment of cooperation, which I'm truly grateful to be a part of. Moreover, I look back very fondly on all the discussions we've had and activities we've done throughout the years. This thank you also extends to my many other colleagues and friends within the Microelectronics department. The general willingness for cooperation and to discuss each others technical and personal issues has been invaluable. Both inside and outside the office, I've enjoyed the time we spent together.

Finally, I want to thank all my friends and family who have supported me up to this point. I've had the extraordinary privilege of having very close friends from every major step in life so far, from my time in elementary school to academia. Their continued companionship has been a major pillar of support, one which I am truly grateful to have. Moreover, I want to highlight the massive and unconditional support that my mother, father and sister have given me, which has been essential to the successes that I have achieved so far.

Nuriel Rozsa
Delft, June 2025

About the author

Nuriel Nathan Machiel Rozsa was born in Seattle, United States in April 1997 and moved to The Netherlands in 2000.

He received the B.Sc. degree (cum laude) in electrical engineering and the B.Sc. honours program certificate from Delft University of Technology, Delft, The Netherlands in 2018. He received the M.Sc. degree in microelectronics from Delft University of Technology, Delft, The Netherlands in 2021.

He pursued a Ph.D. degree at the Electronic Instrumentation Laboratory from 2021 to 2025, working within the Ultra-X-Treme research program on high frame-rate 3D ultrasound probes for imaging the Abdominal Aorta. His current research interests include analog and mixed-signal electronics and system design for ultrasound imaging applications.

In his spare time, he enjoys socializing, video- and boardgames, miniature wargames, working on electronics and modeling hobby projects, and following cultural and political events.

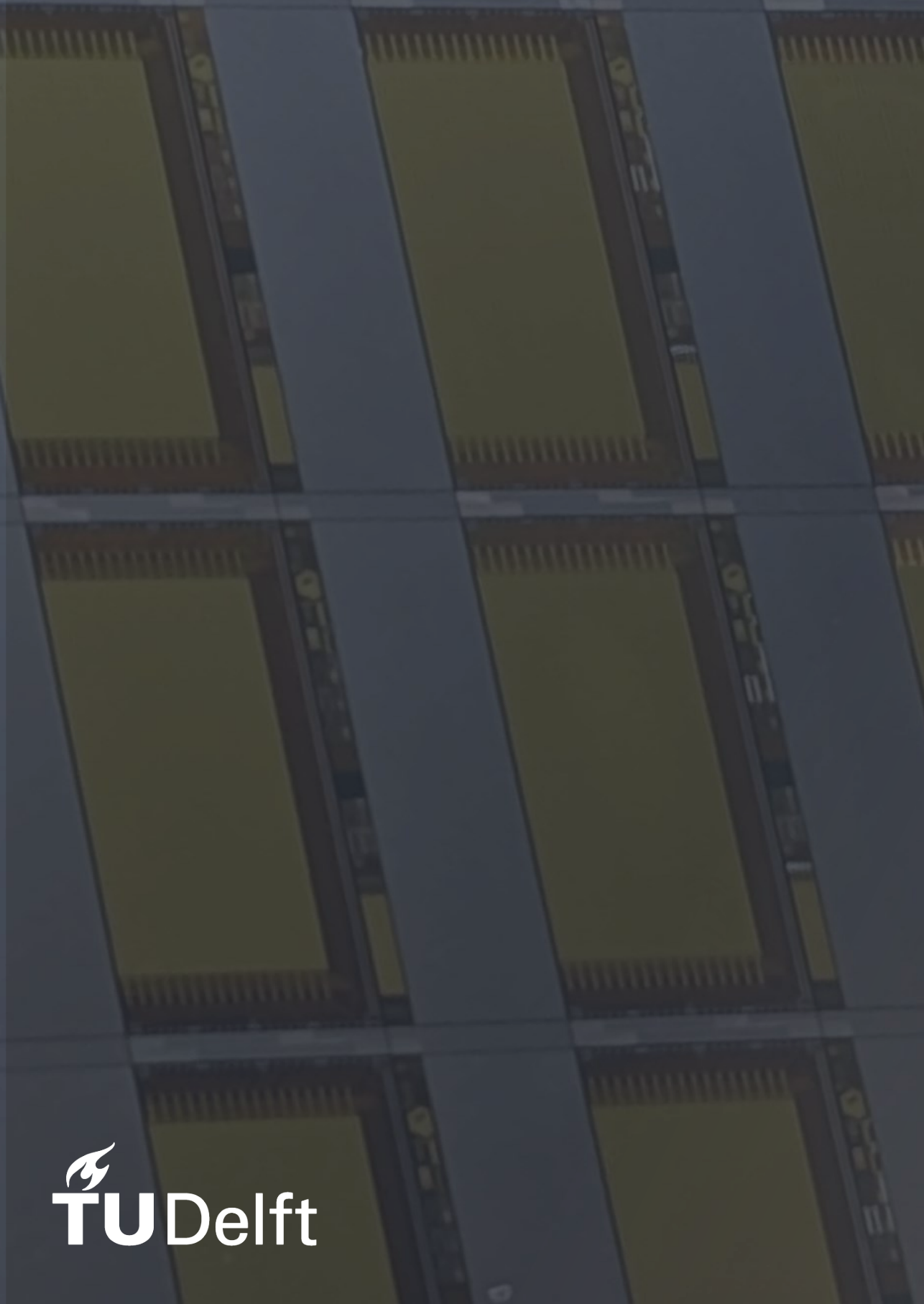
TUDelft